

Gran Sasso Science Institute
XXXII cycle



GRAN SASSO SCIENCE INSTITUTE

Multiple detector analysis
in the CRESST Dark Matter experiment

PhD candidate:
Stefano DI LORENZO

Advisors:
Paolo GORLA (LNGS-INFN)
Carlo BUCCI (LNGS-INFN)

Abstract

During the past century, from the first observation of the velocity anomalies in the Coma Cluster made by Zwicky, several observational evidences were collected at both galactic and cosmological scale that there is a large amount of matter in our universe is dark. The most recent results of the Planck mission measured the ratio between ordinary matter and dark matter to be around 5. Still the nature of dark matter, despite the significant effort of the scientific community, remains unknown.

The CRESST (Cryogenic Rare Event Search with Superconducting Thermometers) experiment based at the underground facility of the Laboratori Nazionali del Gran Sasso (LNGS) is one of the most sensitive experiments aiming at the direct detection of dark matter particles via elastic scattering off nuclei in CaWO_4 scintillating crystals. The CRESST crystals are operated as cryogenic calorimeters, each equipped with a cryogenic light detector for the detection of the scintillation light coming from the crystals.

When a particle interacts inside the detector produces a phonon and a light signal; the latter is used to discriminate nuclear recoils, possibly induced by dark matter scattering, from electron recoils induced by the dominant electron/gamma background. Defining the Light Yield as the ratio between the energy measured in the light channel and the one measured in phonon channel, it is possible to establish regions (bands) where the different interactions are expected.

The results of CRESST Run 32 showed an excess of events in the acceptance region that could not be explained in terms of known backgrounds. Interpreting these events as a dark matter signal, under the most standard assumptions for the galactic dark matter halo, identifies regions in the cross-section vs mass parameters space compatible with the observation. In the following CRESST physics run, thanks to a substantial global background reduction, it was possible to partially exclude the dark matter interpretation of the excess of events.

This work aims to test with a high statistic the CRESST run 32 excess, to prove (and possibly exclude) the dark matter interpretation. The analysis is performed on the full dataset collected during Run 33 using a Likelihood approach to combine the data from multiple detectors.

For this purpose data collected during CRESST Run 33 were used. These data, acquired between July 2013 and August 2015, provide a very large exposure, of the order of $\gtrsim 130$ kg·day for each detector, allowing to achieve an improvement of the the CRESST exclusion limit for dark matter masses above $1 \text{ GeV}/c^2$.

The description of the CRESST experimental framework in which the ana-

lysis has been portrayed, together with all the steps of the analysis workflow needed to go from the collected raw data to the fit of the bands in the Light Yield - Energy plane are described. The steps needed for extending the range of the detector, the operations necessary for the energy calibration, alongside the different cuts to remove pile-up and spurious events for the different detectors are thoroughly discussed. The relevant parameters for the electron/gamma and nuclear recoil bands that are used to produce the exclusion limit are computed for each individual detector.

The exclusion limit is computed in this work with an Extended Maximum Likelihood approach, which allows to combine the data of multiple detectors and benefit of the cumulative exposure.

The final part of the thesis focuses on comparisons with previous results and possible future improvements. The exclusion of the dark matter interpretation of the excess observed in Run 32 is discussed.

*A Zio Freddy
e Nonna Venusta*

Ringraziamenti

Una tesi, specialmente una tesi di dottorato, non è mai il lavoro di una sola persona, e questa tesi non è di certo un'eccezione. Per questo voglio ringraziare diverse persone per l'aiuto che mi hanno dato durante questi quantomai travagliati mesi di scrittura.

I primi ringraziamenti vanno ai miei relatori, Carlo e Paolo. Il loro aiuto e sostegno è stato fondamentale durante la stesura di questa tesi.

Un grazie particolare a Paolo per le intere giornate che mi hai dedicato.

Un grazie speciale va Francesco, che ha avuto fiducia in me. Sarò sempre felice di partecipare a qualsiasi iniziativa mi proporrai.

Un grazie di ad Irene, Giovanni, Daniele, Ambra, Guido, Laura, Giovanni, Valetina e tutte le persone LNGS.

Un enorme ringraziamento va a Nello, penso che non avrei potuto chiedere un compagno di ufficio migliore di te. Grazie per la tua compagnia, il tuo supporto e tutte le citazioni di Boris.

Un grazie speciale a tutti i miei compagni del corso di dottorato AP XXXII per reso questi anni speciali.

Un pensiero speciale va a Vanessa, Enrico e Zhao per essermi stati vicini durante la scrittura ed il lockdown.

Un ringraziamento sentito va a i miei ormai ex compagni di Pisa: Fabio, Francesco, Niccolò, Claudia, Marta, Matteo, Roberto, Francesca, Alberto, Alessandro, Lucia, Maro, Simone, Leonardo. Siete degli ottimi amici ed ogni volta che ci riusciamo a vedere di persona il cuore mi si riempie di gioia.

Grazie a Lorenzo e Paolo per le nostre chiacchierate di questi ultimi due anni.

Un grazie di cuore ai miei amici di sempre Alessio, Simone, Peppe, Alessandro, Pietro e Matteo. Nonostante non ci vediamo più tutti i giorno come ai tempi della scuola, ogni volta che vi incontro mi sembra sempre che non ci sia giorno che non ci siamo visti.

Un grazie a tutti i miei zii e cugini, per i momenti in allegria durante i miei fugaci passaggi a casa.

Grazie a Nonno Rocco, che mi riesce sempre a strappare un sorriso.

Miriam, le parole non potranno mai esprimere quanto ti sia grato per l'aiuto ed il supporto che mi hai dato durante tutto questo percorso.

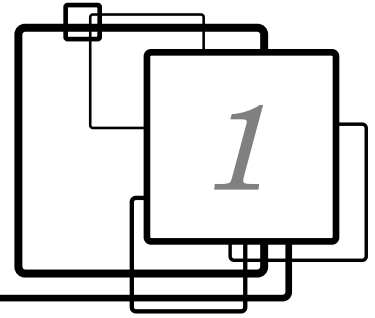
Infine grazie, grazie, grazie, un milione di volte grazie alla mia Famiglia. Anche nei momenti in cui ero scontroso ed arrabbiato, voi ci siete sempre stati. Grazie per quello che mi avete sempre dato e mi darete e per tutti i *Tu sai...* Vi voglio bene.

Contents

Abstract	3
Ringraziamenti	7
1 A Dark Universe	13
1.1 Evidence for Dark Matter in our universe	13
1.1.1 The velocity dispersion of galaxy clusters	13
1.1.2 Galaxies rotation curve	14
1.1.3 Galaxy Clusters Collisions	15
1.1.4 Cosmic Microwave Background	16
1.1.5 Structures formation	17
1.1.6 Stellar Streams	17
1.2 Dark Matter Candidates	17
1.2.1 Neutrinos	19
1.2.2 WIMPs	19
1.2.3 Asymmetric Dark Matter	20
1.2.4 Axions	21
2 The hunt for Dark Matter	23
2.1 Dark Matter search approaches	23
2.1.1 Collider search	23
2.1.2 Indirect search	24
2.1.3 Direct search	25
2.2 Dark Matter Interaction Rate	25
2.2.1 Velocity distribution	26
2.2.2 Cross section	27
2.3 Experimental approaches for direct search	29
2.3.1 Cryogenic Detectors	29
2.3.2 Liquid Noble Gas TPCs	29
2.3.3 NaI experiments	30
2.3.4 Directional experiments	32
3 The CRESST experiment	35
3.1 Background and shielding	36
3.1.1 Muon background	36
3.1.2 Neutron background	38

3.1.3	Natural radioactivity chains background	38
3.1.4	Particle Identification	39
3.2	CRESST working principle	40
3.2.1	Cryogenic calorimeters	40
3.2.2	Signal readout	42
3.2.3	Detector operating point and response	44
3.3	CRESST most recent results	46
4	CRESST data analysis	51
4.1	Data acquisition	51
4.1.1	CRESST datasets	52
4.2	Pulse Fit and Energy calibration	53
4.2.1	TES range extension	53
4.2.2	Linearization and Energy Calibration	56
4.3	Stability, coincidence, and data quality cuts	58
4.3.1	Blind analysis	59
4.3.2	Stability Cuts	59
4.3.3	Coincidence Cuts	60
4.3.4	Data Quality Cuts	61
4.3.5	RMS Cut	62
4.3.6	Carrier Cut	63
4.4	Data Simulation and Cut Efficiency	67
4.4.1	Event Simulation	67
4.4.2	Cut Efficiency	67
4.4.3	Resolution and Threshold	68
4.5	Light Yield and Energy spectrum	69
4.5.1	CPE optimization	69
4.5.2	Gamma line tilt correction	70
5	Detector Analysis	75
5.1	Detector population	76
5.1.1	TUM40 detector	76
5.1.2	Frederika detector	81
5.1.3	Anja detector	87
5.1.4	Lise detector	91
5.1.5	Verena detector	95
5.2	Detector Response	101
5.2.1	Electron/Gamma light mean	101
5.2.2	Electron/gamma energy spectrum	103
5.2.3	Nuclear recoil light mean	103
5.2.4	Nuclear recoil energy spectrum	104
5.2.5	Band Width	104
5.2.6	Excess Light	105
5.3	Energy Spectrum and Light Yield	106
5.3.1	TUM40	107

5.3.2	Frederika	109
5.3.3	Anja	111
5.3.4	Verena	112
5.3.5	Lise	112
6	Maximum Likelihood	115
6.1	Maximum Likelihood	115
6.1.1	Extended Maximum Likelihood	116
6.1.2	Exclusion Limit with Profiled Likelihood Ratio	116
6.2	Density functions	117
6.2.1	CRESST Likelihood description	118
7	Dark Matter results	119
7.1	TUM40	119
7.2	Frederika	120
7.3	Anja	121
7.4	Verena	121
7.5	Lise	122
7.6	Combined limit	123
7.7	Conclusions and outlook	126
7.7.1	Study of Systematics	126
	Bibliography	129



A Dark Universe

Lord Kelvin in 1904 was one of the first to propose a dynamical estimation of the Milky Way mass based on the gas theory, to determine the number of dark bodies inside the galaxy. A relation between the galaxy size and its velocity dispersion can be established, describing the stars as particle gas interacting gravitationally [1]. Fascinated by the idea of Kelvin, in 1906 Poincaré [2] argued that since the velocity dispersion predicted in Kelvin's estimate is of the same order of magnitude as that observed, the amount of *matière obscure* was likely to be less than or similar to that of visible matter [3].

Nevertheless it was only in 1933 that Fritz Zwicky, while studying the redshift of different galaxy clusters in *Die Rotverschiebung von extragalaktischen Nebeln* (The Redshift of extragalactic nebulae) [4, 5], noticed the high-velocity dispersion of galaxies in the Coma cluster. Applying the virial theorem to the cluster, Zwicky inferred a total mass ~ 400 times larger than the one expected from the luminous mass. The presence of this unseen mass was a difficult result to be explained, and Zwicky decided to call this extra amount of mass *dunkle Materie*, Dark Matter.

The Dark Matter existence became widely accepted in the 1970s thanks to the studies of Vera Rubin. Using the advanced spectrometer developed by Kent Ford, Vera Rubin provided the first firm evidence of Dark Matter as a result of the rotation curves of Andromeda Nebula [6] and several spiral galaxies [7, 8].

Nowadays, there are several experimental evidences at galactic and cosmological scales, pointing out that most of the matter in our Universe is dark. Despite the scientific community effort during the past century, the nature of Dark Matter remains still unknown.

1.1 Evidence for Dark Matter in our universe

1.1.1 The velocity dispersion of galaxy clusters

Traditionally Dark Matter's first evidence came from the study of velocity dispersion in galaxy clusters. In a study done by Zwicky on a variety of different Galaxy Clusters [4, 5], a large velocity dispersion was noticed in the Coma cluster.

Supposing that the Coma cluster reached the mechanical equilibrium, it is possible to apply the virial theorem. From the velocity measurements obtained, the mass of the cluster is inferred. The cluster mass computation with the virial theorem is 400 larger than the one inferred by the luminous matter.

Even if the stationarity hypothesis fell, the problem persists. If the cluster is not at equilibrium and the virial theorem could be not applied, the difference in the computed mass is of a factor one half: a large amount of mass compared to the visible one is still needed to explain why the cluster is gravitationally bounded.

If the cluster mass is only the one due to the luminous mass, the velocity dispersion will rip it apart in the future. In this case, many isolated galaxies with large proper velocity are expected in the Universe, but such a conclusion does not match the observations.

In 1927 Zwicky confirmed this result [9], proposing a new method based on the Gravitational Weak Lensing discussed by Einstein[10] and Zwicky himself [11, 12]. The cluster mass is deduced using such effect looking at the distortion induced on light coming from the behind galaxies.

Other discrepancies analogues to the Coma cluster one were also observed in the Virgo cluster in 1936 [13].

1.1.2 Galaxies rotation curve

Dark Matter presence at the galaxy scale was confirmed in the 1970s with the measurement of stars orbital velocity in spiral galaxies made by Vera Rubin with the powerful spectrometer realized by Kent Ford [7, 6, 8]. A star moving in a circular orbit of radius r so that the gravitational force balances the centrifugal force

$$\frac{mv(r)^2}{r} = G \frac{mM(r)}{r^2}; \quad (1.1)$$

where $v(r)$ is the velocity at a distance r from the galactic center and $M(r)$ is the galaxy mass contained within this radius r . The larger fraction of the luminous matter in a spiral galaxy is clustered in the center. Denoting the average mass density with ρ , $M(r)$ is defined by :

$$M(r) = \frac{4}{3}\pi r^3 \rho. \quad (1.2)$$

If the galaxy mass is only due to the luminous core, its velocity is expected to grow like $v(r) \sim r$ in the central region and decrease like $\sim 1/\sqrt{r}$ outside the galaxy core.

This behaviour is not in agreement with observation in several rotation curve measurements done on spiral galaxies [14]. The data suggest the presence of a giant Dark Matter halo around the galaxy. As an example, Figure 1.1 shows the measured rotation curve of galaxy M33 with the fitted model accounting for the different velocity contribution [15].

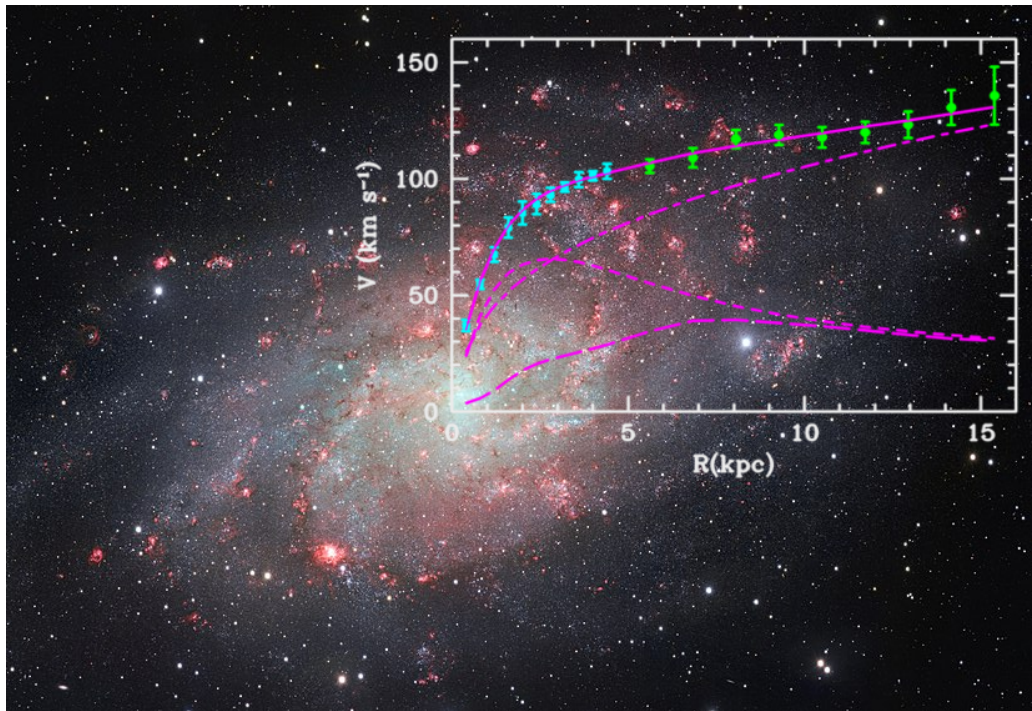


Figure 1.1: The figure shows the measured velocity obtained with optical (cyan) and radio (green) measurements, together with the a model fit for velocity (solid line) and the different contributions: the halo (dash dotted), the luminous mass (short dashed) and the gas (long dashed).

1.1.3 Galaxy Clusters Collisions

Another important indication for Dark Matter existence comes from galaxy clusters collisions. The first evidence came from the study of 1E 0657-558 cluster [16], often referred to as the Bullet Cluster. The term Bullet Cluster is due to the sub-cluster shape, which passes through the main cluster. In a cluster, stars and galaxies form $1\div 2\%$ of the mass [17] while plasma accounts for $5\div 15\%$ [18] and dark matter for the rest. Usually, all of these three species follow a spherical symmetry due to the gravitational potential. During a collision, stars and galaxies behave like collisionless gas. While the baryonic-plasma counterpart of the two clusters suffers a slow down due to the electromagnetic interaction.

Figure 1.2 shows this effect. The X-ray distribution due to baryonic matter is shown in pink, while the mass distribution inferred using the gravitational lensing is depicted in blue. From the pink distribution in the smaller cluster, it is possible to appreciate the typical shock wave shape due to the collision.

Looking instead at the blue distribution, it is clear that the two population undergo through different interactions which cause their separation.

In 2008 the merging galaxy cluster MACSJ0025.4-1222 was identified [19], showing that the Bullet Cluster is not an isolated case.

The Bullet Cluster is one the Dark Matter best evidence: the different plasma and gravitational mass behaviour during the collision attest the Dark Matter collisionless nature [20, 21]. It is required to mention that many attempts have

been pursued to explain this effect, and many other unexplained gravitational effects a cosmological distance, with Modified Gravity Models [22]. So far, these models have not been able to account for all anomalies.

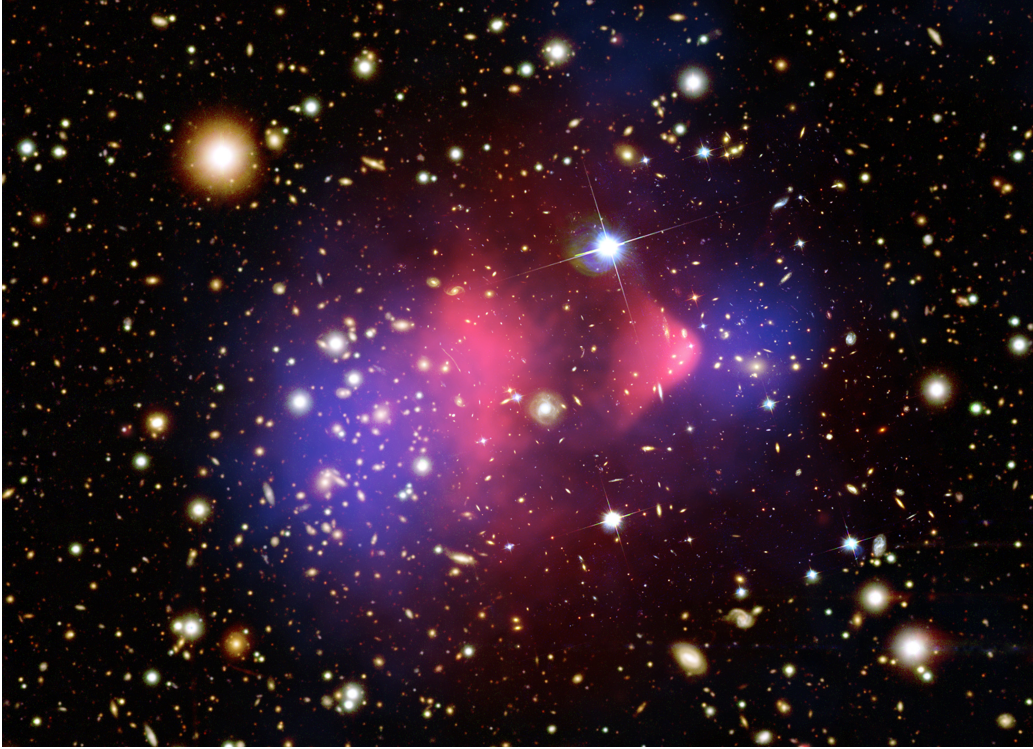


Figure 1.2: The image shows in pink the X-ray distribution due to the plasma, and in blue the distribution of matter computed using the gravitational lensing.

1.1.4 Cosmic Microwave Background

The Cosmic Microwave Background was firstly predicted in 1948 by Peebles [23] and then discovered in 1964 by Penzias and Wilson [24]. The CMB is electromagnetic background radiation isotropically permeating the whole Universe.

After its discovery, this radiation was soon interpreted as the Big Bang remnant [25].

Due to the expansion of the Universe, 380'000 years after the Big Bang, the mean photon energy became lower than the binding energy of the Hydrogen atom corresponding to 13.6 eV. From that moment on, photons were free to travel across the Universe since they could not separate Hydrogen atoms in electrons and protons. For this reason, the CMB is also referred to as the last surface scattering. As a consequence of the Universe expansion, this remnant radiation has been redshifted from the UV region (13.6 eV) to the microwave region. The thermal spectrum of the actual CMB radiation corresponds to a black body spectrum characterized by a temperature of 2.72548 ± 0.00057 K [26]

Studying the angular distribution of the temperature fluctuations, which are of the order $\Delta T/T \sim 10^{-5}$, the main parameters of the Standard Cosmological

Model can be obtained as predicted in [27]. From the 1990s to our days, three satellite missions measured the spatial distribution of the CMB spectrum with an increasing precision: COBE [28], WMAP [29], and Planck [30].

In the most recent results of Planck [31], the fit of the multipole power spectrum of the CMB anisotropies (Fig.1.3) shows that our Universe is made of dark energy 69.94%, dark matter for 26.06%, and baryonic matter 4.90%. The model validity is in agreement with the baryonic density coming from the Big Bang Nucleosynthesis theory [32].

1.1.5 Structures formation

Another evidence of the Dark Matter existence is the presence of the structures present today in the Universe. Structure formation started when matter density overtook radiation density as the primary contributor to the energy content of the Universe. At this point, regions with a slightly higher density acted as gravitational attractors, becoming the seeds for structures formation.

Only non-relativistic moving matter can be trapped in the small gravitational bound system, which is why Dark Matter is considered to be *cold*. As matter starts to collapse, the structure formation process is regulated by the gravitational force that pulls the mass in, and radiation pressure pushes it out. When the system reaches a critical mass, called Jeans mass [33], at which gravity overwhelm pressure, the system collapses. The presence of a weakly interacting Dark Matter not driven apart from radiation pressure facilitates the creation of gravitational wells where baryonic matter can fall and start to form structures.

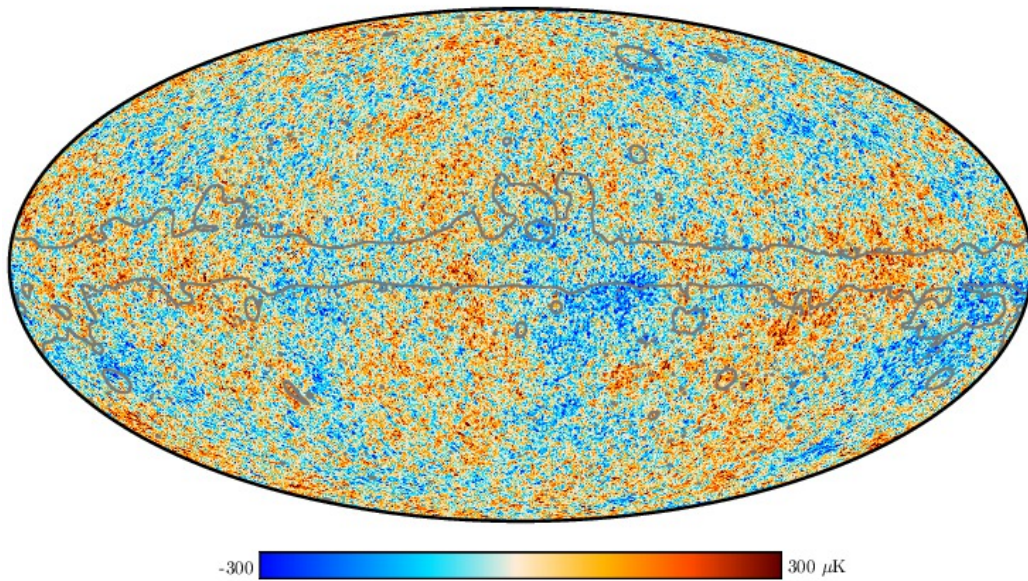
Many body simulations [34, 35] can reproduce structures comparable with the ones observed in today's Universe only when accounting for the presence of cold Dark Matter; otherwise, a longer time for structure formation is necessary.

1.1.6 Stellar Streams

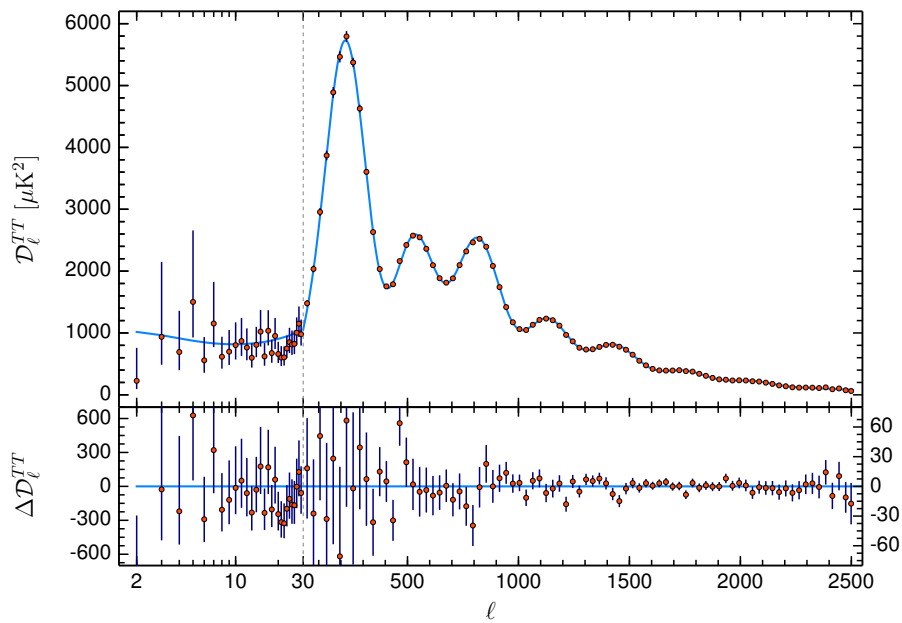
Another evidence for the existence of Dark Matter in the galaxy structures comes from Stellar Streams studies. Stellar streams are groups of stars that were once a globular cluster or a dwarf galaxy torn apart and whose remnants now rotate outside the galaxy plane. The analysis of the data of the GD-1 stream [36, 37] showed several substructures that cannot be explained only in terms of baryonic matter. The presence of a Dark Matter sub-halo perturbing the stream is necessary to account for such structures.

1.2 Dark Matter Candidates

From the evidence collected in the previous section, it is possible to write a list of characteristics which a Dark Matter candidate should have:



(a) Distribution of temperature anisotropies with respect the black body radiation with $T=2.72548$ K, in grey the removed contour of the galaxy disk foreground is shown.



(b) Top: Coefficient of the multipole expansion in spherical harmonics of the CMB anisotropies, with the fit superimposed. Bottom: the fit residuals of the top part of the plot.

Figure 1.3: Some of the result obtained by Planck, in (a) there is the spatial distribution of the anisotropies, while in (b) there is the coefficients of the multipole expansion with the best fit obtained by the Planck collaboration assuming the Standard Cosmological Model [30].

Long lived Since Dark Matter affects the CMB (380'000 years after the Big Bang) and is present today, it should be stable or at least have a lifetime

of the same order of magnitude of the age of the Universe.

Weakly interacting The Bullet Cluster showed that the Dark Matter/nucleon or Dark Matter/Dark Matter cross-section is *weak*, namely, of the same order or smaller than the typical weak interaction. Nevertheless, Dark Matter is not necessarily related to Z and W^\pm gauge bosons.

Chargeless The lack of interaction with the galactic plasma shown in the Bullet Cluster and its dark nature require Dark Matter to be chargeless.

Non-baryonic The CMB measurement and the Big Bang Nucleosynthesis strongly disfavour a baryonic nature of the Dark Matter.

Cold To have the structures we see in today's Universe, Dark Matter needs to be cold: only with this condition, a gravitationally bound system can form starting from the primordial density fluctuations.

All the information listed above does not make the search for Dark Matter any easier. During the last years, several candidates have been proposed in a variety of different models spanning 51 orders of magnitude in mass and 63 order of magnitude in cross-section, as shown in Figure 1.4

1.2.1 Neutrinos

As the first possible explanation for the Dark Matter paradigm, neutrinos were proposed since they are the only Standard Model particle with all the characteristics listed above for a Dark Matter candidate. However, the measurement obtained by the Planck collaboration [31] shows that the relic neutrino abundance is not sufficient to explain Dark Matter. Although standard neutrinos do not suit as Dark Matter candidates, exotic neutrinos (sterile neutrinos, heavy right-handed neutrinos), introduced to solve the neutrino mass problem, can work as Dark Matter candidate [39]. For example, to explain neutrino mass, some models introduce a massive right-handed neutrino, which does not interact with the Z/W^\pm boson and can be a suitable Dark Matter candidate. These kinds of neutrinos are referred to as *sterile neutrinos*. A more detailed review of sterile neutrino as a Dark Matter candidate can be found in [40].

1.2.2 WIMPs

The Weakly Interacting Massive Particles (WIMPs) are a general class of particles with a mass between $10 \text{ GeV}/c^2$ and a few TeV/c^2 . The interest in the WIMPs arise from the measurement of present relic Dark Matter density :

$$\Omega_\chi h^2 \approx \frac{3 \times 10^{-27} \text{ cm}^3 \text{ s}^{-1}}{\langle \sigma_{ann} v \rangle}, \quad (1.3)$$

where σ_{ann} is the WIMP annihilation cross-section, v the relative velocity of the

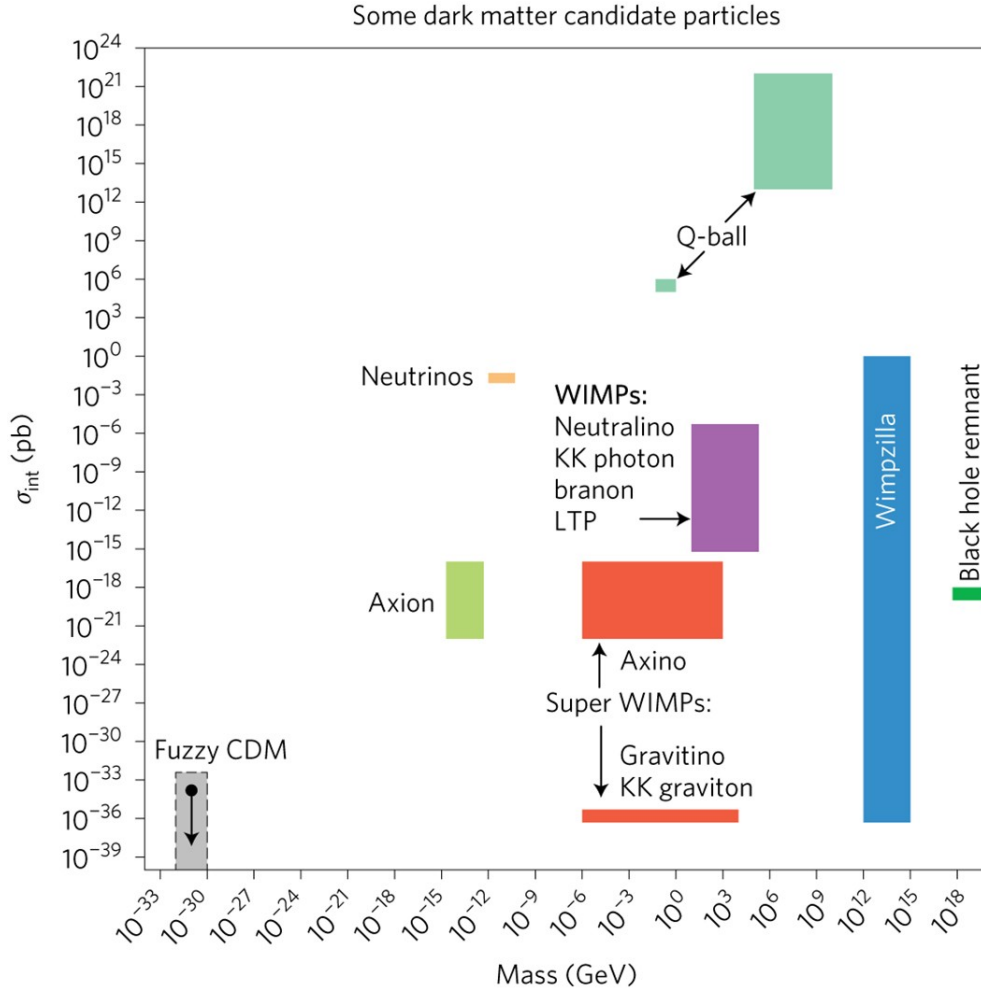


Figure 1.4: Mass and cross section for several Dark Matter candidates [38]. The wide ranges covered for both mass and cross-section can be appreciated.

annihilating WIMPs, and the angle brackets denote the average over the WIMP thermal distribution. Considering the $\Omega_\chi h^2 \approx 0.12$ measured by Planck [31], the $\langle \sigma_{ann} v \rangle \approx 3 \times 10^{-27}$ is of the same order of what expected for particle of $\sim 100 \text{ GeV}/c^2$ which interact via electroweak force. Since the standard model supersymmetric extension predicts a particle with such characteristics [41], this coincidence is often referred to as the *WIMP miracle*. Such a miracle rose the interest in this kind of candidate and gave a huge boost to the Dark Matter search. Despite the WIMP miracle appeal, many works have pointed out that there is no experimental evidence in favour of this hypothesis, and an open-minded approach is mandatory.

1.2.3 Asymmetric Dark Matter

The main motivation for Asymmetric Dark Matter (ADM) models comes from the observations that at present day baryonic and Dark Matter densities are

comparable [31] :

$$\Omega_\chi \sim 5\Omega_b. \quad (1.4)$$

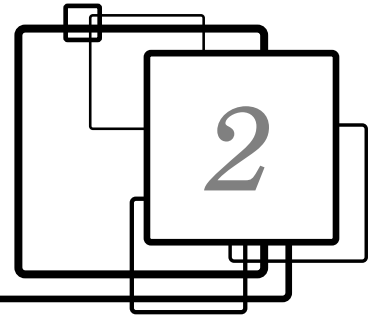
This fact suggests a possible common origin and additional connections between their cosmological evolutions.

The hypothesis behind ADM is that the same asymmetry present today between matter and anti-matter also occurred in the dark sector, leading to a higher abundance of Dark Matter particles than Dark Matter anti-particles in today's Universe. The predicted mass for the asymmetric dark matter varies from the sub-GeV/ c^2 to tens GeV/ c^2 [42, 43].

1.2.4 Axions

Axions are a kind of particles hypothesized to solve the strong CP problem corresponding to the fact that the strong interaction does not violate the CP symmetry even if, according to the QCD theory, such violation is allowed. A solution to the problem for the non-violation of CP symmetry is the Peccei-Quinn mechanism [44, 45]. The extension of the Axion hypothesis beyond the strong CP problem gives birth to the so-called Axion Like Particles. Such particles are present in several Beyond Standard Model theories [46] and considered suitable Dark Matter candidates thanks to their general properties [47]. Predicted mass for axions varies from the μeV to the meV range.

Because of the variety of models spanning several orders of magnitude in both mass and cross-section is not astonishing that Dark Matter is searched thorough different channels and with different techniques. In the next Chapter, an overview of the different experimental approaches exploited to detect Dark Matter is given. The most common techniques used in direct Dark Matter search are briefly presented and discussed.



The hunt for Dark Matter

Despite the considerable evidences for Dark Matter described in the previous Chapter and the scientific community efforts during the last decades, no direct observation of Dark Matter has been performed. The investigation on Dark Matter is done looking at its interaction with Standard Model Particles, and there are three ways to do it, as illustrated in Fig. 2.1

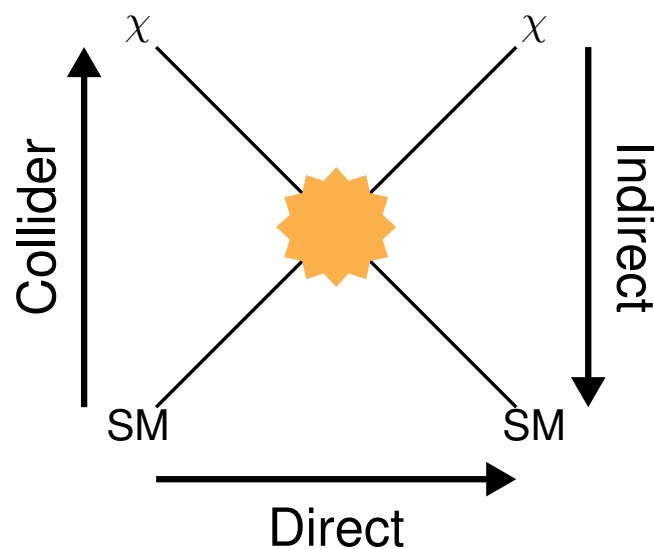


Figure 2.1: The figure shows the three ways used to search for Dark Matter Interactions (χ in figure) with Standard Model particles (SM in figure); the arrows indicate which interactions is looked for in the various searches according to what the incoming and outgoing particles are.

2.1 Dark Matter search approaches

2.1.1 Collider search

Particle accelerators are one of the most powerful tools that physics has nowadays to explore particle properties. Today the most advanced accelerator is the Large Hadron Collider (LHC) located at CERN, which can generate maximum energy

of 14 TeV in the center of mass frame. This collider could reproduce the very first moment of the Universe when it was in a hot and dense state.

The typical signature of an extremely weakly interacting particle in this kind of detector is the so-called *missing transverse energy* (MET). Such particles escape from the interaction region, producing no signal in the detectors and leaving the total energy apparently not conserved as expected from the energy and momentum conservation laws.

If the dark matter particles were light enough to be produced at LHC, they would pass unnoticed through the detectors. Leading to a final state with no particles detected at all, making the *missing energy* method pointless. Consequently, the minimal request to detect Dark Matter particles at colliders is their production with at least one hadronic jet. The event signature is the detection of a single energetic jet paired with missing energy and transverse momentum.

It is fundamental to underline that even if a particle with all the characteristics listed in Section 1.2 is detected at the collider, it would not be sufficient to state it is a Dark Matter particle. Direct observations in the galactic halo will be necessary.

For a more detailed review of the Dark Matter search performed at the collider, see [48].

2.1.2 Indirect search

Considering the amount of Dark Matter present in the Universe, there is a finite probability that Dark Matter particles annihilate or decay, producing Standard Model particles that are detectable. This kind of Dark Matter search is usually performed looking for excess in gammas, neutrinos, anti-protons, and positrons distributions.

Gammas and neutrinos Dark Matter could annihilate or decay and produce gammas or neutrinos. Since neutrinos and gammas are chargeless, they do not interact with magnetic fields, making it possible to pinpoint their source.

The probability of observing an annihilation process is larger in a high-density region. For this reason, the sky region close to the galactic center is observed. In this way, the high-density request is satisfied, and the detector saturation due to galactic center luminosity is avoided.

Neutrinos are searched by experiments like SuperKamiokande [49] and ICEcube [50], which use a large amount of water (ice in the case of ICECube). Neutrinos interaction with electrons or nuclei of water molecules can produce Čerenkov light. The detection of such radiation would reveal neutrino presence, allowing to measure properties like energy and direction, for example.

On the other hand, gammas are investigated with an experiment like Fermi

[51], a space observatory used to perform gamma-ray astronomy observations from low Earth orbit.

Recently, the Fermi collaboration measured an unexpected excess in gamma-ray radiation from the Milky Way galaxy center [52]. Today, there is still no accepted explanation for this excess. However, dark matter self-annihilation processes have been proposed as possible sources for the excess [53, 54].

Positrons and Anti-protons their interaction with the galactic magnetic field prevents tracking their origin. Nonetheless, detecting an unexplainable excess in the positrons and anti-proton energy spectrum in terms of known sources is a valid method to probe Dark Matter. Such spectra are measured with cosmic ray telescopes like AMS [55] and DAMPE [56]. The first is located on the ISS, while the latter is a satellite launched at the end of 2015. These cosmic ray telescopes are optimized for positrons and electrons and look for excess in the positron spectrum.

2.1.3 Direct search

Direct search experiments rely on the hypothesis that Dark Matter interacts with ordinary matter at a weak (or sub-weak) scale. Earth-bounded experiments aim to measure electron or nuclear recoils induced by Dark Matter particles interacting into the detector. Since the expected rate is extremely low, cosmic radiation represents a primary source of background. For this reason, such experiments are placed in deep underground facilities where cosmic radiation flux is reduced by several orders of magnitude.

2.2 Dark Matter Interaction Rate

As discussed in the Sec 1.1, galaxies are surrounded by a Dark Matter halo. Since the idea behind the direct dark matter search is that particles from halo interact with the target nuclei in the detector, the halo model is a crucial point for the expected Dark Matter rate calculation. There are numerous models to describe the formation of Dark Matter halos. One of the most commonly used models for galactic Dark Matter halos is the spherical pseudo-isothermal halo [57]. With this model, it is possible to evaluate the Dark Matter density at a certain radius. For example, the local Dark Matter density in the Earth proximity is $0.3 \text{ GeV}/c^2 \text{ cm}^{-3}$ [58].

Another critical point is that the relative velocity between the Dark Matter particles and the detector is the only relevant kinematic parameter for the scattering process. Finally, we will describe the elastic Dark Matter rate calculation in the hypothesis of a spin-independent interaction as it is the relevant one for the CRESST experiment. For testing spin-dependent processes, a considerable amount of target nuclei with non-zero spin is needed.

For what concerns the CRESST target, the only nucleus that would probe a light Dark Matter spin-dependent interaction is the isotope ^{17}O . Unfortunately, its abundance is extremely low (0.038%), and CRESST main focus is, therefore, on the spin-independent interaction. The measured quantity in direct search experiment is the differential rate N as a function of the nuclear recoil energy E_R for unit mass that is given by:

$$\frac{dN}{dE_R dM} = n_\chi N_T \int_{v_{min}}^{v_{max}} v f(\vec{v}, \vec{v}_e) \frac{d\sigma}{dE_R} d^3v, \quad (2.1)$$

where n_χ is the local numerical Dark Matter density given by $n_\chi = \rho_\chi/m_\chi$, ρ_χ is the local Dark Matter density, N_T is the number of target nuclei, v_e and v are the Earth and DM velocity in the galactic Earth frame, $f(\vec{v}, \vec{v}_e)$ is the Dark Matter velocity distribution, and $d\sigma/dE_R$ is the differential cross-section for dark matter scattering off a nucleus. The integral is evaluated between v_{min} , which is the minimum velocity for a nuclear recoil with energy E_R and v_{max} that is the maximum velocity in the laboratory frame. For the terms inside the integral, some details are in the following subsections.

2.2.1 Velocity distribution

According to all the information collected with the experimental observations (see Sec. 1.1), two basic conditions must be satisfied by Dark Matter particles of the halo. Firstly they must have a non-zero velocity; otherwise, they would have collapsed toward the galaxy center. At the same time, their velocity must be low enough to keep them confined in the galaxy.

Several models have been developed to describe the particles velocity inside the halo, but the distribution that is used most often in the literature is the truncated Maxwellian, also known as Standard Halo Model. In detail, the velocity distribution $f(\vec{v}, \vec{v}_e)$ is described by a Maxwell-Boltzmann distribution with a cut-off at the escape velocity from the galaxy [59]:

$$f(\vec{v}, \vec{v}_e) = \frac{1}{\mathcal{N}(v_0, v_{esc})} \exp\left(\frac{v^2 + v_e^2 + 2vv_e \cos\theta}{v_0^2}\right), \quad (2.2)$$

where θ is the angle between Earth's and dark matter's velocity in the galactic rest frame, v_0 is the orbital velocity of the Sun around the galactic center. The sharp cut-off is needed to consider only particles gravitationally bounded to the galaxy. The normalization factor $\mathcal{N}(v_0, v_{esc})$ is given by:

$$\mathcal{N}(v_0, v_{esc}) = \pi^{3/2} v_0^3 \left[\operatorname{erf}\left(\frac{v_{esc}}{v_0}\right) - \frac{2v_{esc}}{\sqrt{\pi}v_0} e^{-v_{esc}^2/v_0^2} \right] \quad (2.3)$$

where the Earth velocity is given by:

$$v_e = v_0 + 15 \cos\left[\frac{2\pi}{365 \text{ days}}(t - 152 \text{ days})\right] \text{ km/s.} \quad (2.4)$$

The phase of the cosine is set to 152 days that corresponds to the 1st of June. On this date, the Sun velocity is aligned with the Earth one, maximizing the incoming Dark Matter flux.

In this way, the Earth motion around the Sun creates a distinctive feature in the Dark Matter expected signal: an annual modulation used as a smoking gun to identify the DM signal [60].

2.2.2 Cross section

The other term present in the integral is the differential cross section. The most general cross section for a spin-independent energy spectrum, is given by:

$$\frac{d\sigma}{dE_R} = \frac{\sigma_n m_N}{v^2 2\mu_n^2} \frac{[Zf_p + (A - Z)f_n]^2}{f_n^2} F^2(E_R), \quad (2.5)$$

where σ_n and μ_n are the dark matter-nucleon cross-section and reduced mass, A , and Z are the atomic mass number, and the proton number of the target nuclei, f_p and f_n parameterize the different coupling for DM-neutron and DM-proton. $F(E_R)$ is the nucleus form factor, which takes into account the nuclear structure that cannot be considered point-like given the high transferred momentum $q = \sqrt{2m_N E_R}$ in the DM - nucleus scattering. Lots of different parameterization can be found to describe the form factors. In this work, the widely used Helm form factor [61] parameterization is used:

$$F_H^2(E_R) = \left(\frac{3j_1(qr/\hbar)}{qr/\hbar} \right)^2 e^{-s^2 q^2/\hbar^2}, \quad (2.6)$$

where j_1 is the first spherical Bessel function, $r = \sqrt{r_n^2 - 5s^2}$, $s = 1$ fm, and $r_n = A^{1/3}$ fm.

Assuming the same coupling for neutrons and protons ($f_n = f_p$), the cross-section reduces to

$$\frac{d\sigma}{dE_R} = \frac{\sigma_n m_N}{v^2 2\mu_n^2} A^2 F_H^2(E_R). \quad (2.7)$$

It is possible to notice the peculiar feature of the A^2 dependence of the cross-section, favoring heavy nuclei.

We have all the elements to calculate the energy spectrum of the recoils induced by DM scatterings. The expected energy spectra for CaWO_4 , which is the compound relevant for the analysis portrayed in this work, are shown in Figure 2.2.

Figure 2.3 shows the number of expected events as a function of the Dark Matter mass, for a CaWO_4 detector with a finite energy threshold. It is crucial to notice that despite the A^2 dependence of the cross-section, tungsten is disfavoured to explore light Dark Matter mass because of the energy needed to have a recoil above the threshold. On the other hand, oxygen due to lighter mass is preferred for low mass Dark Matter analysis. The CRESST approach that

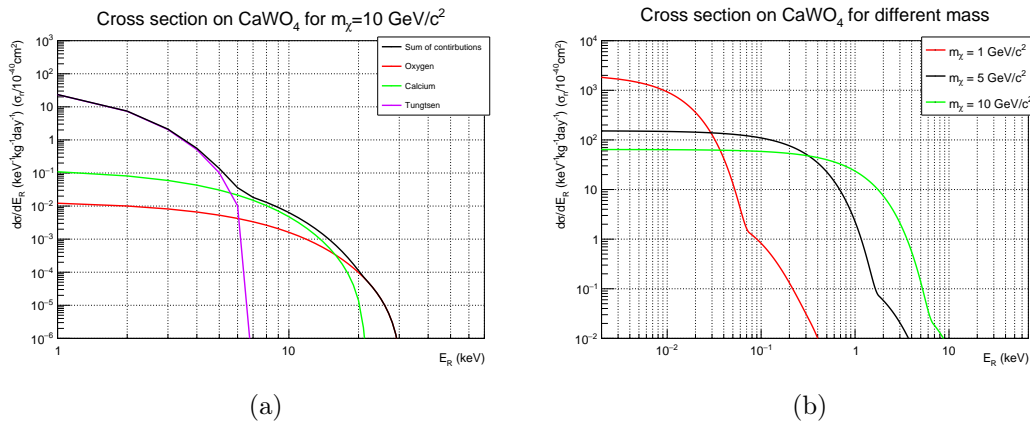


Figure 2.2: The two figures illustrate the differential rate for the calcium tungstate, showing as the different element or the different Dark Matter mass influence the shape of the expected spectrum. Figure (a) shows how the different elements in the CaWO₄ contribute to the total energy spectrum; it is clear that the energy spectrum is dominated by the tungsten cross section because of its high A . Figure (b) shows the total differential rate on CaWO₄ for different Dark Matter masses.

uses detectors with different elements makes the experiment capable of exploring different DM mass regions.

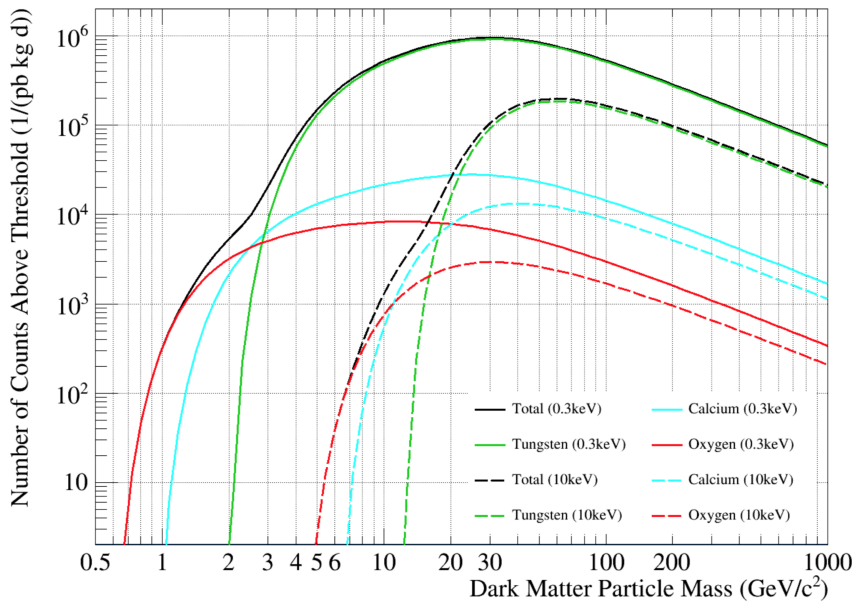


Figure 2.3: The figure shows how the effect of a finite threshold affects the Dark Matter lowest detectable mass. Solid lines show the effect of a threshold of 0.3 keV for a calcium tungstate detector. Dashed lines show the effect of a 10 keV threshold. With the different colour are shown the different contribution, black for total, red for oxygen, cyan for calcium and green for tungsten.

2.3 Experimental approaches for direct search

Considering the extremely faint interaction of Dark Matter particles, it is fundamental to have a target mass as large as possible for direct Dark Matter search. The use of large target mass would maximize the number of target nuclei and, consequently, the observed event rate. Moreover, a very low energy threshold is needed to detect the nuclear recoils, whose typical energies go from tens of eV to tens of keV. Due to the very low expected rate, abating as much as possible, all the background sources is crucial. This is achieved with passive techniques, namely installing massive shielding around the detectors and active techniques that allow for proper particle identification and rejection of background events. The particle identification can be achieved by detecting multiple signals produced inside the target material, such as the heat, scintillation light, and ionization.

The most used detectors for direct Dark Matter search are Time Projection Chambers (TPCs) with liquid noble gases, cryogenic detectors, and scintillating crystals.

2.3.1 Cryogenic Detectors

The cryogenic detectors are a class of devices operated at milliKelvin temperatures. The detector consists of the main absorber equipped with a sensitive thermometer. A particle interaction deposits a large fraction of its energy in the absorber in the form of phonons. Depending on the absorber material, a small part could be released in ionization or scintillation. The combined measure of two channels (phonon/ionization or phonon/scintillation) allows discriminating the electron/gamma background from the nuclear recoils, possibly induced by Dark Matter. Present experiments using heat and ionization are for example SuperCDMS [62] and EDELWEISS [63]. They are based on semiconductor detectors, where an interaction produces a heat signal and hole-electron pairs collected thanks to an electric field. CRESST is based on the simultaneous detection of scintillation light, and heat [64], a more detailed description of the CRESST working principle is reported in Section 3.2.

The main advantage of cryogenic detectors is the performances in terms of energy resolution and threshold. Both CRESST and EDELWEISS have shown thresholds below 100 eV, making them especially suitable for light Dark Matter search. The downside of these detectors is the technical complexity, making it very difficult to scale to large masses. Currently CRESST has the best sensitivity in the $0.16 \div 1.7 \text{ GeV}/c^2$

2.3.2 Liquid Noble Gas TPCs

Several WIMP mass search experiments use liquid noble gas in dual-phase TPCs. Noble gases are known to be extremely good scintillators. They have a very high scintillation yield, and they are transparent to their radiation, which is emitted mainly in the UV region. These experiments typical layout includes a vessel

filled with noble gas in both liquid and gaseous phase, with two arrays of PMTs on the top and on the bottom of the vessel.

A Dark Matter interaction inside the experimental volume generates a scintillation signal (S1) and ionization electrons. An electric field applied along the vessel drifts the electrons toward the interface between the liquid and the gas phase. Here the electrons extracted from the liquid phase accelerate in the gas and cause a second scintillation signal (S2). The S2 signal is amplified compared to S1 thanks to the avalanche having place in the gaseous phase. The use of signal S2 allows locating the event in the $x - y$ plane while using the time difference between the S2 and S1 signals is possible to quantify the z of the events. The 3D reconstruction of the event location permits to define an inner fiducial volume and to reject events close to the vessel surface (that is usually less radio-pure than the liquid noble gas). The ratio S2/S1 is used to discriminate electron/gamma background from the nuclear recoils produced by DM interactions. The scalability of this type of detector is relatively easy, and therefore they have presented the best sensitivities in a typical WIMP scale between $10 \text{ GeV}/c^2$ and $1 \text{ TeV}/c^2$.

The vessel is usually placed inside a water tank equipped with PMTs. The water tank is used as passive shielding against gammas and neutrons and as an active veto for muons.

In Figure 2.4 a schematic view of the dual phase TPCs operating principle is shown. Present experiments using this approach are LUX [65] PandaX - II [66] and XENON1T [67] with liquid Xenon, and DarkSide [68] with liquid Argon.

Because of the different mass numbers, the expected rate due to a Dark Matter scattering is higher for Xenon compared to Argon. Concerning the radiopurity, Xenon does not contain radioactive isotopes apart from the double beta emitter ^{136}Xe . Atmospheric Argon contains traces of two radioactive isotopes ^{39}Ar and ^{42}Ar produced by cosmic rays. The most intense source of background for Argon TPCs comes from ^{39}Ar , which is characterized by a ratio of ^{39}Ar over ^{40}Ar of $8.1 \times 10^{-16} \text{ g/g}$. This ratio can be extremely reduced, extracting Argon from underground wells. Finally, the scintillation light produced by pure Liquid Argon and Liquid Xenon has two decay components due to the de-excitation of singlet and triplet states. The pulse shape depends on the type of incident particle, and such discrimination is particularly effective for Argon since the separation between the two decays is larger than the Xenon one [70].

The main advantage of Liquid Noble Gas TPCs is the scalability to large volumes (current generation is already in the multi tonnes scale). Noble gas radiopurity and fiducialization permit to reach extremely low background values. The only limitation of these detectors is that the dual-phase mode threshold cannot reach very low values. At present time the sensitivity above $5 \text{ GeV}/c^2$ is dominated by liquid Xenon TPCs (LUX [65], XENON1T [67], PandaX-II [66]).

2.3.3 NaI experiments

Several Dark Matter experiments are based on the use of high purity NaI(Tl) crystals. NaI crystals are known to be excellent Dark Matter detectors as they

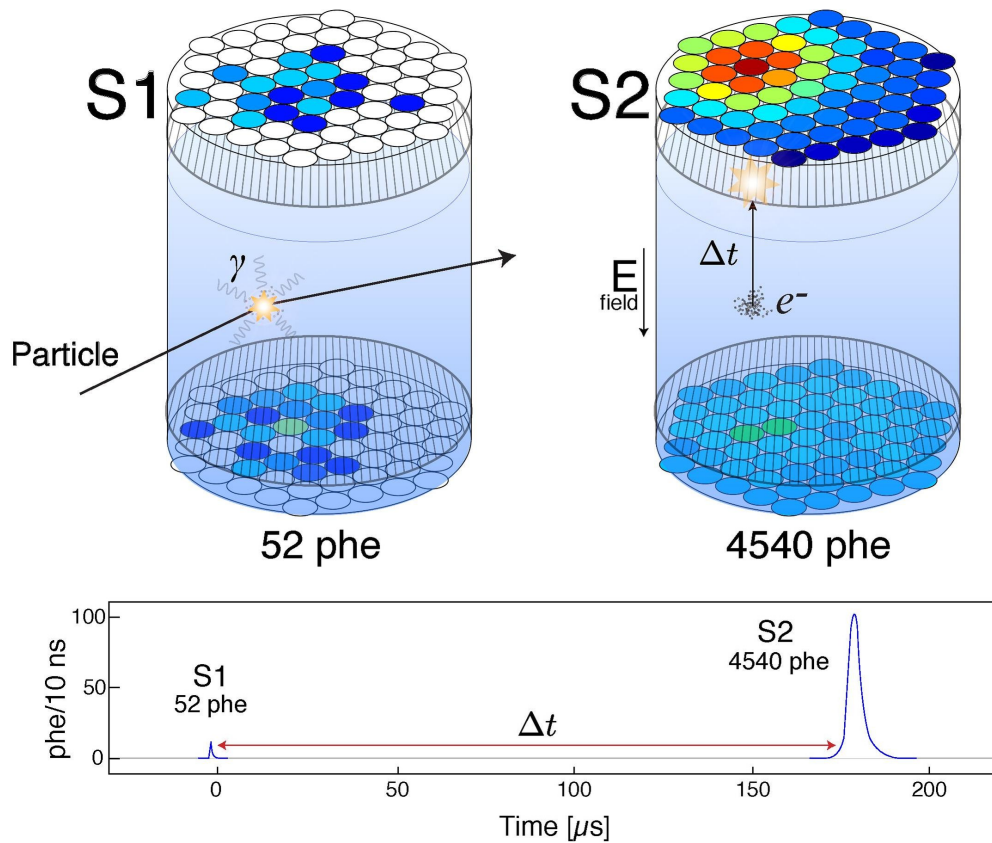


Figure 2.4: The figure shows the interaction of a particle inside TPC and the production of the two scintillation signals S1 and S2, [69].

have a very high scintillation yield. Large ingots can be grown from high-purity sodium iodide, and unusual shapes and sizes can be obtained by pressing small crystals together [71]. One of the main difficulties in reaching a high level of radio-purity comes from the presence of potassium that always accompanies sodium in alkali halides. The isotope ^{40}K in fact has a half-life of 1.29×10^9 y and it can decay β^- into ^{40}Ca (89.28%) or via electron capture into ^{40}Ar (10.72%) [72]. The most notorious experiment is DAMA/LIBRA, which is the only one that detected an annual modulation signal with the characteristics expected for a Dark Matter candidate with a significance of 12.9σ [73]. Figure 2.5 shows the modulated DAMA signal.

The DAMA/LIBRA collaboration results are in strong tension with the results of several other experiments in the assumption of the simplest model for the galactic halo and the interaction. On the other side, presently, no alternative explanation of the DAMA/LIBRA signal has been found. Therefore proving the DAMA/LIBRA signal with the same type of detector is mandatory to fully understand this effect.

For this reason, several NaI-based experiments have been realized to cross-check the DAMA/LIBRA signal. While a signal confirmation at the same labor-

atory is desired to exclude experimental effects, a measurement at different laboratories could give information on the possible origin of the modulation [74]. The SABRE experiment located at LNGS consists of highly pure NaI(Tl) crystal in an active liquid scintillator veto to tag and reduce ^{40}K background from the crystal as the external background. It is currently under construction, and it will start to take data in the next few years [75]. Both COSINE and ANAIS have a similar design. COSINE is located at Yangyang underground laboratory in Korea, and it is currently operating 106 kg NaI(Tl) target material [76]. ANAIS is located at the Canfranc Underground Laboratory and operates a 25 kg NaI(Tl) detector [77].

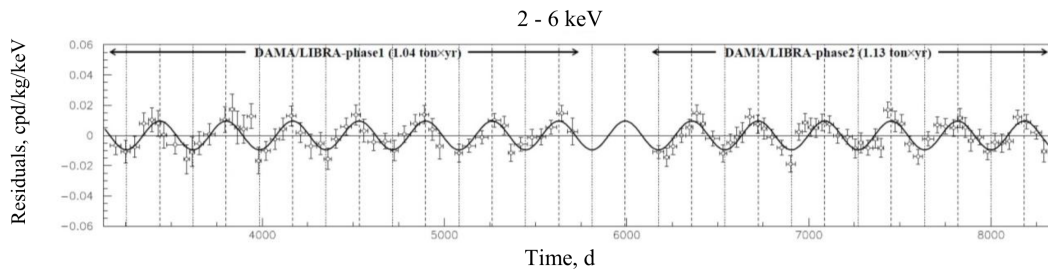


Figure 2.5: The figure shows the DAMA/LIBRA signal oscillation along 13 years [73]

2.3.4 Directional experiments

The last type of direct search experiments discussed is directional experiments. In its revolution around the galaxy, the Solar system moves toward the Cygnus constellation, creating an apparent Dark Matter flux from the Cygnus.

These experiments aim to identify the direction of the Dark Matter particle interacting in the detector to confirm the origin of the signal through this peculiar signature. This technique could substantially reduce the background and probe Dark Matter below the neutrino floor, an unavoidable background due to Sun neutrinos elastically and coherently scattering with the nuclei [78]. Some of the experiments of this type are NEWSdm [79] MIMAC [80] and CYGNUS [81], but their sensitivity is still far to be competitive with noble gas TPCs.

In Figure 2.6, the most recent results for the Dark Matter direct search are plotted. Results labeled with (M) are obtained with the Migdal [82, 83] effect and are not included in the explored region since this effect has not been experimentally observed yet.

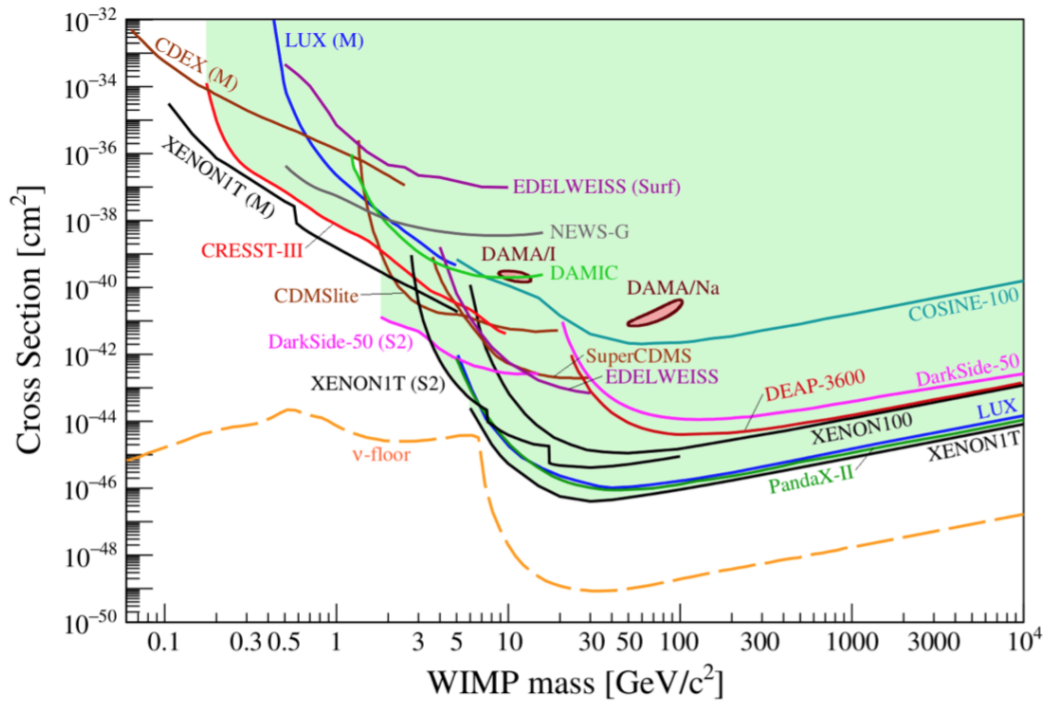
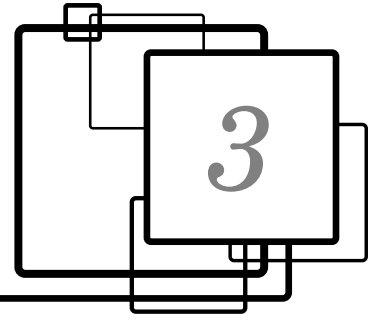


Figure 2.6: Current status of searches for spin-independent elastic WIMP-nucleus scattering assuming the standard parameters for an isothermal WIMP halo is shown in green. Results labeled M were obtained assuming the Migdal effect [82, 83] and are not considered since this effect has not been experimentally observed yet. Plot from [84]. Credits to M.Schumann.



The CRESST experiment

The goal of the CRESST (Cryogenic Rare Event Search with Superconducting Thermometers) experiment is to detect Dark Matter particles via their elastic scattering on target nuclei in the absorber of a cryogenic detector. CRESST, located in the underground site of Laboratori Nazionali del Gran Sasso (LNGS), uses CaWO_4 4 absorber crystals equipped with tungsten superconducting sensors to detect possible Dark Matter interactions. Each detector is coupled with a sapphire cryogenic detector (also equipped with W sensor) to measure the scintillation light, emitted by particle interactions in CaWO_4 , and provide information on the radiation type. This chapter presents a general overview of the CRESST experimental setup, of the detectors working principle, and of the most recent results. The CRESST infrastructure, described in Sec.3.1, includes not only the cryogenic system necessary to provide the working temperature for the detectors, but also all the array of active and passive shields to suppress the different components of the background. As described in 2.1.3 to reach the sensitivity for Dark Matter detection, the CRESST detectors need to be shielded from cosmic rays and from any possible source of background (mainly natural radioactivity) that can mimic or disturb the identification of a Dark Matter signal. Sec 3.2 describes the working principle of the CRESST detector together with the readout and operation details. Finally, the CRESST most recent results and achievements are reported, compared with the most sensitive competitors.

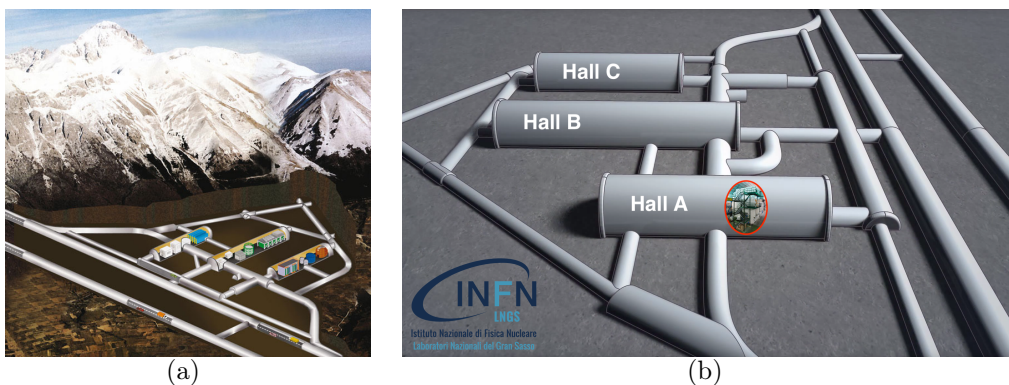


Figure 3.1: A schematic view of the underground facility of LNGS. On the left, it is possible to see the laboratory position in the highway tunnel and the three main experimental halls. On the right, the position of the CRESST hut in the Hall A.

3.1 Background and shielding

The primary background sources and how they are shielded in the CRESST experiment are illustrated in this Section. Figure 3.3 shows a schematic drawing of the experimental setup, whose details will be discussed in the following subsections. The most relevant background sources are electrons, gammas, and α s from natural radioactivity and neutrons due to environmental contaminations or muon induced. More details on the different backgrounds will be illustrated in this Chapter.

3.1.1 Muon background

For a rare event experiment, the main background source on the Earth's surface is due to muons generated by the decay of particles produced by cosmic ray protons interacting with the nuclei of Earth's atmosphere. The muon flux at the sea-level is $\sim 100 \div 200$ particles per $\text{m}^{-2}\text{s}^{-1}$ [39], making impossible any rare event search above ground. For this reason, every low background experiment should be placed deep underground.

CRESST is located at the underground facility of *Laboratori Nazionali del Gran Sasso* (LNGS) in central Italy, in the heart of Abruzzo region, beneath the Gran Sasso mountain (Fig. 3.1). The mountain offers a rock shield of at least 1400 m (3800 meters of water equivalent) in all directions reducing the muon rate by a factor $\sim 10^6$. The most accurate measurement of the muon flux inside the laboratory was obtained by the Borexino experiment and corresponds to $(3.41 \pm 0.01) \cdot 10^{-8} \text{ cm}^{-2}\text{s}^{-1}$ [85] (Fig 3.2).

In addition to the rock shielding, to identify possible signals induced by muons, plastic scintillator panels surround the CRESST experiment for an active muon veto.

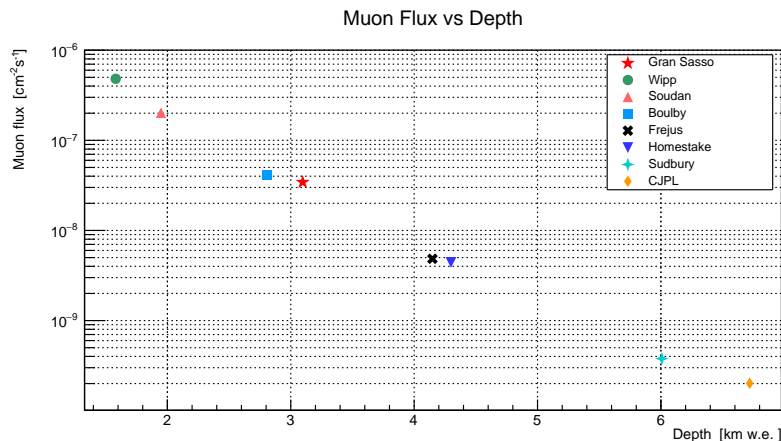


Figure 3.2: Reduction of the muon flux rate with depth for different underground laboratories around the world. In order to compare laboratories surrounded by different rock types that offer different shielding all the depths are given in water equivalent kilometers. The plot is obtained using data from [85], [86] and [87].

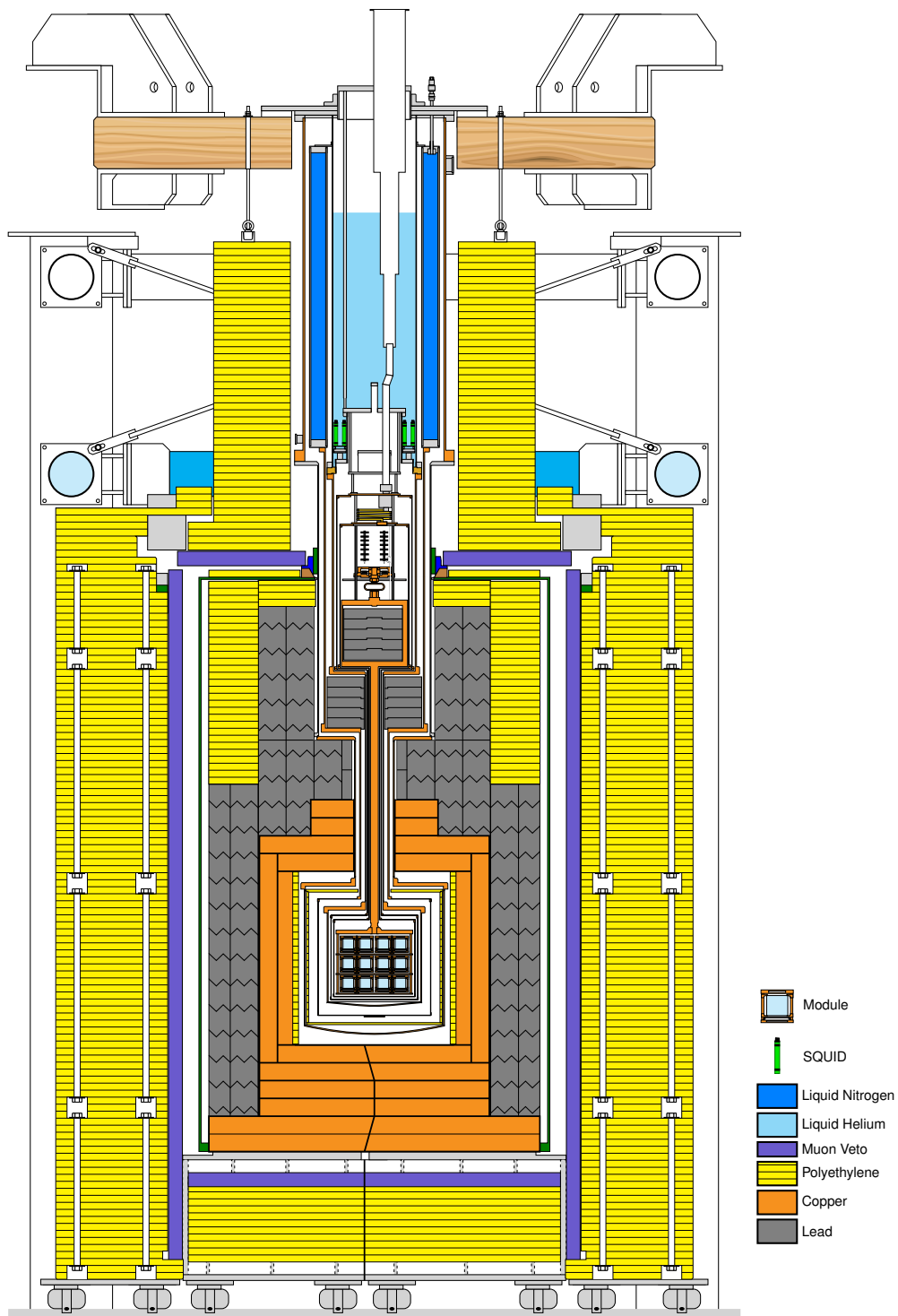


Figure 3.3: Schematic view of the experiment, showing the various shielding and the cryostat structure. The cryostat custom design allows a more effective shielding of the experimental volume. A 1.5 m long copper bar, named *cold finger*, is used to protect the detector from the cryostat operating parts (which cannot be realized only with radio-clean materials). This configuration allows an almost 4π coverage of the detectors with copper, lead, and polyethylene shields.

3.1.2 Neutron background

Neutrons are one of the most dangerous backgrounds for any dark matter search. Due to their ability of penetration and their chargeless nature, neutrons may go undetected into the innermost part of the detectors, eventually resulting in a signal that could mimic a dark matter-nucleus interaction.

Neutrons in deep underground facilities are produced by interaction of cosmic muons (spallation) in the rocks or by α -n reactions due to the natural radioactivity of the surrounding rocks. The neutron flux induced by cosmic muons interacting in the rocks, $2.72 \cdot 10^{-9} \text{ cm}^{-2}\text{s}^{-1}$ [86], and the neutron flux due to α -n reactions in the surrounding rocks, $(3.2 \pm 0.1) \cdot 10^{-7} \text{ cm}^{-2}\text{s}^{-1}$ [88], are mitigated by a passive shielding. For cinematic reasons light elements are the most efficient neutron moderators, therefore three different polyethylene¹ layers are used for this scope, see Figure 3.3.

While the external layer shields from neutrons produced by cosmic muons and natural radioactivity, the two thinner internal layers shield the experimental volume from neutrons coming from α -n reactions happening in lead and copper shielding as well as in the copper thermal shields of the cryostat.

Neutrons produced by cosmic muons interacting in the copper or lead shielding can be tagged with a muon veto coincidence signal.

3.1.3 Natural radioactivity chains background

The other main sources of background are ^{40}K and the three natural decay chains of the ^{238}U , ^{235}U , and ^{232}Th . Isotopes originated from these three series are present in traces in any material surrounding the detectors.

The background contaminations outside the detector are reduced thanks to massive shielding; the background originated in the experiment innermost part is identified and removed during the analysis process.

The background reduction, from the surrounding environment contamination, is achieved with different shielding material, each of them devoted to screening one type of radiation.

While any thin layer easily stops α s and β s because of their ionization energy loss, γ s lose energy via the Compton effect and can deeply penetrate any material. For this reason, high Z materials due to their large cross-section are appropriate.

Lead is one of the best choices because of its high Z and high density. Unfortunately, it is extremely challenging to avoid contamination of the unstable isotope ^{210}Pb . Consequently, an inner shield of copper, which can be purified at a level of 99.99%, is used to protect against β s and γ s originated by the external lead shield.

In Figure 3.3 is shown a schematic view of the experiment. Neutrons are suppressed thanks to the polyethylene shielding described in the previous Section.

¹Polyethylene $(\text{C}_2\text{H}_4)_n$ is a plastic material obtained from the polymerization of ethene (C_2H_4) .

3.1.3.1 Radon-222

One of the most dangerous backgrounds comes from the ^{238}U chain, specifically from ^{222}Rn . Radon is a noble gas and does not establish chemical bonds with surrounding materials. ^{222}Rn is an isotope with a lifetime of 3.82 days, which is long enough for radon to degas from ^{238}U contaminated materials. After the Radon decay, the daughter nucleus can stick on exposed surfaces, and the decay chain rapidly continues until it stops to the long-lived ^{210}Pb (22.3 y), leaving the surface contaminated.

Before reaching the stable isotope ^{206}Pb , the decay chain includes only the relatively short-lived isotopes ^{210}Bi (5.01 days) and ^{210}Po (138.4 days). After ^{210}Pb contaminates the surface, it will start to populate the ^{210}Bi and ^{210}Po . ^{210}Po will eventually reach stability with a half-life of 138.1 days.

Polonium contaminated surfaces can lead to a dangerous background for the dark matter search. In fact in the decay of ^{210}Po into ^{206}Pb with emission of an α particle. Because of the process kinematics, ^{206}Pb nucleus is produced with an energy of 103 keV while the α particle has an energy of 5.3 MeV.

Depending on where the contamination is, two different signatures are possible when the ^{206}Pb nucleus is detected. If the contamination is on the housing surface, the recoil energy detected in the absorber will be lower than 103 keV because the nucleus loses part of its energy, reaching the target crystal.

Instead, when the exposed surface is the target crystal itself, the detected recoil energy is higher than 103 keV because, in addition to ^{206}Pb , recoil energy, also part of the α energy, is deposited in the target crystal (Figure 3.4). Both these signatures can contaminate the Region Of Interest.

The level of radon at LNGS is of $50 \text{ Bq}\cdot\text{m}^{-3}$ [89] so to avoid ^{210}Po surface contamination, the experimental area inside the muon veto panels is enclosed in the so-called radon-box, an airtight box continuously flushed with nitrogen. The CaWO_4 crystals are mounted inside a fully scintillating housing, which has proved to remove from the ROI the ^{210}Po background [90].

3.1.4 Particle Identification

The particle identification is mandatory to achieve good background discrimination coming from the material close to the detector or the detector itself.

The key point for particle identification consists of associating each background source with a specific signature inside the detector. Electrons, gammas and α s are distinguished by nuclear recoils because of their different energy losses. These interactions produce distinct scintillation light signals that can be used to identify the different types of radiations. Neutrons identification is more difficult because of their Dark Matter like signature: the only possible way to identify them is through their multiple interactions in different detectors caused by their higher cross-section. More details will be given in Chapter 4.

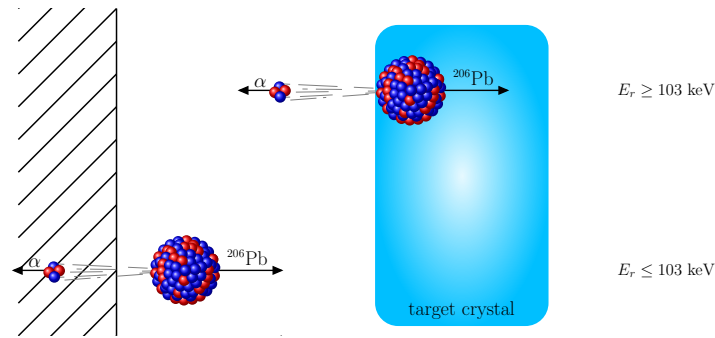


Figure 3.4: Schematic view of the decay of ^{210}Po from ^{222}Rn contaminated surface. In the decay of ^{210}Po an α (5.3 MeV) and the ^{206}Pb nucleus (103 keV) are produced. If the radon contamination is on the crystal surface, all polonium energy plus some energy of outgoing α particle (depending on the contamination depth) is deposited in the crystal. In this case, a nuclear-recoil like event with energy larger than 103 keV is measured. Instead, if the radon contamination is on the housing, the polonium deposit some energy in the housing and the rest in the crystal leading to nuclear recoil with energy smaller than 103 keV.

3.2 CRESST working principle

As introduced at the beginning of the Chapter, the aim of the CRESST experiment is the direct detection of Dark Matter particles via elastic scattering off target nuclei in CaWO_4 scintillating crystals. CRESST target consists of an array of crystals operated as cryogenic calorimeters.

3.2.1 Cryogenic calorimeters

A cryogenic calorimeter is made by an absorber equipped with a sensitive thermometer, weakly linked to a heat bath. A schematic drawing of a cryogenic calorimeter is shown in Fig. 3.5.

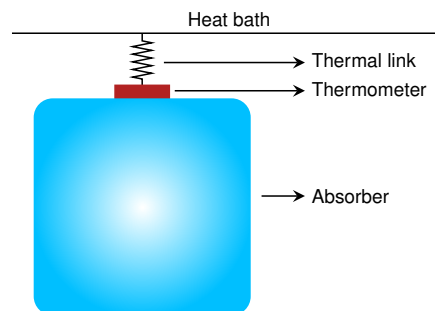


Figure 3.5: Scheme of a simple cryogenic calorimeter. Any rise in temperature due to an interaction inside the crystal is measured by the thermometer. Then everything goes back to heat bath temperature via the thermal link.

In the most naive model², any particle interaction releasing an energy ΔE inside the crystals leads to a temperature rise ΔT proportional to the energy

²a more detailed explanation based on the phonon production and collection can be found in [91]

deposited according to :

$$\Delta T = \frac{\Delta E}{C}, \quad (3.1)$$

where C is the thermal capacity of the crystal. To increase the sensitivity as much as possible, i.e., maximizing ΔT for a fixed ΔE , the heat capacity needs to be as small as possible. For CaWO_4 crystals, the heat capacity depends on the temperature according to the Debye law, and it is proportional to

$$C \propto \left(\frac{T}{\Theta_D} \right)^3, \quad (3.2)$$

where T is the temperature of the crystal and Θ_D is its Debye temperature, that corresponds to 246.5 K in case of CaWO_4 crystals [92]. Note that in Eq. 3.2 the electronic term of the Debye law, proportional to T , is missing as CaWO_4 is a dielectric.

The choice of dielectric material is very convenient to reach extremely low heat capacities since, at very low T , the electronic term becomes dominant. It is evident that to achieve the smallest capacity, the detectors need to be operated at a very low temperature ($\sim\text{mK}$).

3.2.1.1 CRESST cryogenic detector

A CRESST detector consists of two cryogenic calorimeters. The first one is a crystal made of scintillating CaWO_4 and corresponds to the main absorber used for precise energy measurement.

The second calorimeter, made of silicon-on-sapphire (SOS) wafer, is used as light detector to measure the scintillation light produced during an interaction. Figure 3.6 shows a schematic drawing of an interaction inside the detector (3.6(a)) and a picture of a CRESST detector (3.6(b)).

Since the amount of light produced is radiation dependent, it can be used to discriminate between the main background composed by electron/ γ and nuclear recoil potentially induced by dark matter. The discrimination is done with the *Light Yield* (LY) variable defined as the ratio between the energy released in the light channel and the one deposited in the main absorber ($LY = E_L/E_P$). Looking at the LY distribution as a function of the deposited energy, different bands can be appreciated, see Figure 3.7.

Each band corresponds to a different scattering process, and this happens since each interaction is characterized by a different amount of light produced.

In this way, is it possible to define bands for electron/ γ , alpha, and nuclear recoil on O, Ca, and W, and distinguish between the three different classes of interaction.

The Quenching Factor quantifies this difference in light production.

Table 3.1 shows the inverse of the QFs corresponding to the event types related to the bands of Figure 3.7. The QF of the electron/ γ processes and the

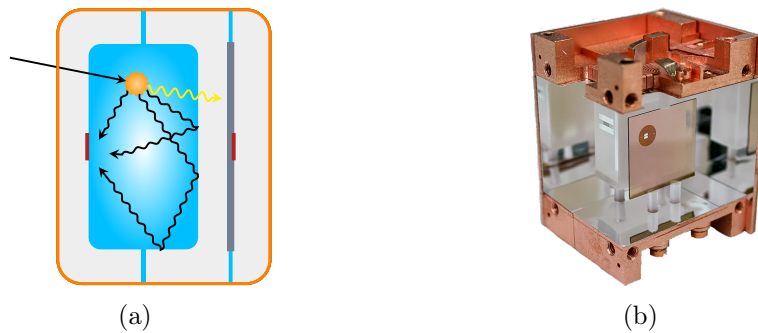


Figure 3.6: Left: A particle interaction in the scintillating absorber crystal (azure) producing light and phonons. Most of the energy is released as phonons collected by the thermometer (dark red) coupled to the crystal. A small fraction of the energy is released as light and then collected and measured by the SOS equipped with another thermometer. Right: Picture of a CRESST detector. It is possible to appreciate the two TES thermometers on the main absorber and the light detector.

corresponding band in Figure 3.7 are set to 1 by construction. More details will be given in Section 5.2.3.

Event	QF^{-1}
e/γ	1.00
α	2.7
O	8.03 ± 0.32
Ca	15.2 ± 1.0
W	51.0 ± 5.7

Table 3.1: Quenching factor for different events types. The ones of the oxygen, calcium and tungsten nuclei were measured with a dedicated run at Maier-Leibnitz-Laboratorium (MLL) facility in Garching [93] while the one for α particles is the main results of [94].

3.2.2 Signal readout

To precisely measure the small temperature rise due to a particle interaction, a very sensitive thermometer is mandatory. To achieve such sensitivity, CRESST uses Transition Edge Sensors (TES). A TES consists of a superconducting film working in its transition between the normal and superconductive phases.

With such devices, it is possible to measure the temperature rise of the order of μK for a resistance variation of the order of $\text{m}\Omega$. In Figure 3.8 an experimental transition curve is shown.

CRESST detectors are equipped with TESs made by a tungsten film with a transition temperature around 14 mK ³. Two aluminum *wings* have been de-

³The actual value of the superconducting transition depends on the deposition process and the substrate. Typical transition temperatures in CRESST are between 15 and 30 mK.

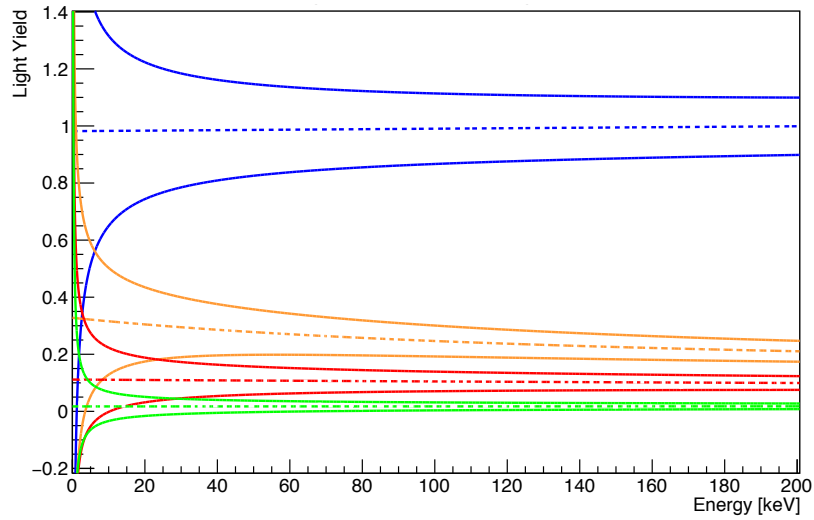


Figure 3.7: In the Light Yield vs Energy plot different bands for different types of event can be defined. The electron/ γ band normalized at $LY = 1$ is shown in blue. The oxygen and tungsten bands are depicted in red and green, respectively. The Calcium band is located between these two bands but is not shown for clarity purposes. Finally, the α band is drawn in orange.

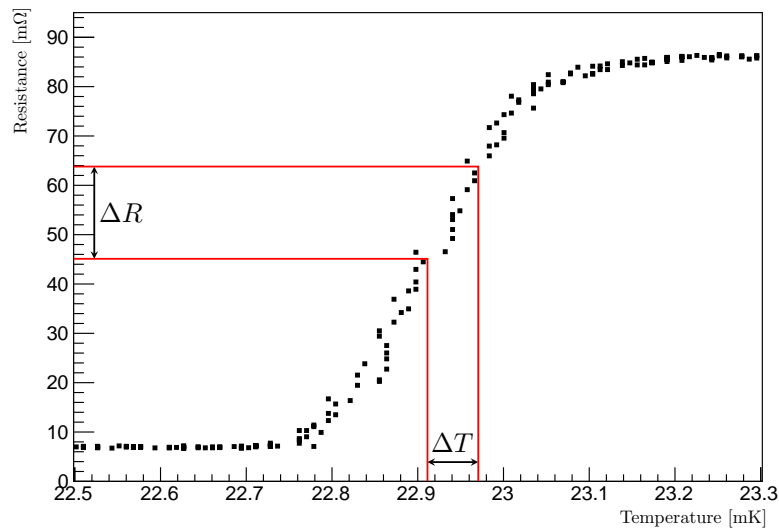


Figure 3.8: A measured transition curve. The extremely good sensitivity can be appreciated : a $\Delta T \lesssim 0.1$ mK correspond to a $\Delta R \sim 20$ m Ω

posited on each TES to maximize the phonon collection⁴ without affecting the conductive property of the sensor itself. Indeed aluminum is superconducting at the TES working temperature since its transition temperature is 1.2 K [95],

⁴ Aluminium wings are used to increase the surface/volume ratio between the TES and the crystal. In this way, a more efficient phonon collection is achieved. More details can be found in [91].

which is two orders of magnitude larger than the one of tungsten. Because of the small TES resistance, a small current of $0.1 \div 1 \mu\text{A}$ is needed.

The use of such a small current makes it difficult to measure the small variation of the TES resistance. For this reason, the TES is operated in parallel to a coil and two resistances, as shown in Figure 3.9.

Any change in the TES resistance modifies how the current split between the two branches of the circuit and, consequently, the magnetic field generated by the coil vary.

The magnetic field tiny variation is measured with very sensitive magnetometers, the Super QUantum Interface Devices (SQUID). The SQUID output signal is used to keep the SQUID flux constant thanks to the feedback circuit with a second coil and monitored by a hardware threshold trigger. In case the SQUID output exceeds a certain threshold, the signal is digitized and saved on disk.

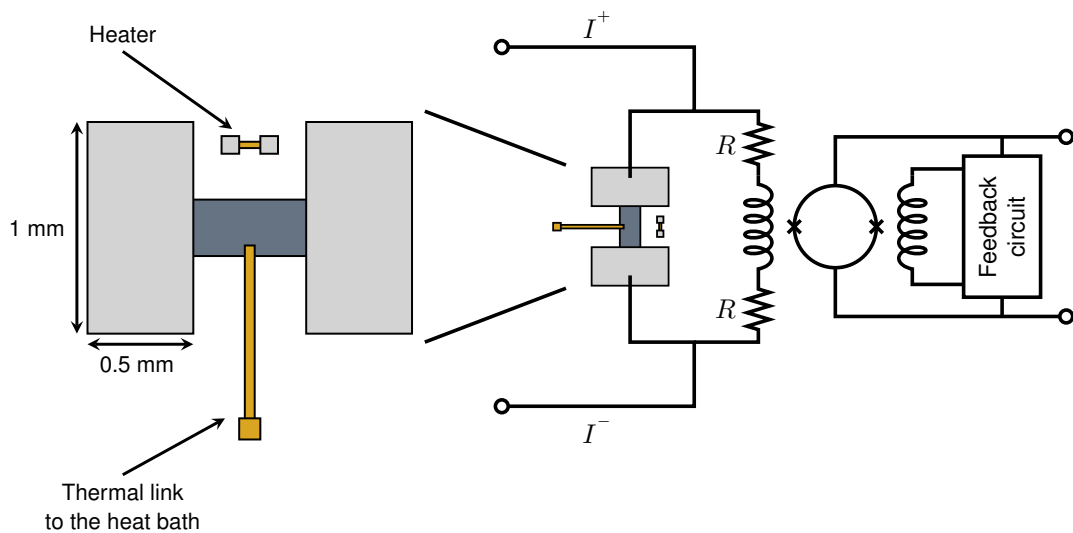


Figure 3.9: Left part: a schematic view of the TES. In the middle, there is the tungsten film (dark gray), connected with the two aluminum wings (light gray). The tungsten is connected to the heat bath via a gold thermal link. On the opposite side of the thermal link, there is the heater used to send the test and control pulses (see Sub Section 3.2.3). Right part: TES readout circuit.

Thanks to the this read-out circuit it is possible to convert the temperature rise in a voltage. As example of the final output result due to a typical particle interaction is shown in Fig. 3.10.

3.2.3 Detector operating point and response

How it can be seen from the transition curve in Figure 3.8, the TES is highly non-linear, and its response changes a lot depending on the operating point. It is crucial for stable detector operations to have a very precise working point and a good knowledge of the detector energy response. For this reason, a resistive

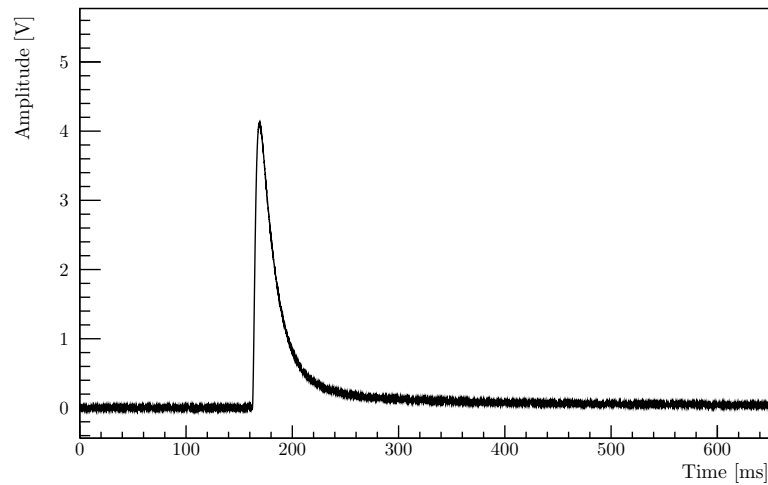


Figure 3.10: A typical record of a particle pulse signal.

heater is placed in proximity of the TES and is used to inject test and control pulses.

3.2.3.1 Control pulses

To have a stable working point, a very large pulse is injected through the heater, sending the TES completely out of the transition. Because the TES resistance-temperature flat curve above the transition, the resulting pulse will have a plateau. Measuring the pulse height is possible to determine the detector working point position and stabilize it, as shown in Fig. 3.11. The control pulses are recorded and then used during the analysis to flag unstable data taking period.

3.2.3.2 Test pulses

Another type of pulses sent through the heater is the so-called test pulses. Test pulses are sent during all the data taking with two different purposes: linearization and time monitoring.

Injecting pulses of known amplitude allows it to extend the small TES linear range and monitor in time the temperature variations of the detector and correct for their effects. Such temperature variations can affect the detector response causing different pulse height for the same energy deposition.

As the analysis procedure and the details on the treatment of the different type of pulses are widely described in the Chapters 4 and 5, they are not reported here. More details on how control and test pulse are used, together with the analysis description, can be found in Sec. 4.2. The full analysis chain is described in Chapter 4.

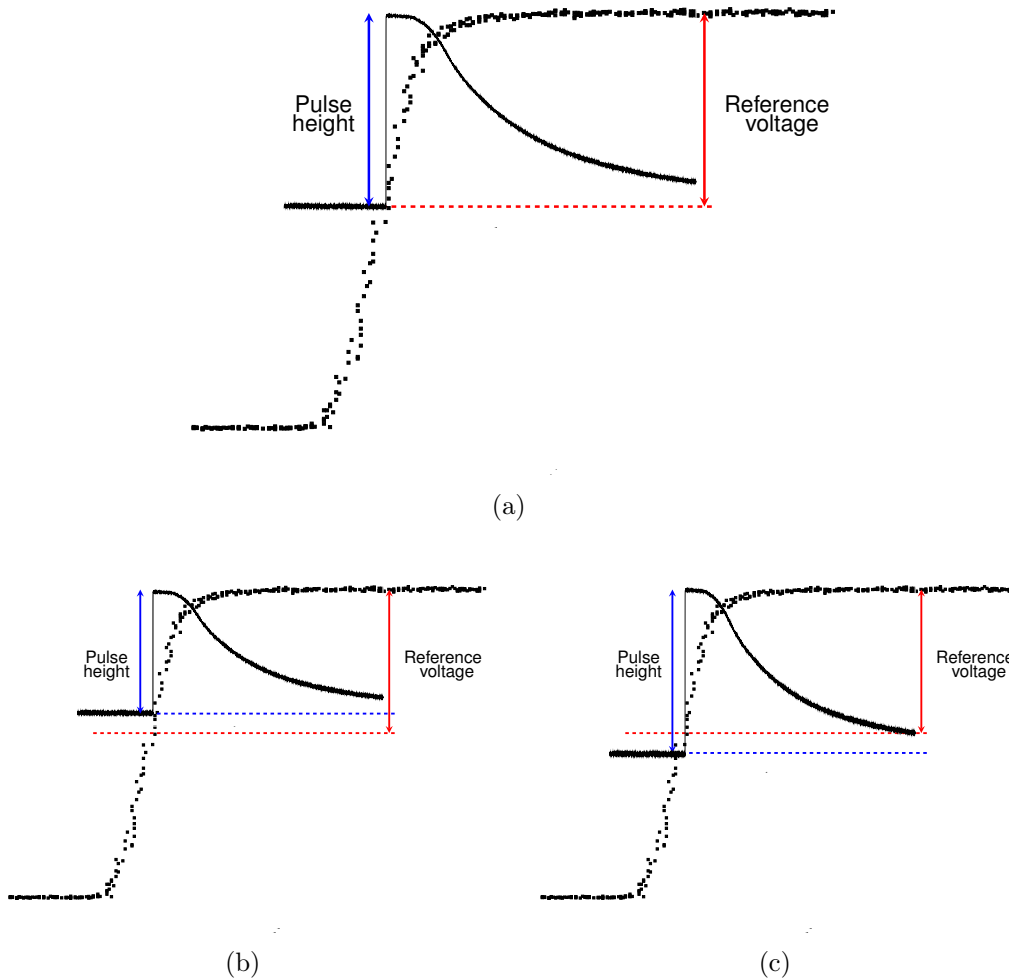


Figure 3.11: In the figure is shown in a naive way how the pulse height of a saturated control pulse is used to determine the working point. In (a), the detector is in the correct working point, and the pulse height is equal to the reference. Instead, if the detector is below or above the working point, the control pulse height will be higher or lower than the reference voltage, as shown in (b) and (c). In this way, it is possible to identify unstable data taking period.

3.3 CRESST most recent results

Thanks to the cryogenic calorimeter technique and the low energy threshold of ~ 300 eV achieved, CRESST has been able to push for the first time the search for Dark Matter sensitivity down to a mass of $500 \text{ MeV}/c^2$ [96], see the solid red line in Figure 3.14.

To extend the probed region of the cross-section - mass plane, there are two different ways. The key factor in pushing the sensitivity toward lower cross-section is the exposure, while to move to lower mass, the crucial point is to lower the threshold.

From 2016 CRESST has focused its scientific program on light Dark Matter search ($0.1 \div 10 \text{ GeV}/c^2$ range). Major upgrades in both the hardware and software to lower the energy threshold and push the search for Dark Matter to lower

mass was performed.

Concerning the hardware, CRESST passed from crystals of around ~ 300 g of 2016 to the actual crystals of ~ 30 g. In this way, the crystal thermal capacity is reduced, improving the detector energy resolution and lowering the threshold. The drawback is the energy reduction as, with a smaller crystal mass, the TES saturates with a smaller energy deposition.

On the software side, the use of a continuous data acquisition system allowed the development of a software trigger [97] based on the optimum filter technique by Gatti and Manfredi [98]. Thanks to these efforts, CRESST reached a threshold of ~ 30 eV setting a new standard for low mass dark matter search.

The results obtained with such upgrade are shown in Figure 3.12 [64]. The result of the CRESST upgrades can be fully appreciated in the plot, with an exclusion limit reaching a Dark Matter mass of $160 \text{ MeV}/c^2$.

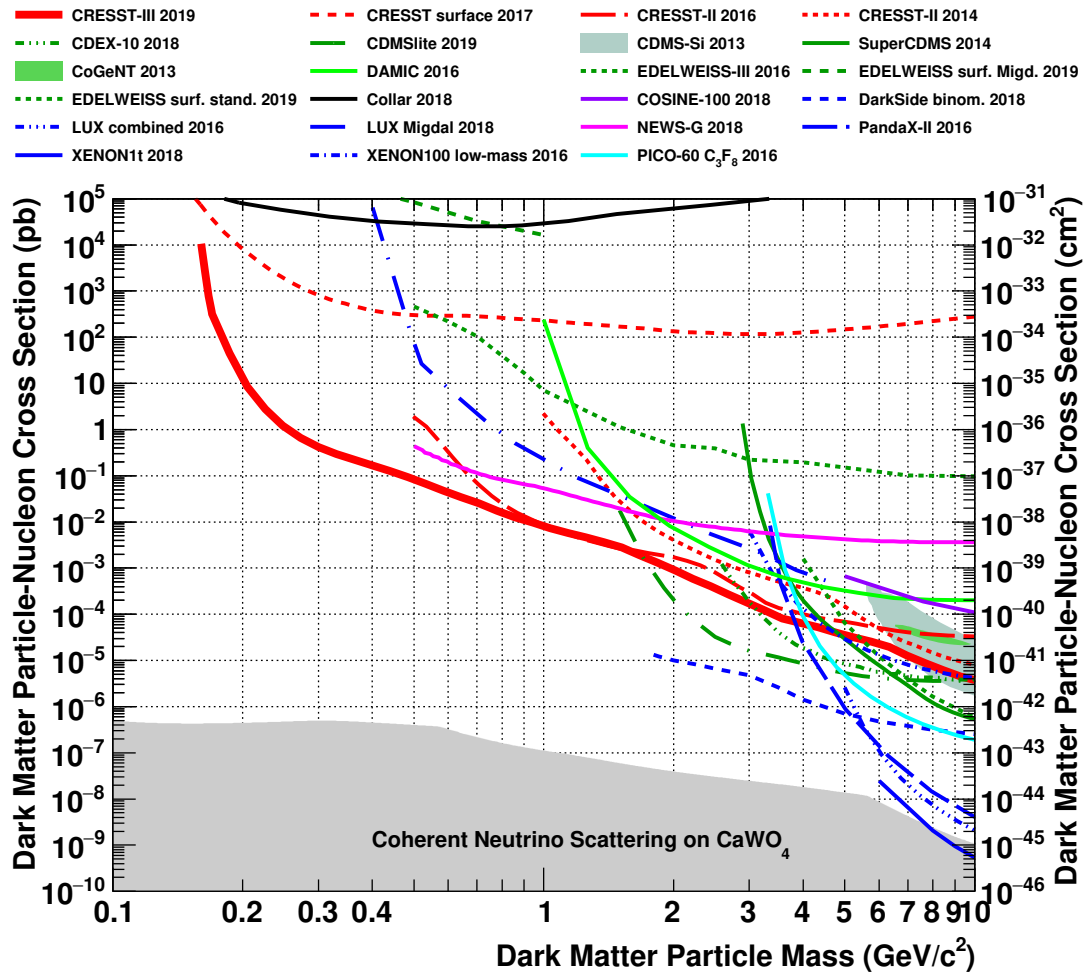


Figure 3.12: Most recent CRESST results (red solid line) compared with exclusion limits obtained other experiments [64].

Before the substantial background reduction allowed to achieve the results shown in Figure 3.12, in 2012, CRESST published the results of Run 32 shown

in Figure 3.13. The two islands present in this figure are due to a 4σ event excess in the acceptance region unexplained in terms of any known background sources.

More precisely, the blue island corresponds to the region of the Cross Section - Mass plane compatible at 68% C.L. with a Dark Matter mass of $25.3 \text{ GeV}/c^2$. Similarly, the two azure islands are the regions compatible at 90% C.L. with a Dark Matter mass of $11.6 \text{ GeV}/c^2$ and $25.3 \text{ GeV}/c^2$ for the M2 and M1 points respectively [99].

As shown in Figure 3.14, these two islands were partially excluded using data from two single modules collected during Run 33 data-taking [100, 101]. The main goal of this work is to test the two *islands* of Figure 3.14 analyzing and combining data from multiple detectors collected during Run33 using a Likelihood approach.

The long data taking period of approximately two years (July 2013 - August 2015), together with the larger mass of the used crystals, concur in obtaining a large exposure, which as aforementioned, is a crucial point to lower the previous limit and completely rule out the islands.

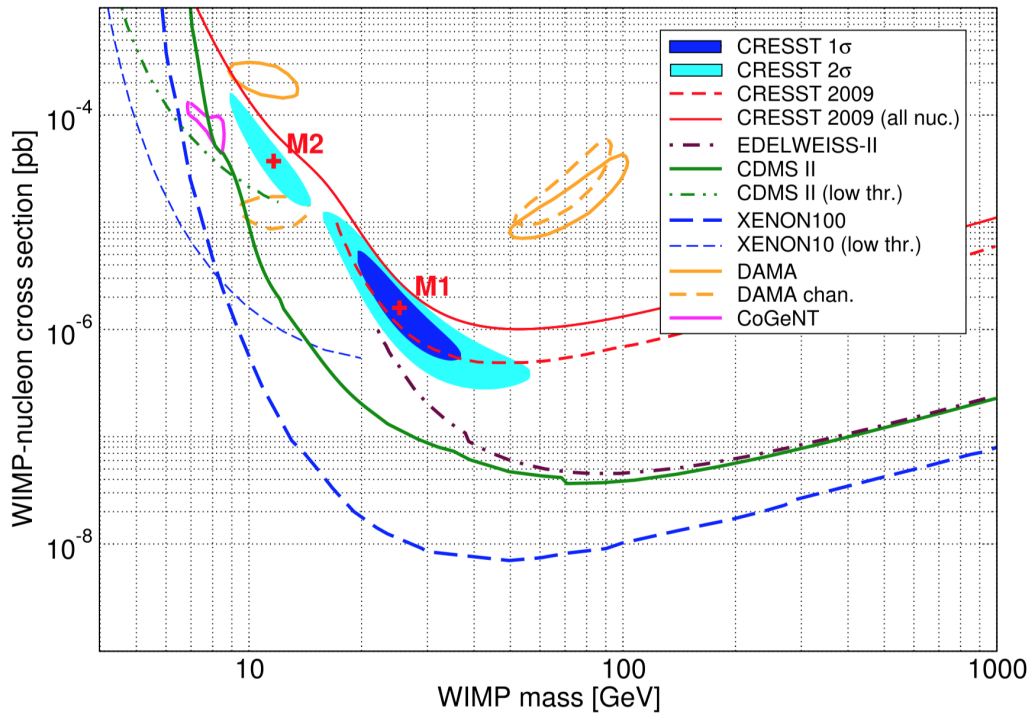


Figure 3.13: Figure shows the two 2σ confidence region labeled M1 and M2, due to the excess found during the Run32 [99]

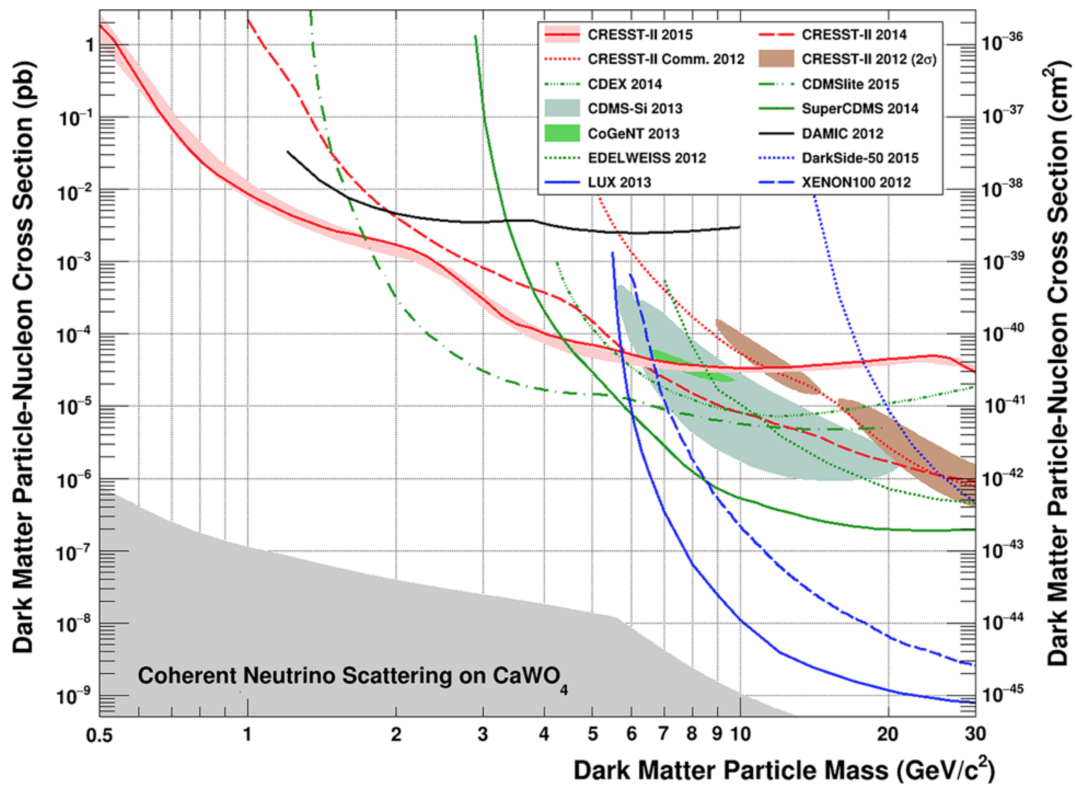
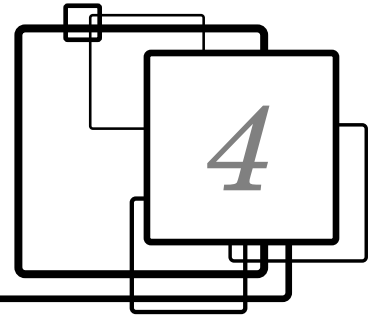


Figure 3.14: From the Figure it is possible to see how the two *island* obtained with the previous Run 32 data. Exclusion limit obtained with CRESST Run33 data [101].



CRESST data analysis

In this Chapter, the steps of the standard CRESST analysis workflow are described. The analysis The readout chain, the fit, and energy calibration procedure are illustrated. The crucial aspect of this approach is the reconstruction of the pulse amplitude, particularly for pulses exceeding the linear range of the transition. After the low-level analysis process necessary steps, the various selections that lead to the final accepted events are described in detail. The cut efficiency curve is then evaluated using simulated data, while energy resolution and threshold are obtained with dedicated measurements. Finally, the Light Yield-Energy plane and the energy spectrum are presented for the selected events. The analysis illustrated in the following Chapter is the core of my work. The described methods have been used to study data acquired by 12 CRESST modules during Run33.

4.1 Data acquisition

As explained in 3.2.2, the temperature rise inside the crystal is converted in a voltage using SQUID sensors.

The output of the SQUID is split in two. One signal goes to a 16 bits transient digitizer, which writes the signal continuously on a ring-buffer at 25 kHz within the range $-10V \div 10V$. The second signal is filtered, amplified, shaped, and sent to the trigger. Each transient digitizer is enclosed with the other seven digitizers in a trigger module.

If one detector channel (phonon or light) trigger fires. The signal opens the time window acquisition. After the time window closes, the detector data are recorded on the disk. The written event includes a pre-trigger time of ~ 80 ms and a post-trigger time of ~ 245 ms.

After the first trigger, the trigger remains active for ~ 120 ms to receive signals from other digitizers in the module and then is inhibited for ~ 200 ms. In Fig 4.1, the relevant time intervals for the pulse recording are shown graphically and numerically.

In addition to the triggered pulses, also signals artificially triggered by the DAQ, called Empty Baseline, are written to disk. This kind of signal will be used to simulate pulses of different energy and measure the cuts efficiency.

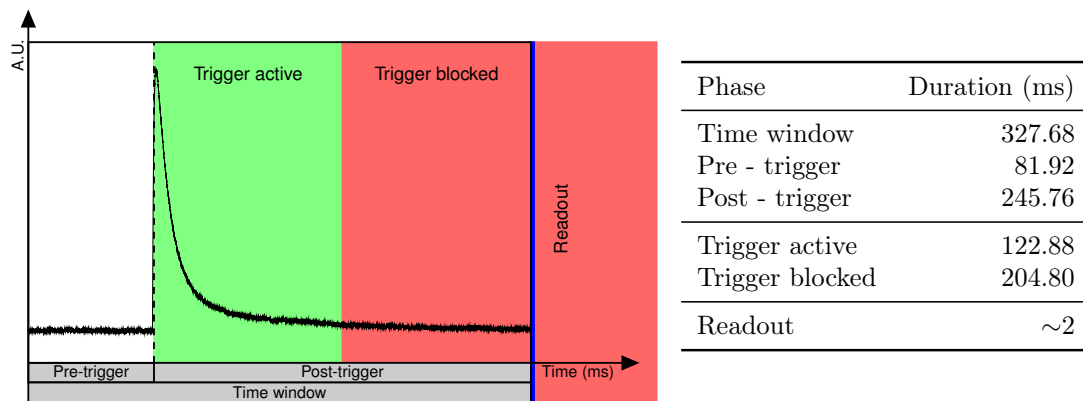


Figure 4.1: The figure on the left shows how data are recorded, when a trigger occurs. In red and green are highlighted the periods when the trigger is active and blocked, blue depicts data writing on disk. The post trigger time is awaited before writing the data on disk. The table on the right reports the exact duration of the most significant parameters.

4.1.1 CRESST datasets

The CRESST analysis uses three different class of datasets, each one used for a different purpose.

Gamma Calibration dataset obtained placing a ^{57}Co gamma source near the experimental area, inside the lead and copper shields. The data collected during this phase are used for:

- extend the linear range of the TES
- linearize and calibrate in energy the Test Pulses

Neutron Calibration dataset obtained placing an AmBe source near the experimental area, inside the outer polyethylene shielding. The data from the neutron campaign calibration are used for :

- the validation of the cuts applied to the data, to verify that the cuts do not remove events in the nuclear recoil bands.
- modeling the nuclear recoil band needed for the exclusion limit, see Chapter 6

Physics data this is the dataset used for the Dark Matter analysis. The physics data are collected in stable conditions and without any source nearby the experimental area.

All three datasets have been analysed using *CresstTools*, a ROOT-based[102] framework developed by the CRESST Collaboration. As part of my work, I personally wrote part of the routines and macros used in this analysis.

4.2 Pulse Fit and Energy calibration

The first part of the analysis workflow is devoted to studying the calibration campaign data obtained with a ^{57}Co gamma source.

4.2.1 TES range extension

The TES extension range is the procedure to extend the TES linear range over the TES plateau. The main purpose of the procedure is to analyze pulses, which put the TES out of transition. The range extension is done through the pulse fit. A detailed description of the procedure to fit the pulse and to extend the TES linear range will be presented.

Despite knowing a valid model for the pulse formation inside a CaWO_4 crystals, to avoid any form of bias from the model, a pulse template is created directly from particle-induced events and used for the fit.

The template is built summing many good pulses around the same energy coming from the TES linear region (this can be only verified *a posteriori*). Figure 4.2 is showing the distribution of the pulse height of events for gamma calibration data and the Test Pulses population. The 122 keV and 137 keV peaks of the ^{57}Co are clearly visible.

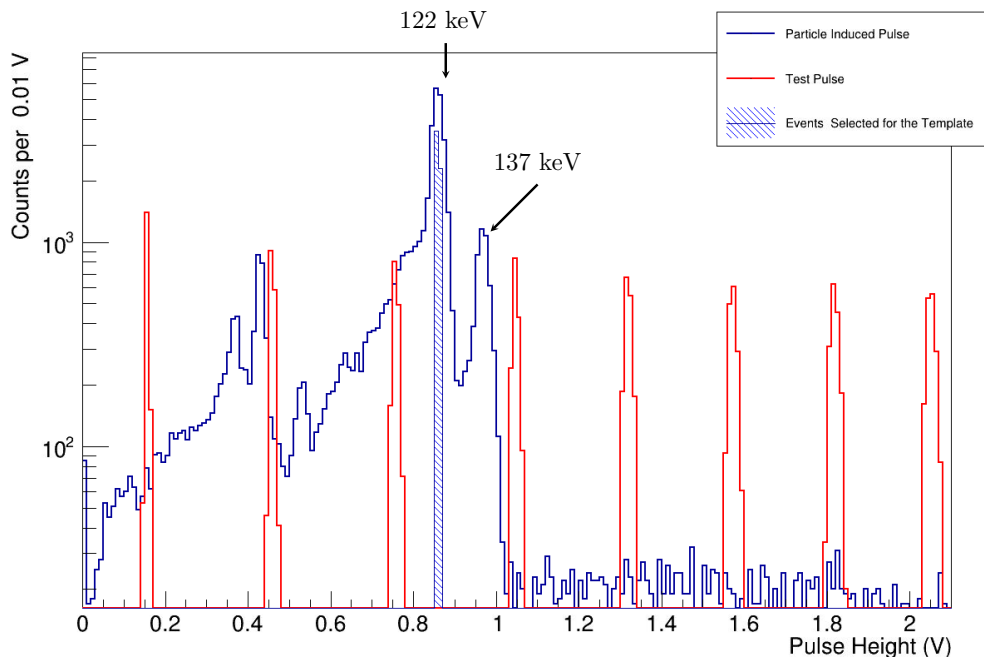


Figure 4.2: The blue curve represents the distribution of the raw pulse height relative to the phonon channel for one module. It is possible to clearly see the 122 keV and 137 keV peaks from ^{57}Co . Also, the presence of tungsten in the crystal produces three additional peaks. The gammas from cobalt can extract an electron from tungsten via the photoelectric effect. If the interaction happens close to the target surface, the X-rays from K_α and K_β tungsten escape lines could not be detected. Then for each calibration line at energy, E_γ other peaks at energy $E_\gamma - E_{esc}$ are expected. In red the Test Pulse population used for linearization.

The events from the 122 keV peak after a few simple cuts to clean the sample from pile-up and electronic noise are used to create the template for both the phonon and light channels, as shown in Fig. 4.3. Concerning the Test Pulses, instead, the template is created using the Test Pulse peak closest to the 122 keV peak.

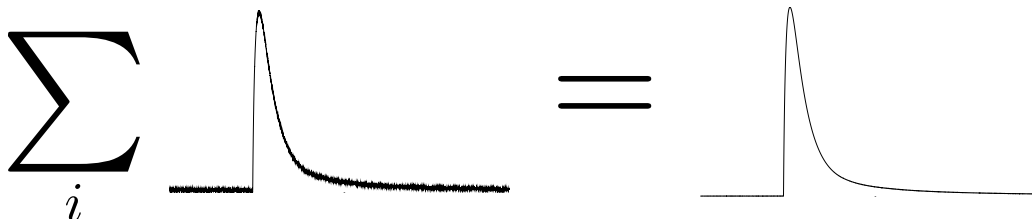


Figure 4.3: The sum of many particle pulses in the same energy range makes it possible to create a template cleaned by the electronic noise and usable for the fit. The sum is done aligning all the baseline to 0. The resulting template is then normalized to a pulse height of 1V. In this way, during the fit procedure, the scaling factor of the template will represent the measure of the pulse height.

After the template creation, the fit can be performed. The fit procedure scales and shifts the template to match the pulse and adjust the parameter of the third polynomial used to describe the baseline (Fig. 4.4). The use of third-degree polynomial to model the baseline is justified by the better energy resolution achieved [103].

From the fit procedure, it is then possible to find three main variables:

Amplitude : precise measure of the pulse height, obtained scaling the template model;

Time shift : time shift relative to the trigger, aligning the template with the pulse, a better time evaluation of the event is obtained;

RMS : the Root Mean Square of the fit, is the root of the sum of the squared residuals and measure of the goodness of the fit. The RMS square multiplied by the number of fitted points is equivalent to the χ^2 .

After a first fit of the events, it is possible to plot RMS vs Amplitude of the data and have a closer look at the RSM with an amplitude below 2V, as shown in Figure 4.5. In the plot, it is possible to observe the RMS rise at a value around 1V, when the pulse approaches the end of the superconductive transition and moves away from linearity. Looking at the plot, it is possible to set a Truncation Limit voltage to fit only the pulse linear part.

Comparing Fig. 4.5(b) and Fig. 4.2 it is possible to see how the amplitude of the 122 keV peak of ^{57}Co is around 0.85V, which is below the truncation limit

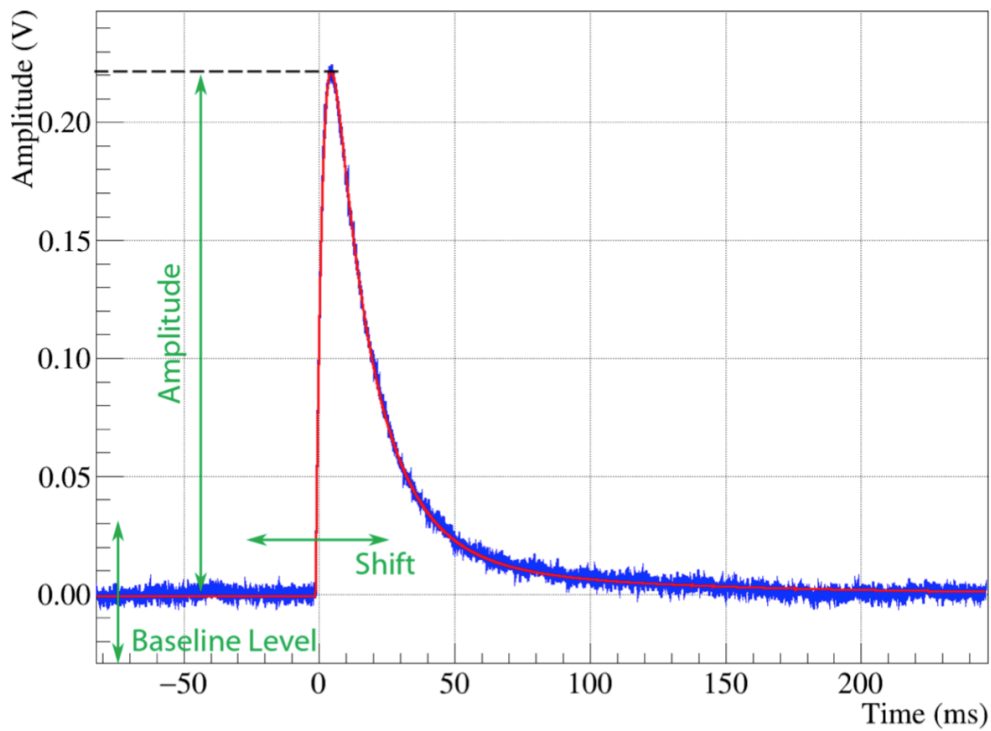


Figure 4.4: In the figure is possible to see the 3 main parameters adjusted by the standard fit procedure.

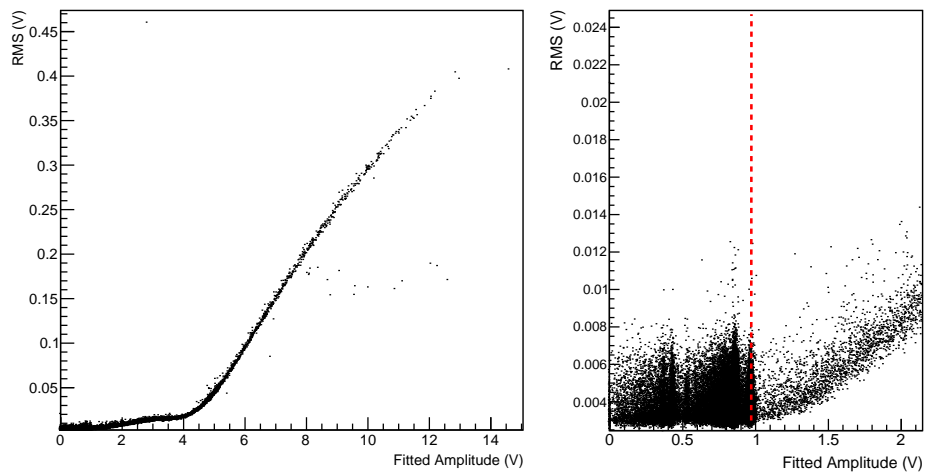


Figure 4.5: On the left is shown the RMS vs Amplitude for the main population. On the right is shown a zoom of the amplitude below 3V, is possible to see the rise of the RMS around 1.1V, in this way is possible to set the truncation limit of 0.98V identified by the red dashed line.

of 0.98V for the module took under examination. Therefore we can confirm that the template is created from a linear response region and can be used for the

truncated fit.

In the case of pulses larger than the truncation limit, only a subset of the points are used for the template fit, as shown in Fig. 4.6.

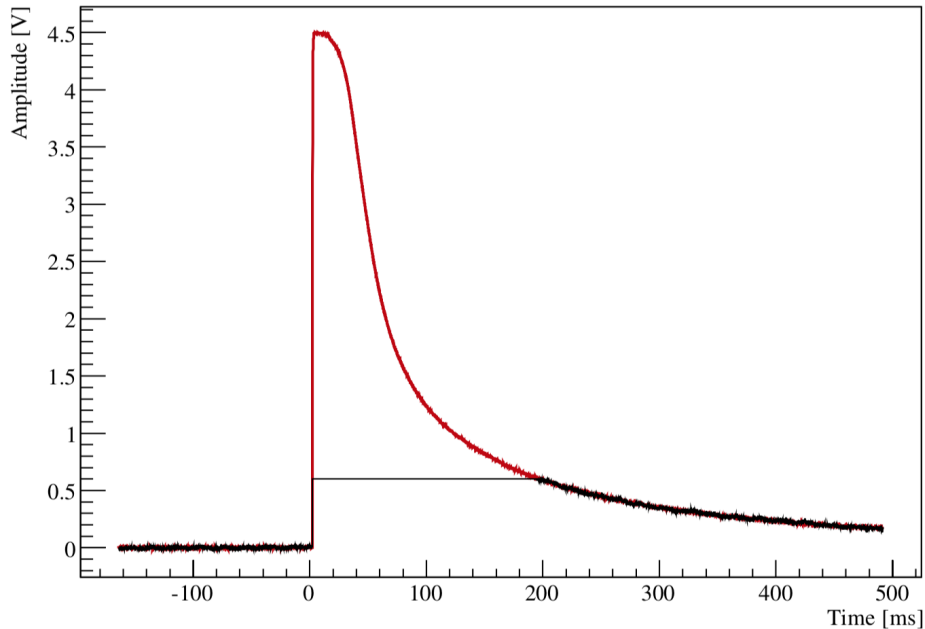


Figure 4.6: In figure is shown the principle of the truncated fit, the pulse points are in red, instead in black instead there are only the point used for the fit.

Despite not using all the points collected, the truncated fit procedure extends the TES linear region. This method has some intrinsic problems.

- for very large energy released in the crystal, most or all the points of the tail of the pulse will be above the truncation limit, and the fit is based mainly on the pulse rise. This effect makes the amplitude measurement of very large pulses not reliable;
- the pulse shape changes with the energy; hence this effect cannot be taken into account using a single template fit for all the energies. This effect leads to a non-linearity behaviour at high energies, which can be correct using the Test Pulses.

4.2.2 Linearization and Energy Calibration

We use Test Pulses to extend and linearize the pulse response and convert the amplitude in energy. As anticipated in Section 3.2.3, the Test Pulses are used to monitor the detector response. Fig. 4.7 shows the use of splines to connect Test Pulses of the same injected voltage. Thus, it is possible to monitor the detector

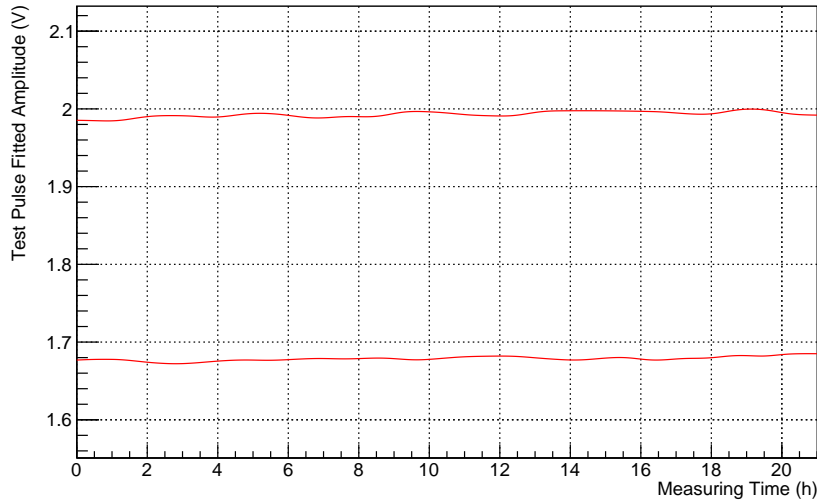


Figure 4.7: The figure shows temporal splines for a data set. Such splines are obtained from the fit of the Test Pulse sent during the data taking.

behaviour during all the data taking and correct working point changes due to small temperature variations.

The transfer function is then defined on an event by event basis according to the value of the Test Pulses temporal spline at the time of each particle event. Fig. 4.8 shows how for a given time, t_0 the transfer function is built using the value of the temporal spline at t_0 and the voltage of the injected Test Pulse. Since the fitted pulse height is converted in the injected test pulse amplitude, this new variable is called Equivalent Test Pulse Amplitude (EquivalentTPA). Since the EquivalentTPA scale is linear by definition, it can be converted in energy using the Convert Pulse to Energy (CPE) factor found using the γ line of the ^{57}Co source, as shown in Figure 4.8.

The same procedure illustrated above to linearize and convert in energy the phonon channel is also applied to the light channel. As explained in Section 3.2, only a small percentage of energy goes in light, and the amount of light produced is energy-dependent. The CPE factor for the light channel assigns to the light produced by the 122 keV gamma of ^{57}Co the same energy; with such procedure, the value of the LY for gamma and electron events is normalized to 1 at 122 keV.

The use of the method mentioned above allows us to obtain a better energy resolution, as shown in Figure 4.9, where the energy obtained multiplying the EquivalentTPA for the CPE and the fitted amplitude for the Amplitude to Energy factor (A2E) are superimposed. This effect is particularly visible by looking at the 122 keV and 137 keV peaks, which are narrower and higher.

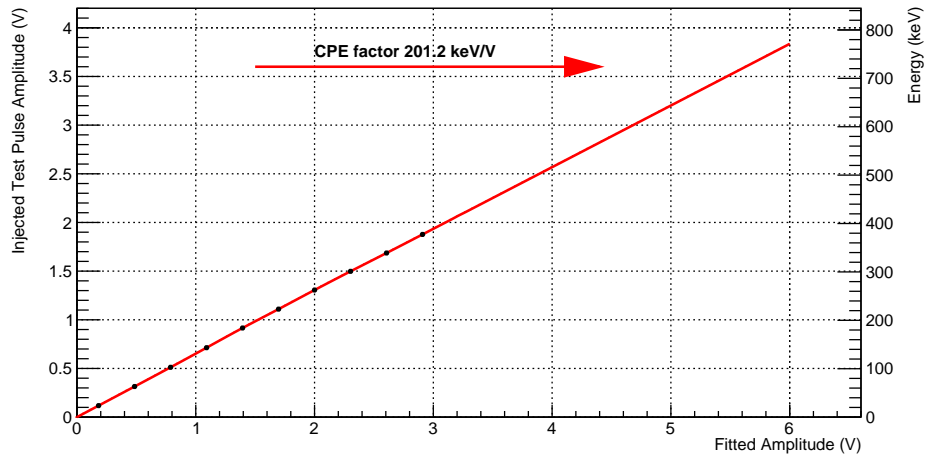


Figure 4.8: Test Pulse Amplitude injected voltage vs Fitted Amplitude. The x value of the black dots is the Test Pulses computed value with the splines at the time t_0 , while the y value is the injected voltage. It is then possible to build a transfer function to convert the fitted amplitude of the pulse to Injected voltage. The EquivalentTPA scale can be then converted easily in energy using the CPE factor.

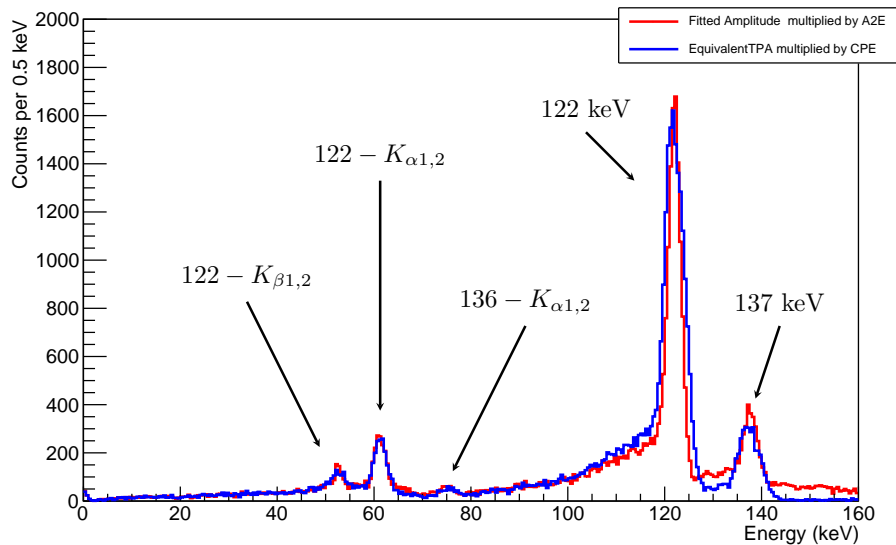


Figure 4.9: The same spectrum for different energy variables for the phonon channel. The blue line represents the Fitted amplitude multiplied the A2E factor, while in red is depicted the EquivalentTPA multiplied for the CPE factor. It is possible to notice how all the visible peaks became narrower. This comparison makes sense since we are in the linear range of the TES and the fitted amplitude can be converted in energy just multiplying it by the A2E factor.

4.3 Stability, coincidence, and data quality cuts

After the light and phonon channels energy calibration, the data needs to be cleaned to remove all the bad events and have a Light Yield vs Energy plot

useful for the exclusion limits. We define bad events that triggered signals with a pile-up, late or early pulse, SQUID reset, decaying baselines, and electronic noise.

4.3.1 Blind analysis

In CRESST, the analysis is blind to avoid any possible data-driven cuts. For this reason, all the cuts (except for the Stable and Rate Cut) are defined on the so-called Training Set, a subset composed of a 20% of files randomly select from the full data set. After all the cuts are defined, they are applied to the full dataset.

4.3.2 Stability Cuts

There are two types of stability cuts needed to remove bad times period in the data taking: the Stable Cut and the Stable Rate Cut.

4.3.2.1 Stable Cut

The Stable Cut accounts for the periods where the detectors were out of the correct operating point. As said in Section 3.2.3, the detector operating point is monitored using the Control Pulses. The pulse height of the control pulse is saved on a different file. Figure 4.10 shows the distribution of control pulse height for a module with a reference value of 5.583V.

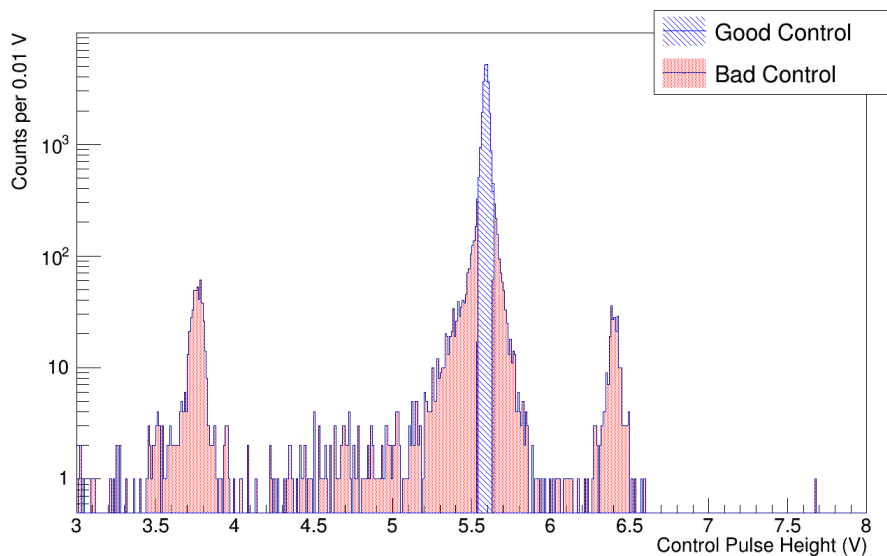


Figure 4.10: The figure shows the distribution of the measured height of the control pulses. With a gaussian fit is possible to find the mean (μ) and the width (σ) of the peak, used to tag the unstable period.

After performing a Gaussian fit of the control pulses peak, it is possible to tag Control Pulses distant more than 3σ as *bad control*. All the periods between two *good control* are flagged as stable. The periods between two bad control or between a good and bad control are tagged as unstable, and every signal in these unstable time window is removed.

4.3.2.2 Rate Cut

The Rate Cut is the only cut done directly on the full dataset. The cut is placed after monitoring the distribution of the event rate as a function of time. All the events belonging to a 10 minutes time interval where the number of counts exceeds a chosen threshold are removed from the analysis (see Figure 4.11). Since the local rate variation with time does not contain any dark matter information, the concept of blind analysis is still valid.

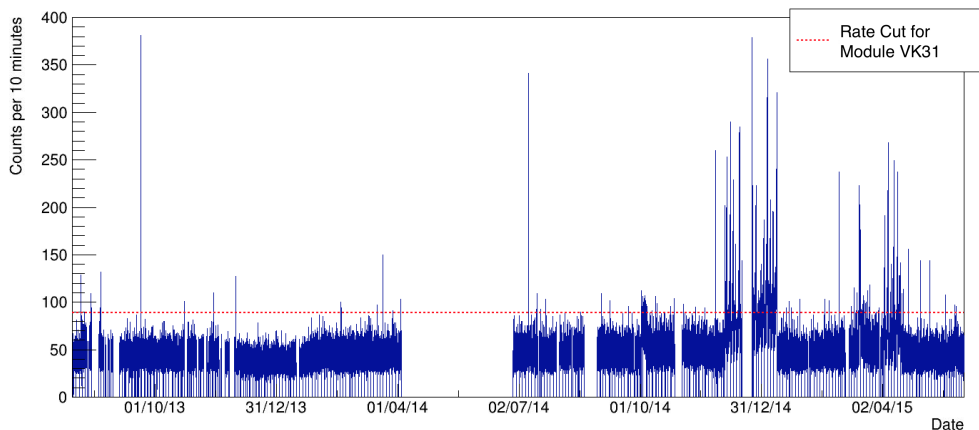


Figure 4.11: The figure shows the rate count for the Module VK31 during all the data taking; the cut is placed at rate of 89 counts per 10 minute. The threshold value correspond to a rate value of 3σ above the mean value. Time intervals with zero counts correspond to detector maintenance, during which the acquisition is stopped.

This cut removes periods with unusually high rates due to environmental or electronic noise.

4.3.3 Coincidence Cuts

While the rate and stability cuts are done on the raw data, the coincidence cuts are done using the precise time measure obtained by fitting the pulses with the template.

4.3.3.1 Muon Coincidence Cut

The Muon Coincidence cut removes events coincidentally with a signal in the muon panel surrounding the lead shielding. Most of the muon panel signals are

due to the surrounding materials gamma radioactivity, so most muon panel triggers are due to events that have no chance to reach the detectors. For this reason, the coincidence window is kept very narrow to avoid strong event suppression. Since the time resolution of the muon trigger is more than ten times better than the one of the detectors, the only parameter this cut is based on is the time resolution of the trigger obtained with the pulse fit. Based on this, all events within $\pm 2\text{ms}$ from a muon trigger in the panel. This time interval corresponds to $\pm 3\sigma$ in the time shift resolution [103].

4.3.3.2 CryoCoincidence Cut

The CryoCoincidence cut removes events in coincidence with signals in the other detectors. This cut is particularly relevant to reject multi-detector hits due to neutrons.

As said in Section 3.1.2, neutrons are one of the most dangerous backgrounds since they can mimic a nuclear recoil induced by a dark matter particle. However, contrary to Dark Matter interactions, neutrons are likely to do multiple scattering in the detectors. In this case, the time window used to remove coincident signal is larger than the one used for the muon coincidences since the time shift resolution play a role for both the detector in coincidence, so are removed events in coincidence in the $\pm 5\text{ms}$ time window.

4.3.4 Data Quality Cuts

The data quality cuts are needed to remove all events due to electronic artifacts, trigger artifacts, and pile-up. Since they do not have a good pulse shape, most of these signals have a high RMS and can be removed using a cut on this variable. To do a narrow cut on the RMS variable, cuts on BaseLine, Peak Position, are performed before this one.

4.3.4.1 BaseLine Difference Cut

The BaseLine Difference variable measures the voltage difference between the left and right parts of the pulse. Such a variable is built using the average of the first 50 points minus the average of the last 50 points. This cut is useful to remove events featuring a decaying baseline or pile-up. Besides, this cut removes events characterized by a huge energy deposit in the crystal, where the feedback mechanism does not react fast enough, and the SQUID changes its working point. These events are called Quantum Flux Loss events. An example is reported in Figure 4.13(c). Event where the baseline reaches the ADC lower limit range of -10V cause an ADC reset and a 10V baseline jumps, Figure 4.13(d).

4.3.4.2 Delta Spike Cut

This cut removes delta spike events, similar to the one reported in Figure 4.13(a) with an instantaneous change of the signal, and cannot be due to any physical event but are induced by electric noise. These events can be identified by looking at how much the pulse changes compared to the typical baseline oscillation. The parameter used to discriminate this topology of events is the ratio between the pulse minimum derivative and the BaseLine RMS.

4.3.4.3 Peak Position Cut

The Peak Position is the maximum of the pulse, usually a few milliseconds after one-fourth of the time window. A cut on this variable removes all those events where the pulse is outside the pulse fit nominal region. Events where the rise anticipates the trigger are due to particle interaction happening in the detector when the trigger is blocked. If the pulse is still above threshold when the trigger is re-activated, the trigger fires again, and the anticipated pulse is written on disk. Events, where the pulse is in the last part of the time window, are likely triggers due to noise followed by another event a few moments later.

This cut is not applied on the Light channel since possible Dark Matter events will release a small amount or no light at all. When the peak is not distinguishable by the baseline noise, the peak position is randomly found on the baseline electronic noise. A cut on this variable for the light channel could remove possible interesting physics signals.

4.3.5 RMS Cut

After the previous cuts are applied, it is possible to apply the RMS cut more simply. Figure 4.12 shows how the RMS vs Amplitude plot changes after all the cut defined above are applied. In this way, a narrower cut on the RMS variable can be defined, eliminating events with RMS value too large compared to the main population.

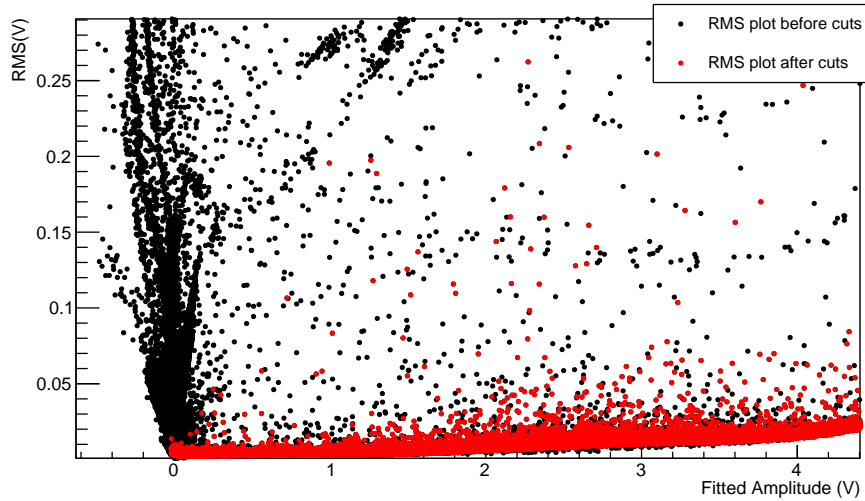


Figure 4.12: The figure shows RMS vs Amplitude plot for the phonon channel of VK31, before (black dots) and after (red dots) the quality cuts are applied.

4.3.6 Carrier Cut

For some detectors like TUM29 (Figure 4.14(a)), the TES is not evaporated directly on the absorber crystal. The TES is instead evaporated on a carrier crystal. In other detectors, like TUM40 (Figure 4.14(b)), the crystal is held by sticks made of CaWO_4 .

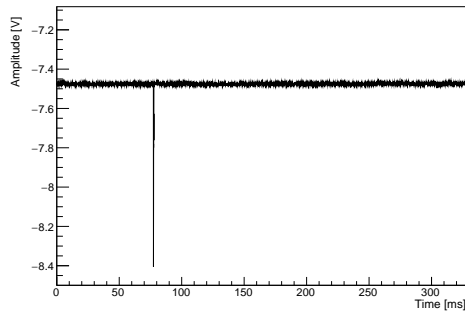
Energy deposition in the carrier or the stick leads to particle pulse with a faster rise and decay times. These kinds of events are the most difficult ones to remove with the previously described data quality cuts since their RMS is not large enough compared to the template pulse one. Figure 4.15(b) shows a carrier event fitted with the absorber template.

To get rid of the carrier event, a new fit of the pulses from this module is performed for all the detectors with carrier or stick. For this fit, a new specific template is created using carrier events (Figure 4.15(a)), and a new variable is defined as the normalized difference of the RMS obtained by each event fit with both absorber and carrier templates.

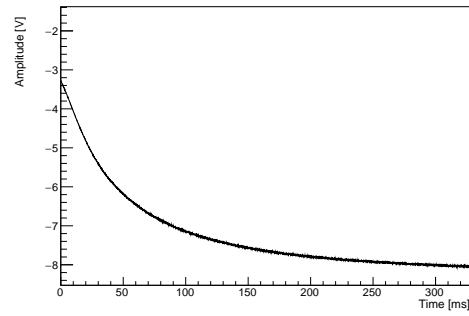
$$\text{RMS}_{ratio} = \frac{\text{RMS}_a - \text{RMS}_c}{\text{RMS}_a + \text{RMS}_c} \quad (4.1)$$

In equation 4.1 a denotes the RMS of the fit done with the standard absorber template, while c denotes the RMS of the fit done with the carrier template. Particle events in the absorber will have an RMS_a value lower compared to the RMS_c value. Since the goodness of the fit is better, the value of RMS_{ratio} is negative, for carrier event is the other way around, and the RMS_{ratio} has a positive value.

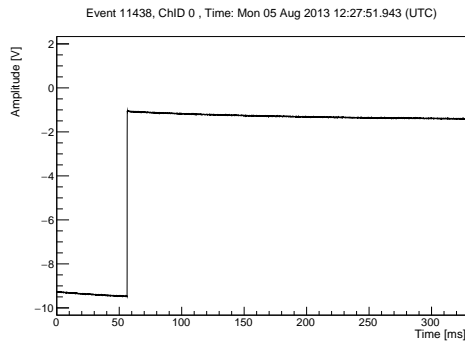
The plot in Figure 4.16 shows the separation between carrier and absorber event using the RMS_{ratio} for Module TUM29.



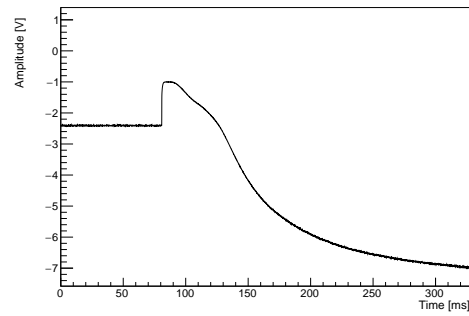
(a) Delta Spike



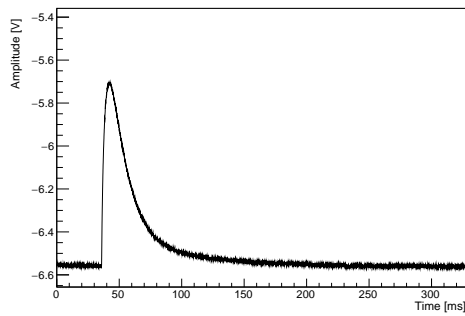
(b) Decaying baseline



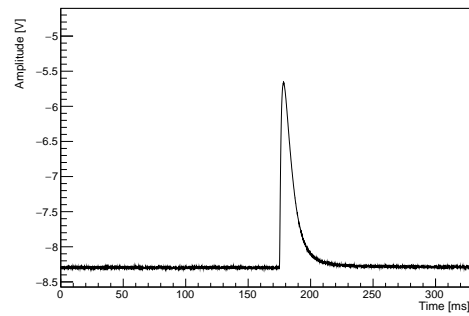
(c) ADC reset



(d) Quantum flux loss



(e) Pre-trigger Pulse



(f) Post-trigger Pulse

Figure 4.13: Figure shows events like the spikes removed with the MinDerivative over BaselineRMS ratio, the Quantum Flux Loss and ADC reset are cut away from the BaseLine Cut, and the outside from nominal position Pulse discarded with the Peak Position cut.

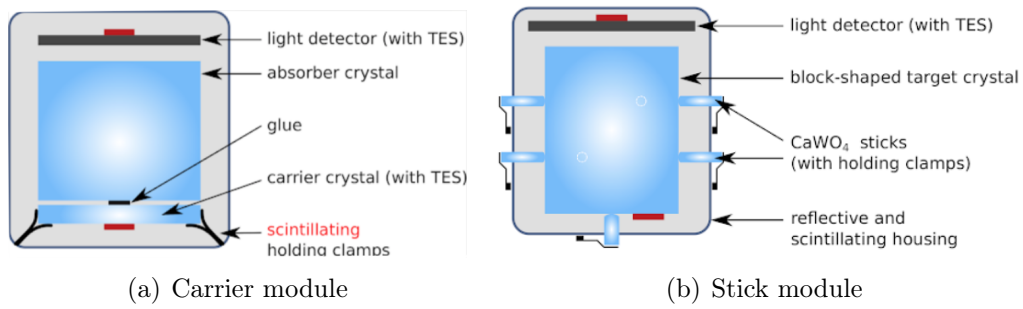
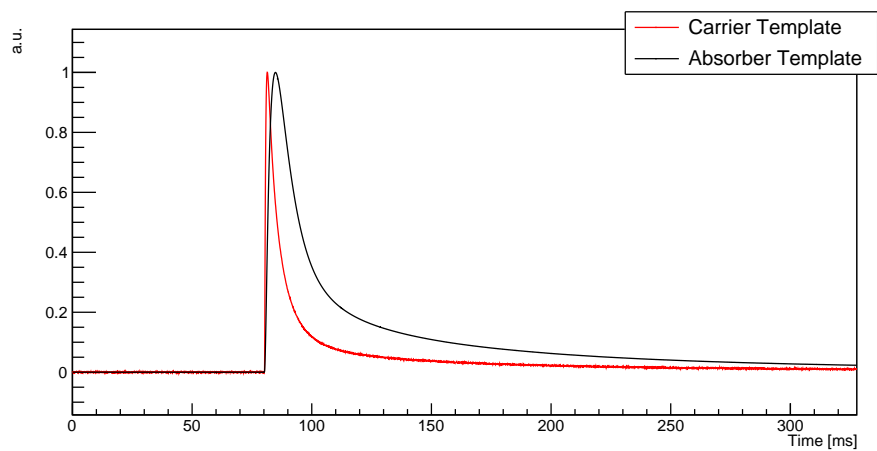
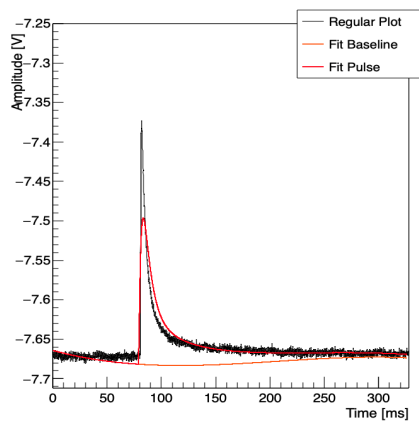


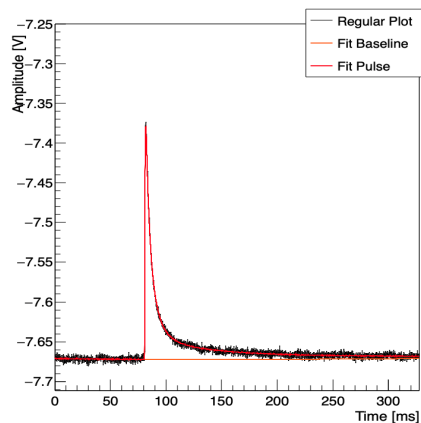
Figure 4.14: The figure shows the two types of modules interested by the Carrier Cut. (a) shows the TUM29 module design with a carrier; (b) shows the TUM40 design with the CaWO_4 sticks.



(a)



(b)



(c)

Figure 4.15: In (a) it is shown the difference between the template created from absorber events (black) with respect to the one built using carrier events (red). In (b) and (c) it is possible to see the same carrier event fitted using an absorber and a carrier template respectively.

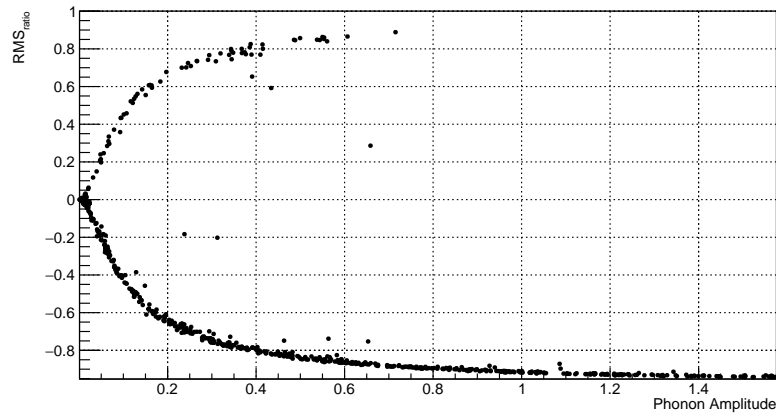


Figure 4.16: Figure shows RMS ratio vs Amplitude plot for the phonon channel of TUM29: the events that fit better using the carrier template populate the upper branch, while the ones due to energy deposit in the absorber populate the lower branch.

Since it is difficult to distinguish where the separation between the carrier and absorber events on the plot in Figure 4.16, the definition of a cut that removes most of the carrier events and at the same time does not reduce the absorber population is not trivial.

For this reason, the cut is defined on simulated events, where no carrier events are present (more details on how data simulation is done can be found Section 4.4.1). Figure 4.17 shows the distribution of the RMS_{ratio} variable for simulated data and the graphical cut used to remove the carrier events.

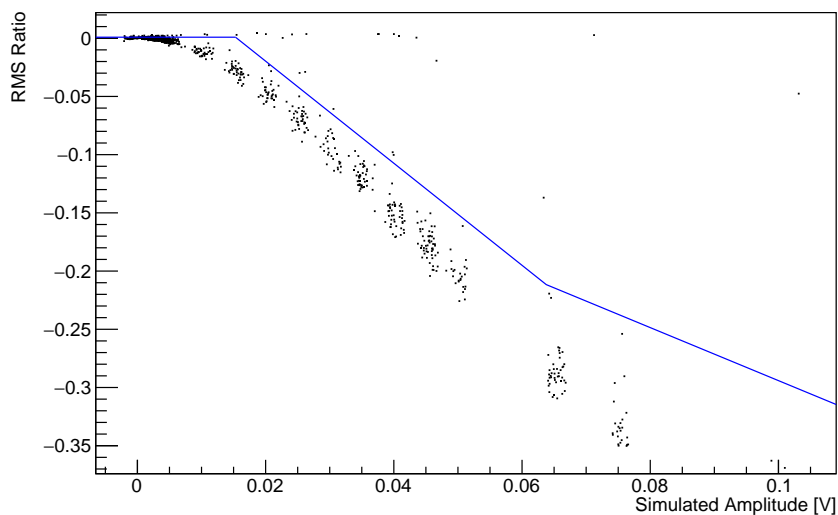


Figure 4.17: Figure shows the RMS_{ratio} versus the Simulated Amplitude. The RMS_{ratio} cuts has been defined on the simulated data where no carrier events are present.

4.4 Data Simulation and Cut Efficiency

4.4.1 Event Simulation

The Cut Efficiency determination is crucial to provide the right statistical weight to the events present in the nuclear recoil bands. To obtain the Cut Efficiency information simulated events are used. Such simulated events are created using the recorded events called Empty Baseline. Empty Baselines are events artificially triggered by the DAQ and not by the standard hardware trigger. These are mostly events with only the baseline noise and no pulse. Creating the simulated data using the empty baselines collected during data taking provide an extremely realistic simulation as pile-up effects and noise conditions are naturally included in the simulated data. The procedure adopted for the event simulation allows to properly evaluate the effects of the cuts on the acquired data.

The simulated energies are converted into pulse heights using the A2E factor described before. The pulse heights found are used to scale the template. To simulate tungsten nuclear recoils, the amplitude obtained for the light detector is multiplied by the tungsten quenching factor. In this way, the efficiency is calculated conservatively on the class of events producing the smallest light amount.

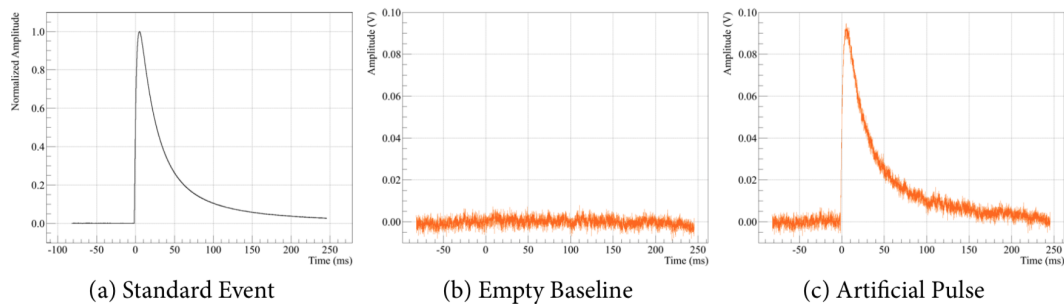


Figure 4.18: The same template used for the standard fit, after a scaling is summed to empty baseline to create an artificial pulse of the desired amplitude.

4.4.2 Cut Efficiency

After the simulation of different energy events, the standard analysis steps are applied to the simulated data. It is then possible to evaluate the effect of the different cuts on the data. The efficiency cut obtained for the training set can be different from the one from the full data set. This effect can be due to different noise and stability conditions, resulting in a different efficiency between the datasets.

In Figure 4.19, it is possible to note the effect of the various cuts on the TUM29 detector for the full dataset as a function of energy. All the cuts optimized on the real data are applied to the simulated one. As anticipated in the previous sections, the stable and coincidence cuts are energy independent. Instead, the data quality cut suffers from the detector finite energy resolution and the signal to noise ratio. So the survival probability is smaller at lower energy.

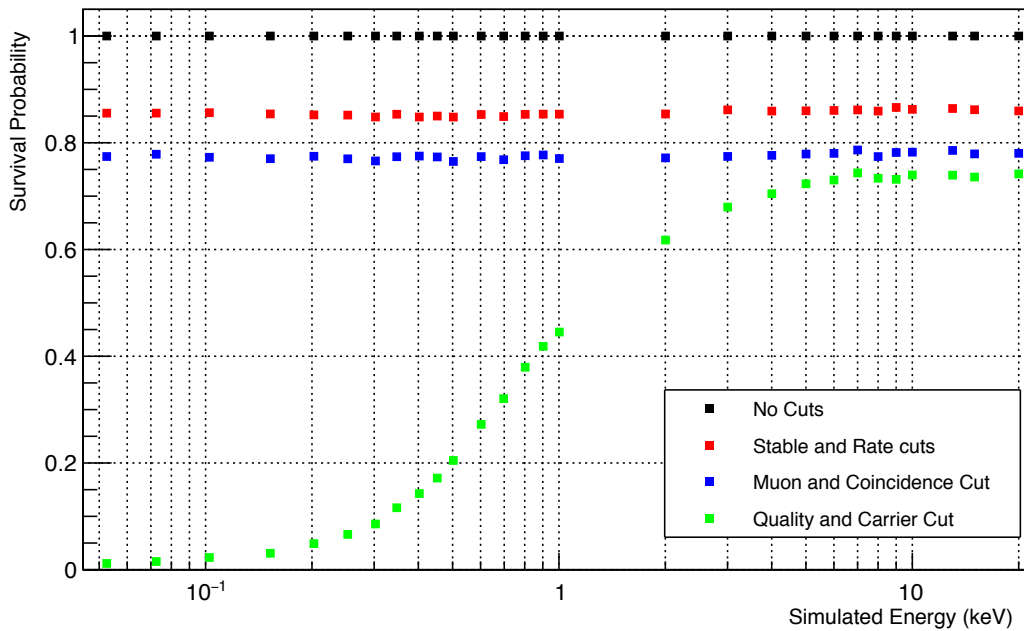


Figure 4.19: Figure shows the cumulative signal survival probability of the cuts applied on the full data set for the detector TUM29.

4.4.3 Resolution and Threshold

Two relevant parameters need to be measured since they play a crucial role in the band fit. These two parameters are the light and phonon channels energy resolution and the phonon detector energy threshold.

The energy resolutions are needed as input parameters to describe the resolution energy dependence of the two channels, which is essential to correctly define the band in the Light Yield vs Energy plane.

A precise measure of the trigger energy threshold is needed to determine the lower limit of the Region of Interest, which goes from the threshold up to 40 keV.

The energy resolution is computed, looking at the EquivalentTPA distribution of the smallest Test Pulse, fitted with a Gaussian function. Using the μ and the σ of the fitted Gaussian, the Test Pulse Injected voltage, and the channel specific CPE, the energy resolution is found with:

$$\sigma(\text{keV}) = \text{CPE} \cdot \text{TPA} \frac{\sigma(V_{inj})}{\mu(V_{inj})} \quad (4.2)$$

Figure 4.20 shows the distribution of the EquivalentTPA for TestPulse injected at 0.025 V in the phonon channel of detector Frederika together with the Gaussian fit. The parameters extracted from the gaussian, together with the CPE, are used to extract the phonon channel resolution.

For the energy threshold evaluation, a dedicated set of measurements has been done, sending different Test Pulses. The plot in Figure 4.21 shown the fraction of the Test Pulses, which have been triggered for given injection voltage.

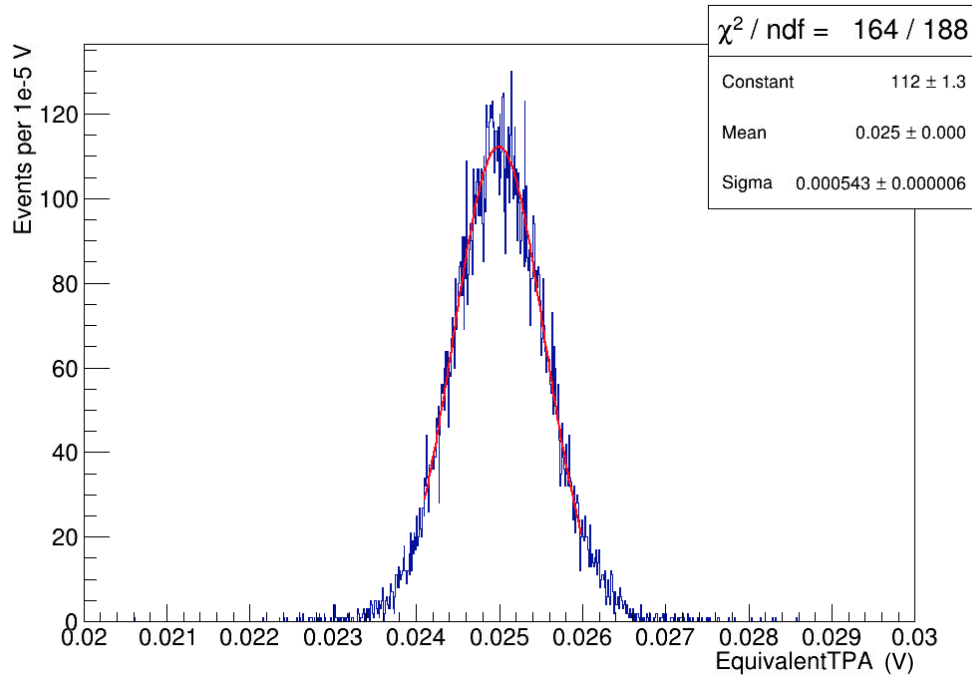


Figure 4.20: The Figure shown the EquivalentTPA distribution of the Test Pulse Amplitude injected a 0.025 V with the gaussian fit superimposed for detector Frederika, in the top right corner the relevant parameter of the fit are shown.

The data have been fitted with the function.

$$f(x) = \frac{1 - P}{2} \left[1 + \operatorname{erf} \left(\frac{x - \mu}{\sigma} \right) \right] + P \quad (4.3)$$

Where the P represents the probability of a random trigger when no Test Pulse has been sent, μ is the threshold in EquivalentTPA, and σ is the detector resolution in injected voltage at the threshold. The threshold in Equivalent TPA with the CPE factor gives the value of the threshold in keV.

4.5 Light Yield and Energy spectrum

There are two more energy corrections to implement, to obtain the most accurate energy reconstruction as possible, in the Light Yield vs Energy Plot.

4.5.1 CPE optimization

The first one concerns the adjustment of the energy scale to the lower energy. The CPE factor is initially calibrated on the 122 keV peak of the ^{57}Co . Since the CRESST interest is in the low energy region, this is adjusted using the low energy gamma peaks. The peaks come from the cosmogenic activation of ^{182}W

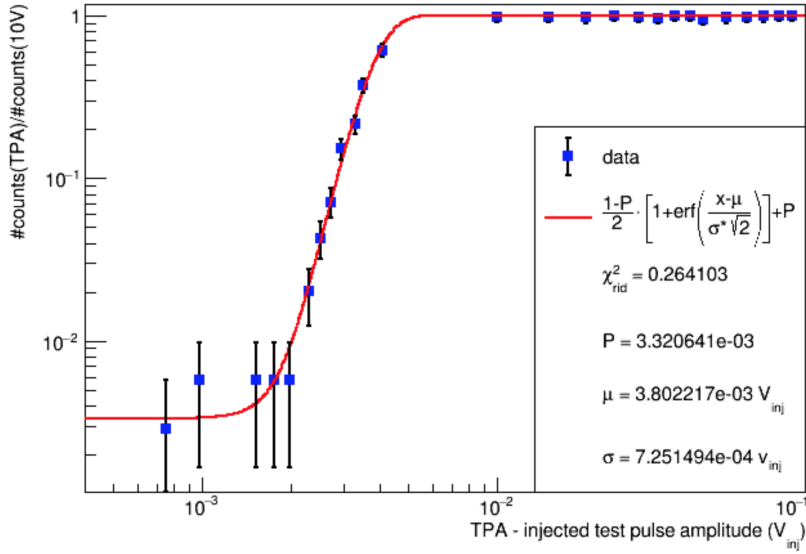


Figure 4.21: The plot shows the fraction of triggered events for detector Frederika.

isotopes present in the crystal. The cosmic protons produce tantalum via the interaction:



The tantalum decays with an half-time 1.82 years via electronic capture:



The electron capture produces a vacancy in the shell of the hafnium daughter nucleus. Such vacancy is filled by an electron from the external shells, which release a photon in the process. Gamma lines are coming from the K (63.5 keV), L1 (11.3 keV), L2 (10.8 keV), and M1 (2.6 keV) shells of the hafnium, other peaks visible in the lower energy parts are due to fluorescence of the housing copper and from the ^{210}Pb from Uranium-238 decay chain. The L1 and L2 peaks are used to adjust the CPE while the other peaks are used as a check.

4.5.2 Gamma line tilt correction

When there is an energy deposition in the absorber, almost all the energy is released in the crystal and only a small amount in scintillation light (typically $6 \div 7\%$ [64]). For the same energy deposition, the repartition between the light and phonon channels can vary due to the number of carrier fluctuations. These fluctuations cause events with a smaller (larger) LY to have assigned a larger (smaller) energy, resulting in a visible tilt of the gamma lines, Figure 4.22(a). This effect can be adjusted (as described in [100]) considering an energy fraction

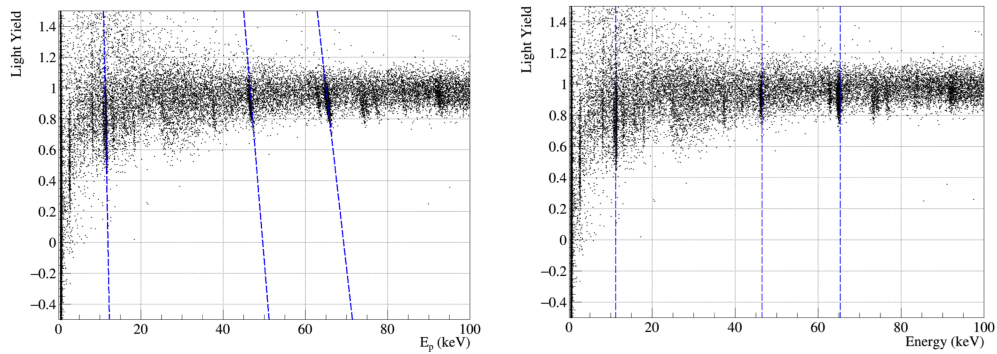
η is released as light and a fraction $(1 - \eta)$ in phonon

$$E = \eta E_L + (1 - \eta) E_P \quad (4.6)$$

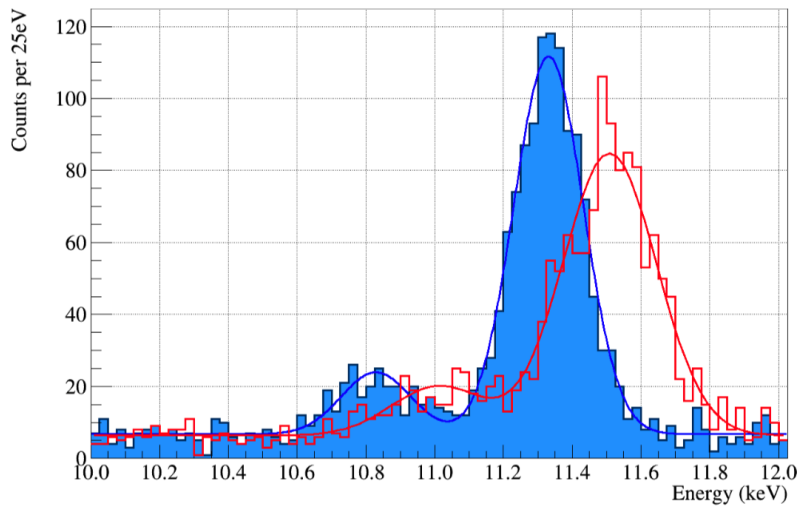
using the Light Yield definition is then possible rewrite Equation 4.6 as

$$E = \eta E_P LY + (1 - \eta) E_P \quad (4.7)$$

$$= [1 - \eta(1 - LY)] E_P \quad (4.8)$$



(a) Light Yield vs Energy before correction. (b) Light Yield vs Energy after correction.



(c) Energy spectrum before(red) and after correction(blue)

Figure 4.22: The effect of the energy correction on both the light yield and energy spectrum

It is possible to see how the gamma lines are adjusted and how this also improves the energy resolution applying the corrections just illustrated, Fig 4.22(b) and Fig. 4.22(c). The adjustment of the η and the phonon CPE factors can move the peak positions, and so subsequent adjustments are needed. Since at every iteration, the adjustments become less and less relevant usually, only a couple

of iterations are necessary. In Figure 4.23 the final energy spectrum obtained for the detector TUM40 is shown, the spectrum is optimized for the low energy region between 0.8 keV and 40 keV. In Figure 4.24 the Light Yield vs Energy plot is shown before and after all the cuts are applied.

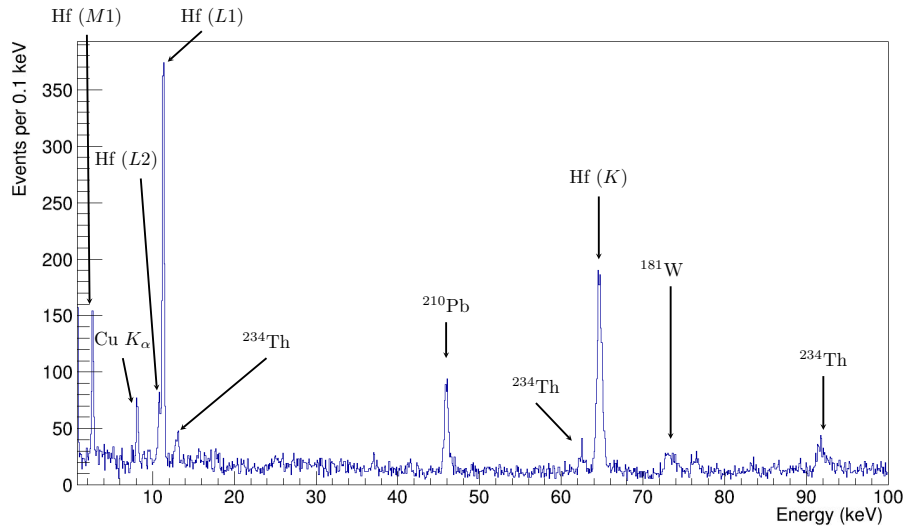


Figure 4.23: TUM40 energy spectrum. The energy scale is corrected according to Eq. 4.7. In the spectrum are visible the different gamma peaks from the ^{179}Ta electron capture (Eq. 4.5), and the gamma produced by an electron filling the vacancies at K (65.35 keV), L1 (11.27 keV), L2 (10.74 keV), M1 (2.6 keV), the Copper fluorescence at 8 keV, the gamma at 46.5 keV from ^{210}Pb , and gammas from ^{234}Th .

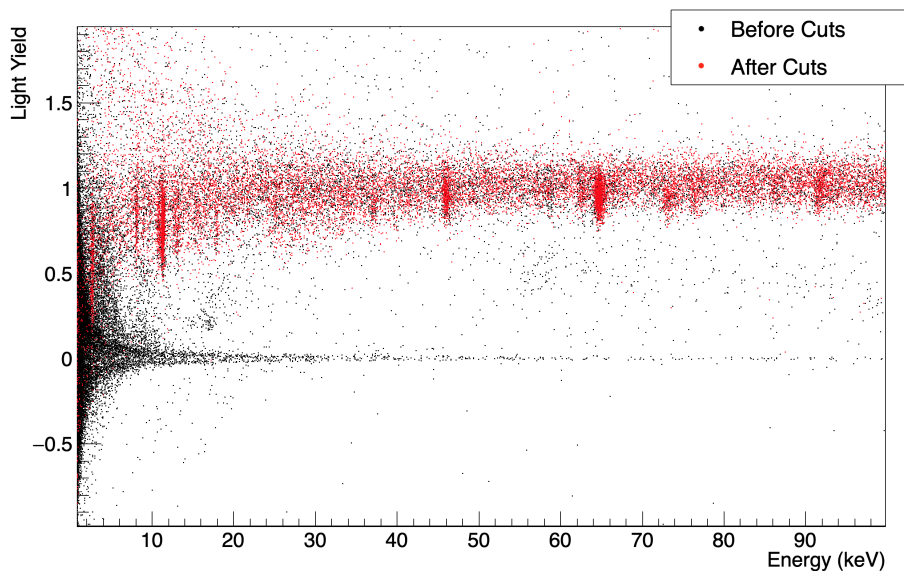
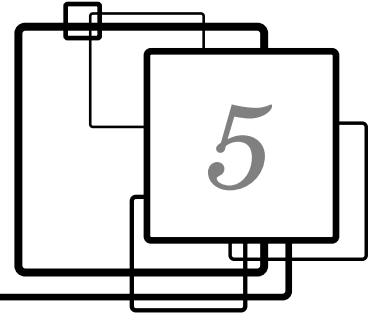


Figure 4.24: TUM40 Light Yield vs Energy Spectrum for the energy range $0.8 \div 100$ keV and light yield range $-1 \div 2$, before the cuts (red) and after all the cuts (black). The energy scale is corrected according to Eq. 4.7.

In the next Chapter, I will focus on the analysis of different detectors.



Detector Analysis

In the preparation of this work, 12 detector modules from CRESST Run 33 have been analyzed. From these 12, a subset of 5 modules has been selected. These 5 detectors present the best characteristics in terms of threshold, resolution, background, and exposure, to be used for a Dark Matter analysis.

In the first part of this Chapter, the analysis of the light vs heat scatter plots for the 5 selected detectors on the training dataset is reported and discussed. Table 5.1 summarizes the mass, dimensions, module arrangement, and the producer for each detector analyzed.

The crucial part of this work is the identification of the various events populations present in the plots. Properly determining such populations origin allows us to safely set cuts to reject spurious events and preserve the physics information. The different populations are highlighted for specific detectors, discussing the origin and the false shape features.

In the second part of the Chapter, the detector response for the different event classes is described. Finally, in the last part of the Chapter the unblinded data after all the selections are shown. The energy spectrum and the Light Yield vs energy scatter plot for the full dataset are presented.

Detector	Mass (gr)	Dimension (mm)	Module Type	Producer
TUM40	248	$32 \times 32 \times 40$	TES directly evaporated on crystal held by CaWO_4 sticks	TUM grown crystal
Frederika	266	$34.6 \times 40.2 \varnothing$	TES on glued carrier crystal and parylene	MD GREAL
Anja	308	$39.9 \times 40.3 \varnothing$	TES on glued carrier crystal and parylene	Vladimir Kochurykhin
Verena	306	$39.5 \times 40.3 \varnothing$	TES directly evaporated on crystal	MD GREAL
Lise	306	$39.6 \times 40.3 \varnothing$	TES on glued carrier crystal and parylene	Vladimir Kochurykhin

Table 5.1: For each detector are reported the mass, the size, the configuration, and the producer. All detectors crystals are made of CaWO_4 . Each detector is equipped

5.1 Detector population

5.1.1 TUM40 detector

The TUM40 crystal was grown at the Technische Universität München facility, starting from selected radio pure CaCO_3 and WO_3 powders [104]. The module setup is illustrated in Figure 5.1.

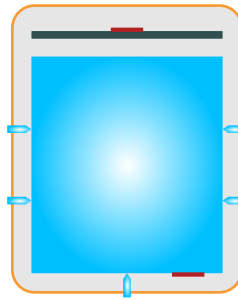


Figure 5.1: TUM40 crystal layout: in the figure are visible the scintillating CaWO_4 sticks holding the crystal and the scintillating foil (light gray) inside the copper housing (orange). Both the TESs evaporated on the light and phonon detector are depicted in red.

In Figure 5.2, the scatter plot of the light Pulse Height vs the phonon Pulse Height for TUM40 is presented

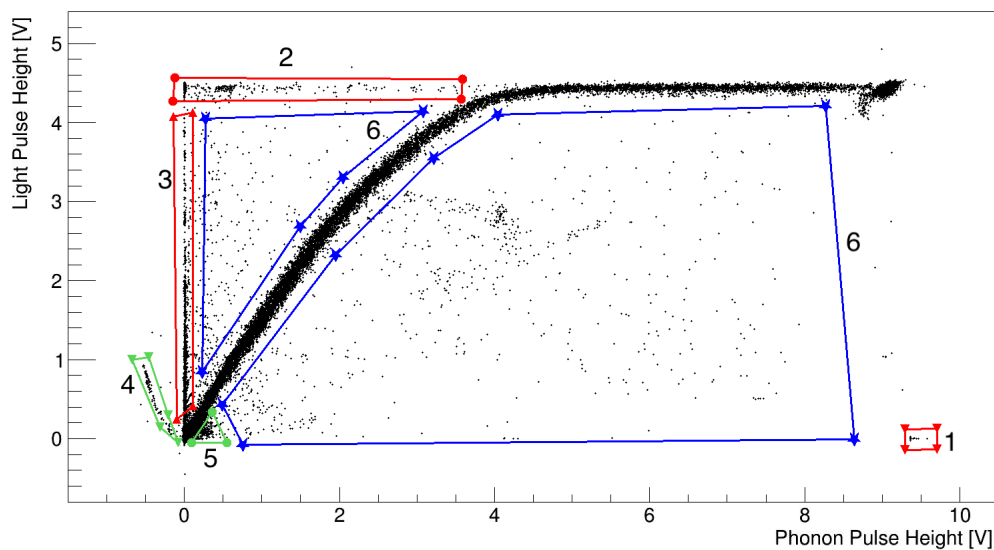


Figure 5.2: The scatter plot of the raw pulse height of the light detector vs the pulse height of the phonon detector for TUM40. Plot obtained with the training dataset.

Two general features can be observed in Figure 5.2:

- most of the data are distributed in a rectangle; the rectangle sides are the TES dynamic transition range (phonon on the x-axis and light on the y-axis). Since each TES has its own behaviour, the box size is different for each detector.

- the presence of the main event population starting at the origin and ending on the rectangle opposite vertex

Outside the main event population, several others can be found. The different event families are boxed in different colors and with different markers. In the following, the various populations are analyzed, highlighting the features of the different pulse shapes and discussing the origin.

5.1.1.1 TUM40 Region 1

The events highlighted in the region labeled 1, in the right down corner of Figure 5.2, have a huge phonon signal and almost no light. In Figure 5.3 a typical events from this population is shown, both for phonon and light channels.

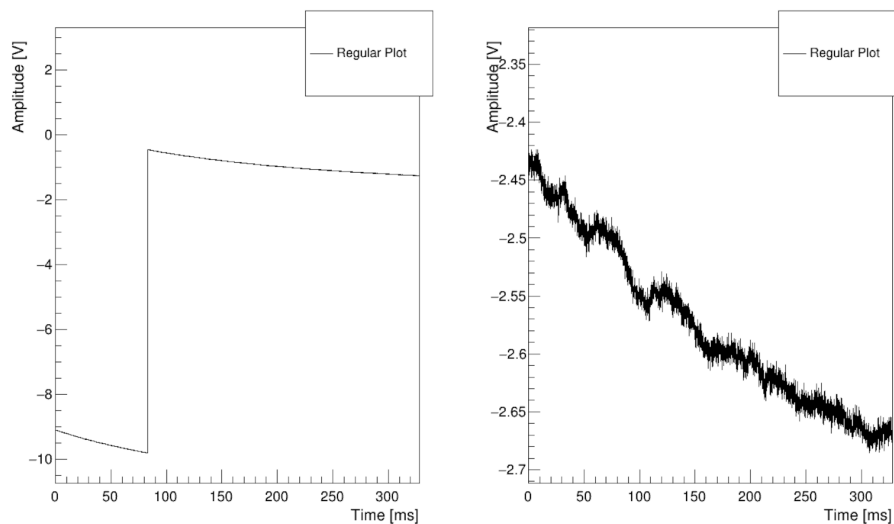


Figure 5.3: The phonon (left) and light (right) pulse recorded for an event in region 1.

The phonon signal shown in the left figure is unphysical since the energy deposition is larger than the TES dynamic range. The signal is due to the offset reset of the phonon channel. When the baseline reaches the lower limit of the ADC range, the offset is reinitialized to zero, generating the abrupt transition recorded in this event window. This pulse shape can be rejected from the good data set using the baseline difference cut (see Section 4.3.4). A descending baseline behaviour can be observed for these specific events, both in the heat and light channels, likely resulting from a previous large energy deposition and light emission.

5.1.1.2 TUM40 Region 2

The events from this population have a saturated light signal paired with a relatively small phonon signal. A typical signal is shown in Figure 5.4.s

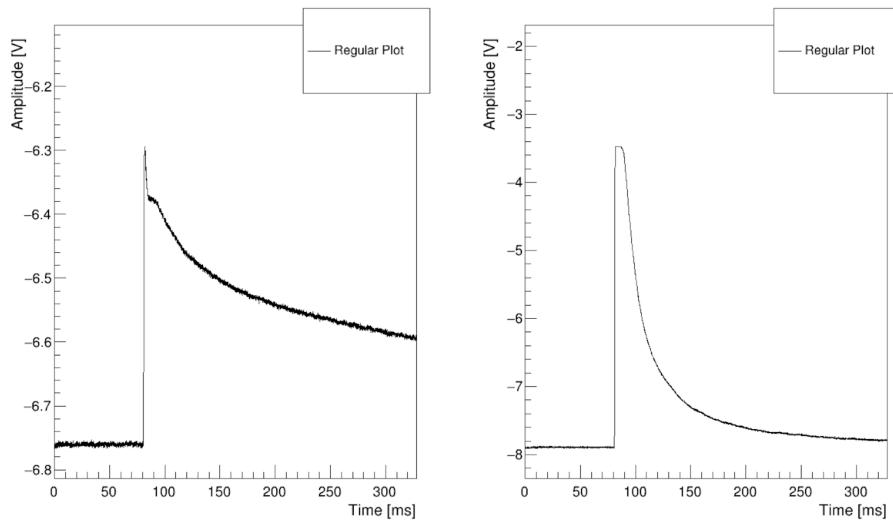


Figure 5.4: The phonon (left) and light (right) pulse recorded for an event in the region 2.

The phonon channel pulse is characterized by a spike followed by a tail not recovering to the previous baseline level. This signal is most likely induced by direct interaction in (or very near) the TES. The non-recovering behaviour is due to the large energy release that is not compensated by the feedback circuit described in Section 3.2.2, resulting in a SQUID quantum flux loss that produces a change in the baseline level. The presence of large energy deposition in the light channel suggests that an α particle can be the cause of this event.

5.1.1.3 TUM40 Region 3

As shown in Figure 5.2, these events present almost no signal in the phonon channel with a light counterpart well above the threshold. Figure 5.5 shows a typical couple of signals from this region.

In the two plots, corresponding to the heat and light signals, only decreasing baselines are visible. This situation is the result of an interaction happening when the trigger is blocked (see Section 4.1) after a triggered pulse. If the baseline is still above threshold when the trigger is reactivated, the two pulses are recorded. In this population, the decaying baseline present in the light detector is much larger than the one present in the phonon channel. This kind of event is likely due to the tail of interaction in the light detector. Also, this population is removed by the baseline difference cut (see Section 4.3.4).

5.1.1.4 TUM40 Region 4

These events present a small signal in the light channel and a negative measured phonon pulse. Figure 5.6 shows a typical event from this selection.

The class of event depicted in Figure 5.6 is similar to the one illustrated in Section 5.1.1.3. Differently from before, these events come from interactions in

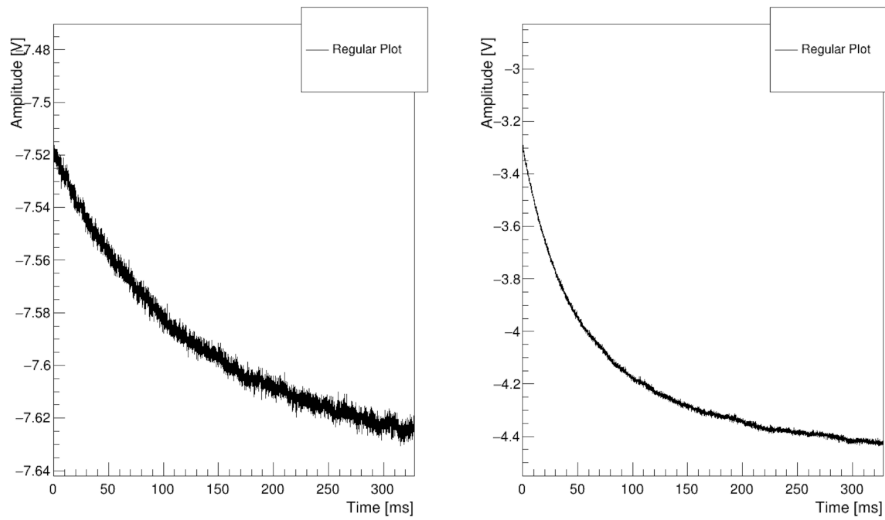


Figure 5.5: The phonon (left) and light (right) pulse recorded for an event in the region 3.

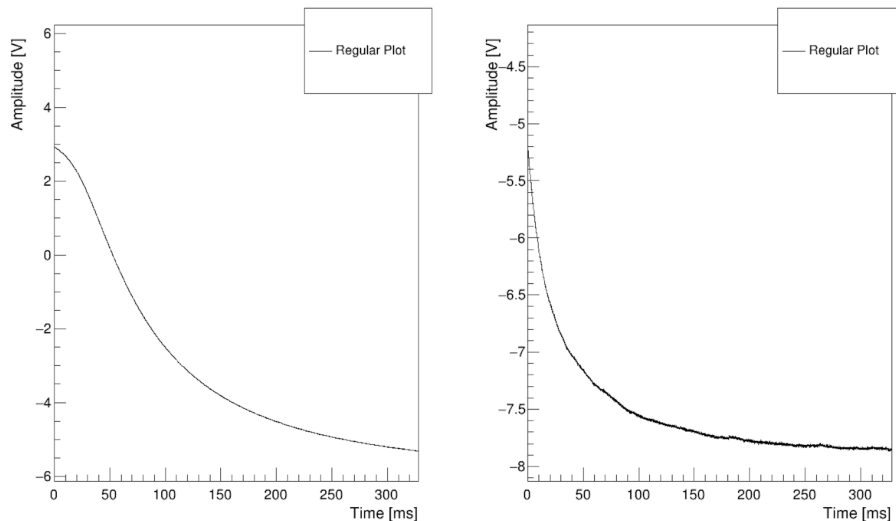


Figure 5.6: The phonon (left) and light (right) pulse recorded for an event in region 4.

the phonon channel while the trigger was blocked. The raw pulse height estimation algorithm fails, providing a negative amplitude for these events. This effect is generated by the computing method. The Pulse Height is evaluated computing the difference between the maximum value recorded in the time window and simple linear fit of the baseline. The baseline value is obtained fitting the first ~ 75 ms of the triggered window (first 23% of recorded data points) with a linear polynomial. In most cases, this is sufficient to have a reliable measure of the Pulse Height.

For the class of events under examination, the maximum misidentified as the peak is found at $t = 0$, which is overestimated by the simple linear baseline model. When the difference between the maximum value and the corresponding baseline

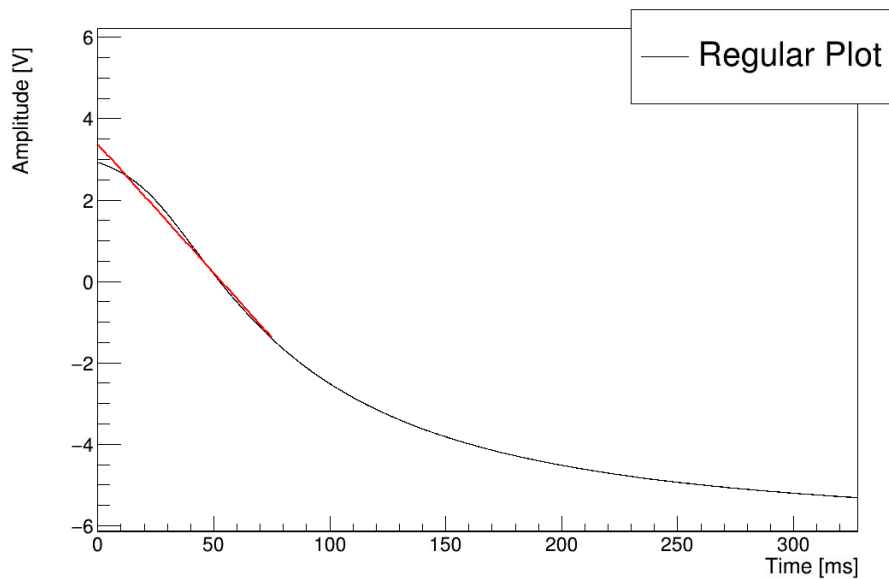


Figure 5.7: The fit used to estimate the baseline level is shown, the fit (solid red) of the first 23% recorded point is shown superimposed to the recorded pulse. The maximum point recorded is for $t = 0$, which is below the baseline computed value at that time. This fact leads to a negative raw measurement of the phonon channel Pulse Height.

value a $t = 0$ is computed, the result is negative, producing a negative estimation of the phonon channel PulseHeight. In Figure 5.7 the baseline reconstruction for the phonon event of Figure 5.6 is shown. It is clearly visible how the baseline (solid red line) at $t = 0$ is higher than the recorded pulse maximum.

5.1.1.5 TUM40 Region 5

From the scatter plot in Figure 5.2, these events present a small signal in both the phonon and the channel. Figure 5.8 shows a typical event from this region.

These events present an increasing linear signal in the phonon channel. This event class is generated by temperature feedback correction. The detector is heated to go back to the operating point, generating a drift of the baseline level and the following trigger fires.

5.1.1.6 TUM40 Region 6

The last class of events is not clustered in a specific region but is spread all around in the scatter plot. Nonetheless, these events have a common origin. In Figure 5.9 an event from this class is shown.

This class of events is characterized by a SQUID reset, followed by an ADC reset: this produces the double spike in the phonon channel. The combination of the two effects depends on the Squid Quantum Flux and the initial baseline, the final result is not predictable, and the events are scattered in the plane.

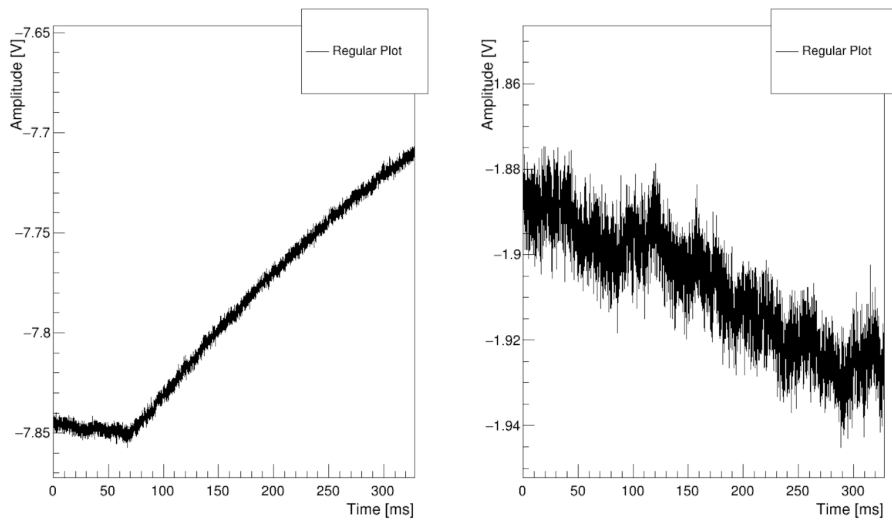


Figure 5.8: The phonon (left) and light (right) pulse recorded for an event in region 5.

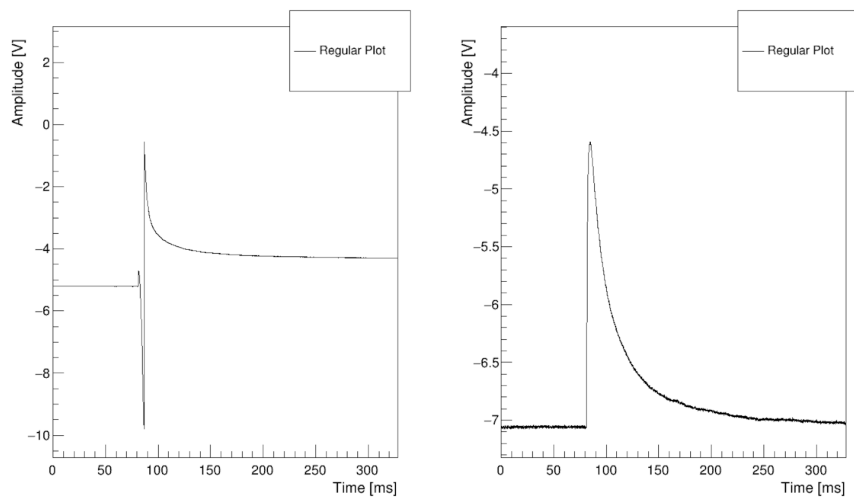


Figure 5.9: The phonon (left) and light (right) pulse recorded for an event in the region 6.

5.1.2 Frederika detector

Detector Frederika is built from a commercial CaWO_4 crystal. These crystals are more contaminated by radioactive isotopes than those produced in the CRESST facility at Technische Universität München (TUM). On detector Frederika, the phonon detector TES is evaporated on a small carrier crystal glued to the main absorber. As shown in the scheme of Figure 5.10, the detector is held by clamps coated with parylene that provides scintillation light to tag events generated on the clamps' surface.

In Figure 5.11, the scatter plot of Light versus Phonon Pulse Height for detector Frederika is shown. Some differences are evident compared to TUM40, such as the presence of substructures below the main population and a cluster

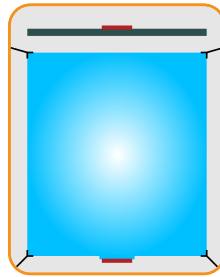


Figure 5.10: The Frederika crystal layout is shown. In the figure, it is visible the scintillating CaWO_4 crystal held by clamps and the scintillating foil (light gray) inside the copper housing (orange). The TES (dark red) of the phonon channel is evaporated on a smaller carrier crystal glued to the main absorber. The clamps holding the detector are coated with parylene making the detector housing fully scintillating.

of events with Phonon Pulse Height $\sim 8.5\text{V}$ and Light Pulse Height $\sim 4.5\text{V}$

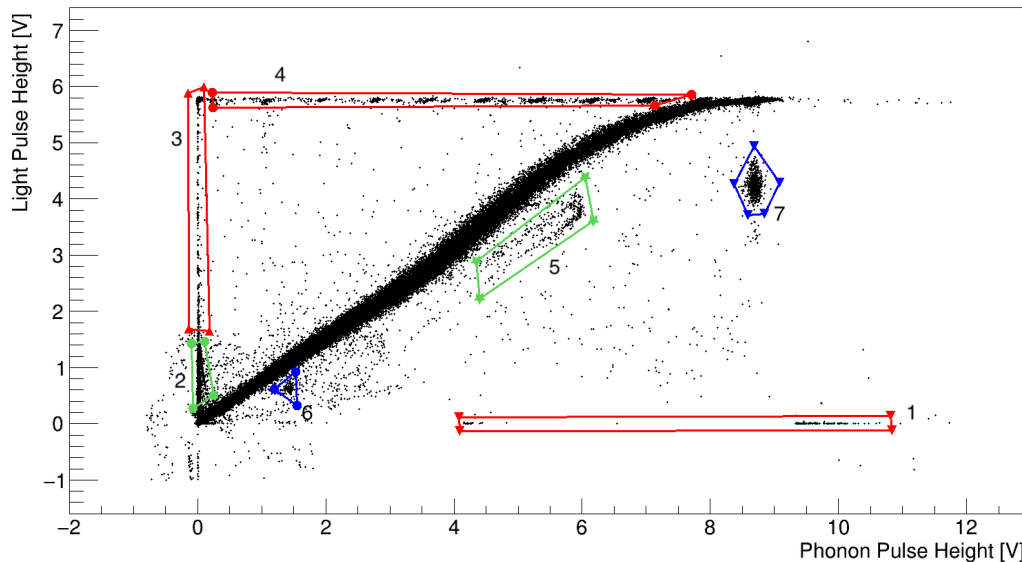


Figure 5.11: The scatter plot of the pulse height of the light detector vs the pulse height of the phonon detector for Frederika. Plot obtained with the training dataset.

5.1.2.1 Frederika Region 1

These events present a large signal in the phonon channel and almost no signal in the light channel. Figure 5.12 shows a typical event from this region.

This class of events is due to the ADC reset similar to the event with no light described for TUM40 in 5.1.1.1.

5.1.2.2 Frederika Region 2

As shown in Figure 5.11, these events have a zero phonon signal and low light signal. Figure shows 5.13 a typical event from this region.

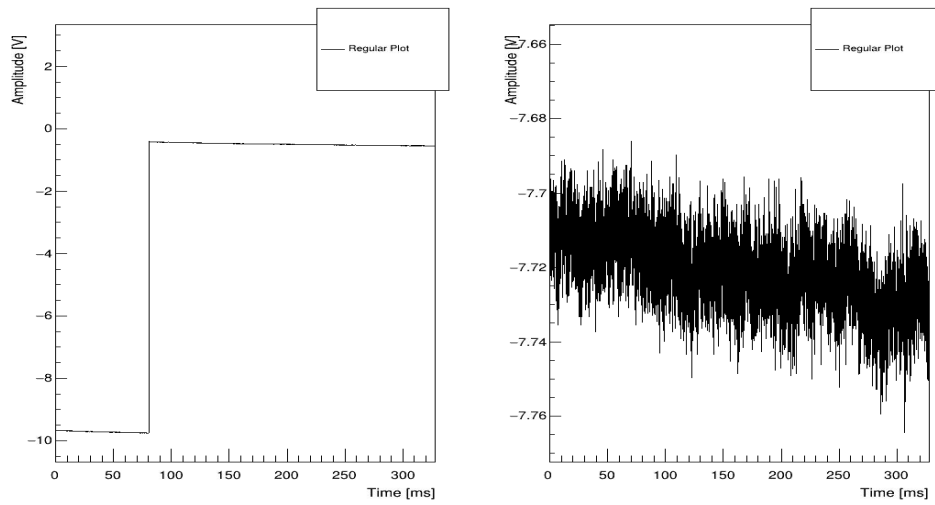


Figure 5.12: The phonon (left) and light (right) pulse recorded for an event in the region 1.

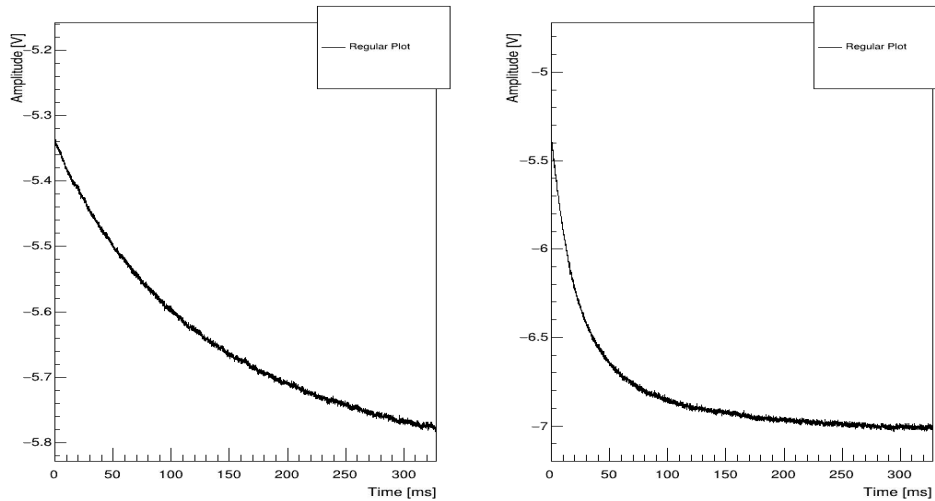


Figure 5.13: The phonon (left) and light (right) pulse recorded for an event in region 2.

These events are induced by an energy release when the trigger is inhibited or by a previous large energy deposit with a long tail. When the trigger is enabled again, event tail is above the threshold, so the trigger fires, and the event is recorded. As the tail is much larger in the light channel, these events likely come from light detector direct hit.

5.1.2.3 Frederika Region 3

As can be seen from the scatter plot in Figure 5.11, these events present a zero phonon signal and a quite large light signal. Figure shows 5.14 a typical event from this region.

The event in Figure 5.15 shows an empty baseline for the phonon signal and

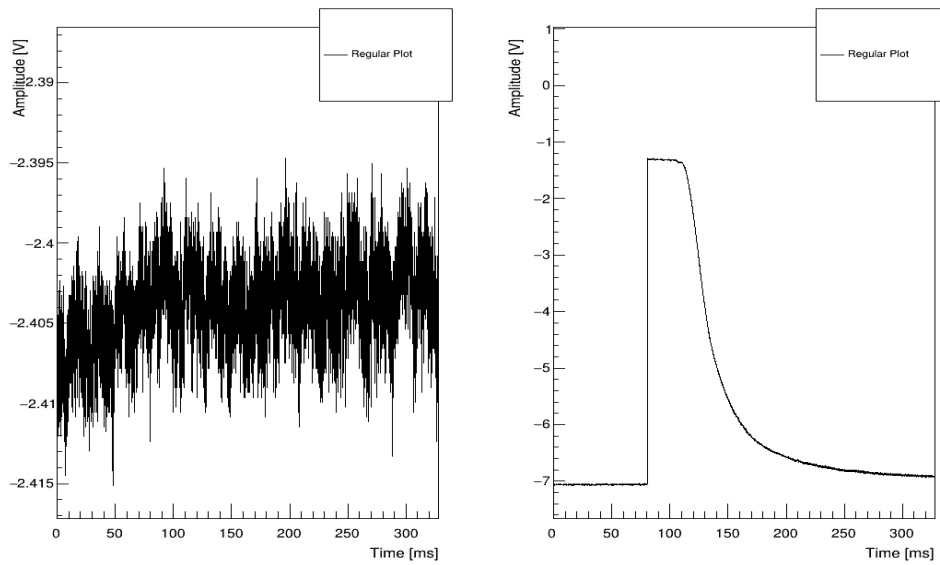


Figure 5.14: The phonon (left) and light (right) pulse recorded for an event in region 2.

a saturated pulse for the light signal. An event like this can be produced only by direct hit of the light detector by α or β from the detector housing, which does not reach the main absorber.

5.1.2.4 Frederika Region 4

From the scatter plot in Figure 5.11, one can see that these events present a saturated light signal and clustered events in the phonon signal. Figure shows 5.15 a typical event from this region.

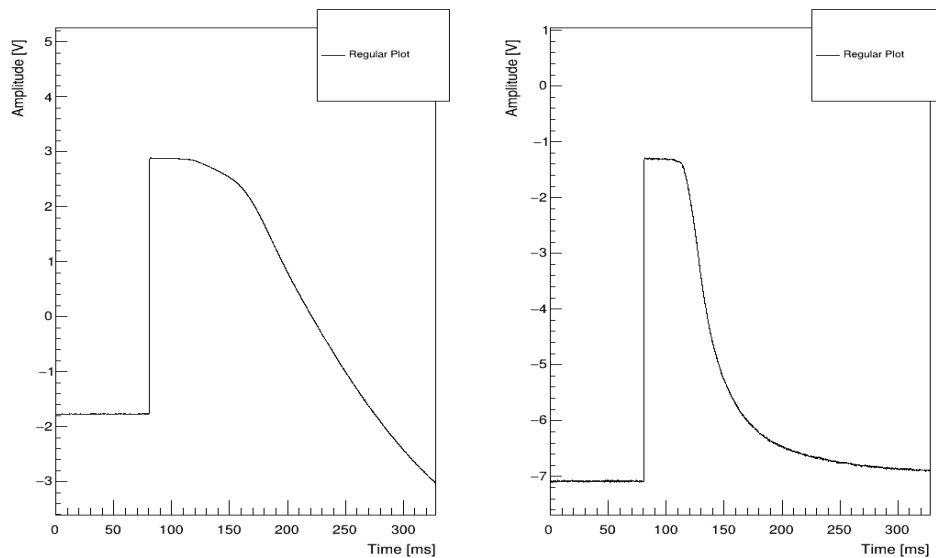


Figure 5.15: The phonon (left) and light (right) pulses recorded for an event in Region 4.

This class of events is characterized by large energy release in the phonon channel, which causes the baseline change (SQUID quantum flux loss) and a saturated signal in the light channel. The SQUID quantum loss and corresponding baseline change explain the clustering of events, as described in Section 4.3.4.

5.1.2.5 Frederika Region 5

Figure 5.16 shows a typical event from this region. These events populations (see Figure 5.11) produce lines right below the main population. These events are characterized by pulses happening when the trigger is inhibited just before the trigger is enabled again.

The presence of a pulse above the threshold makes the trigger fires. However, the saved pulse has a shorter pre-trigger baseline. When the baseline fit algorithm tries to reconstruct the proper value, part of the pulse is included in the fit. This leads to an overestimation of the baseline value.

Despite being correctly identified, the peak has a smaller Pulse Height measurement due to how the height is computed. In Figure 5.17 is shown how the naive baseline computation already described for detector TUM40 reduce the computed Pulse Height of this class of events.

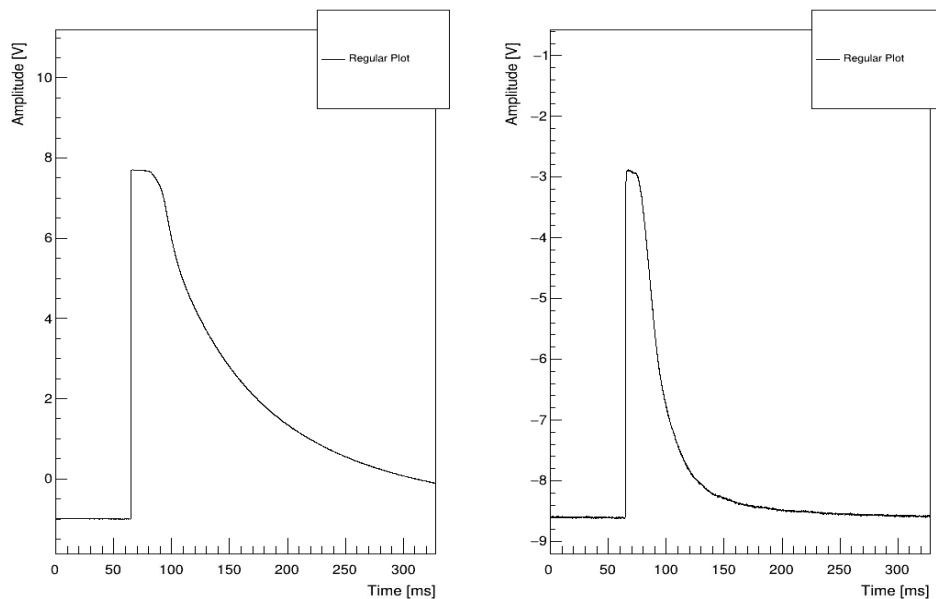


Figure 5.16: The phonon (left) and light (right) pulses recorded for an event in region 5.

5.1.2.6 Frederika Region 6

These events are right below the main population at low Pulse Height, clustered at about 1.7 V in phonon pulse height (see Figure 5.11). Figure 5.18 shows a typical event from this region with the fit superimposed.

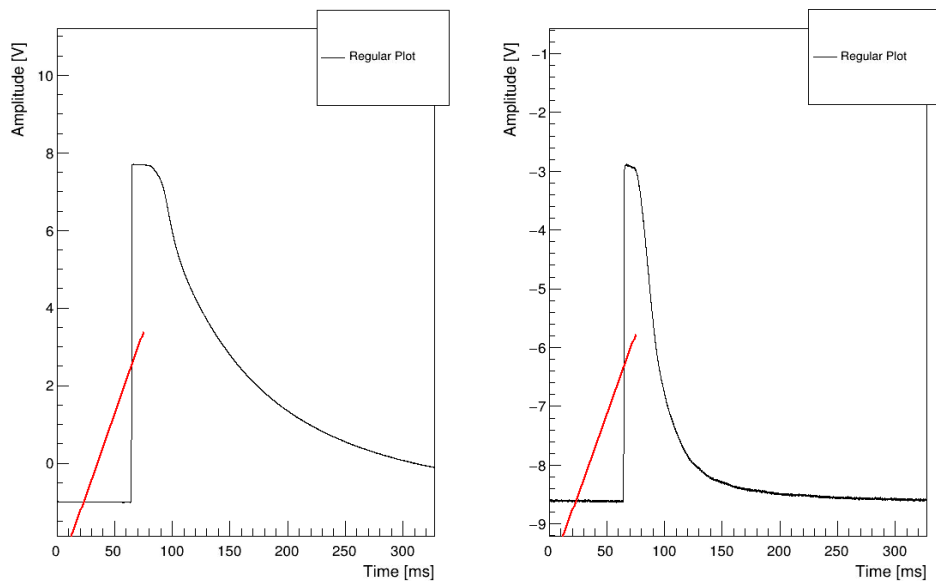


Figure 5.17: The phonon (left) and light (right) pulses recorded for an event in region 5 are shown. In red the linear fit of the first 23% of the recorded pulse.

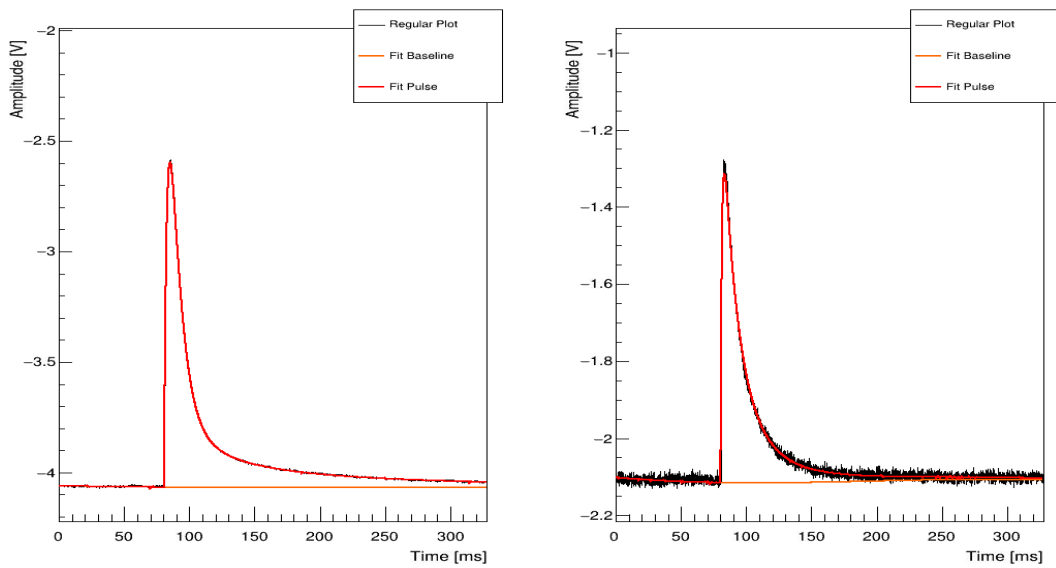


Figure 5.18: The phonon (left) and light (right) pulses recorded for an event in region 6 with the fit superimposed.

The event is shown in Figure 5.18 does not appear problematic, and the fit is reliable. The events in this selection are nuclear recoil induced by ^{210}Po decay on the detector surface. The emitted α particle escapes from the crystal, impinging in the scintillating and reflecting foil surrounding the detector. This interaction produces scintillation light that shifts the nuclear recoil outside the dark band allowing its rejection.

5.1.2.7 Frederika Region 7

The events in this contour present a saturated phonon signal and a light signal below the main population. Figure 5.19 shows a typical event from this selection with the fit superimposed. The remarkable feature of this class of events is the very large fitted amplitude of the phonon events.

These events are due to α particles releasing energy of the order of MeV in the crystal. They appear outside the main population, which is the electron/gamma population, due to the lower Quenching Factor. These events are physical events not removed by the cuts. The associated light places them in the α band well separated from the dark events acceptance region.

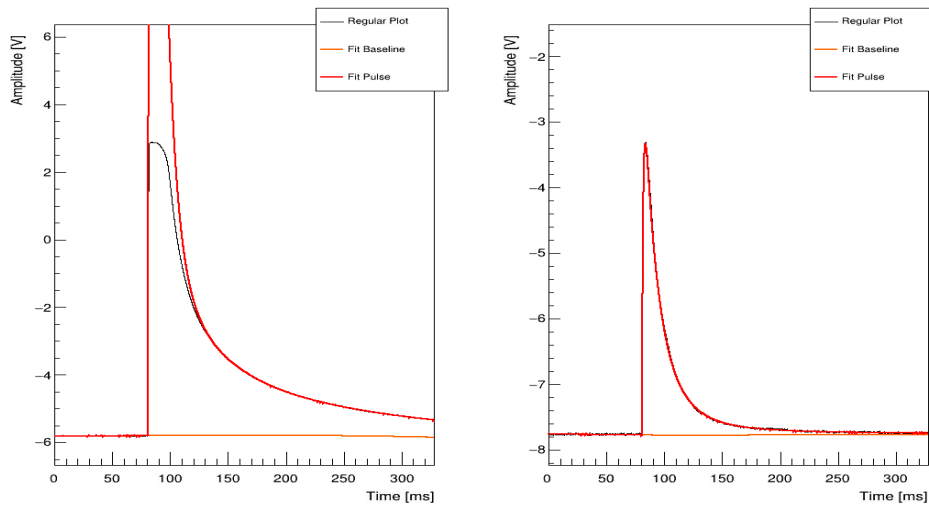


Figure 5.19: The phonon (left) and light (right) pulse recorded for an event in region 7 with the fit superimposed.

5.1.3 Anja detector

Detector Anja is made from a commercial crystal made by the same company, which delivered Frederika¹. The module setup is identical to the one of detector Frederika (see Figure 5.10).

In Figure 5.20, the scatter plot of Light versus Phonon Pulse Height for detector Anja is shown. Despite the detector has the same setup of Frederika and is from the same producer, the scatter plot of Light versus Phonon Pulse Height is quite different. The differences come mainly from TES performances and responses.

5.1.3.1 Anja Region 1

The events in this region present a negative phonon Pulse Height. Figure 5.21 shows a typical event from the selection.

¹Producer Vladimir Kochurykhin

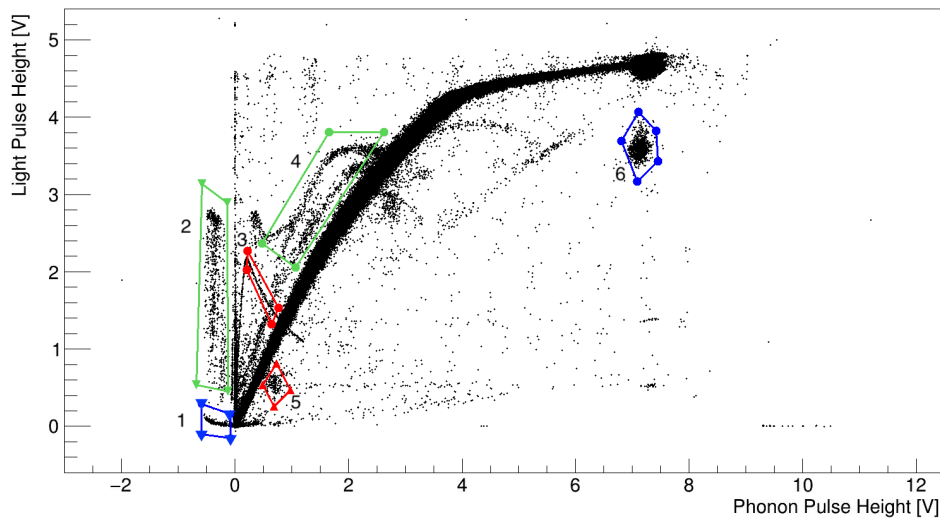


Figure 5.20: The scatter plot of the raw pulse height of the light detector vs the pulse height of the phonon detector for Anja. Plot obtained with the training dataset.

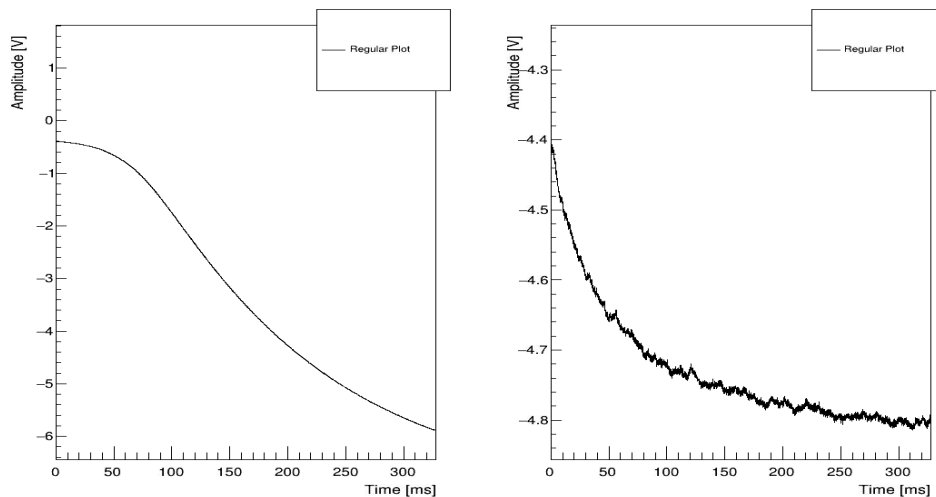


Figure 5.21: The phonon (left) and light (right) pulse recorded for an event in region 1.

This class of event has only the tail of the pulse in the recorded window. These events have a negative phonon pulse height for the same reasons explained for detector TUM40 (Sections 5.1.1.3 and 5.1.1.4) and Frederika (Section 5.1.2.2).

5.1.3.2 Anja Region 2

The events in this contour present a negative phonon Pulse Height. Figure 5.22 shows a typical event from the selection. Similarly to the class of events in region 2 (Section 5.1.3.1), the computed phonon pulse height is negative, but the phonon pulse height shows a larger pulse height compared to the one described in the previous Section.

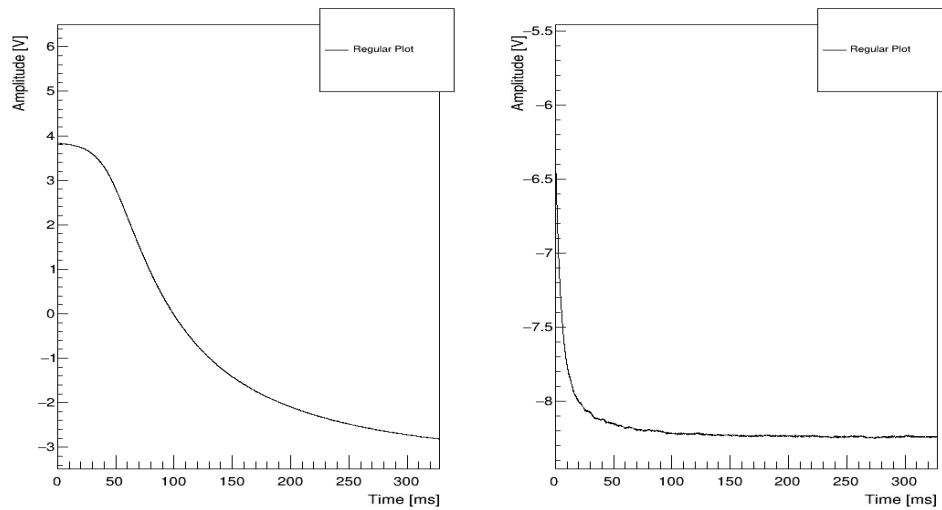


Figure 5.22: The phonon (left) and light (right) pulses recorded for an event in region 2.

The event in Figure 5.22 differs from the one in Figure 5.21 for the amplitude of the pulse tail, as both these classes of events contain only the final part of the pulse at the beginning of recorded time window. The difference is only due to the energy released during the inhibited trigger time.

5.1.3.3 Anja Region 3

The events in this region are clustered in a diagonal line with a negative slope. The typical event of this region is shown in Figure 5.23. This class of event presents only the tail of the recorded pulse. In the phonon channel, the presence of two different decay times can be observed. The two decay times are likely due to the pile-up of two events of different energies. This behaviour is generated by a SQUID reset during the trigger inhibited period.

5.1.3.4 Anja Region 4

This class of events in region 4 is due to anticipated pulses, as shown in Figure 5.24. The reason why this class of events is outside the main population is described in section 5.1.2.5.

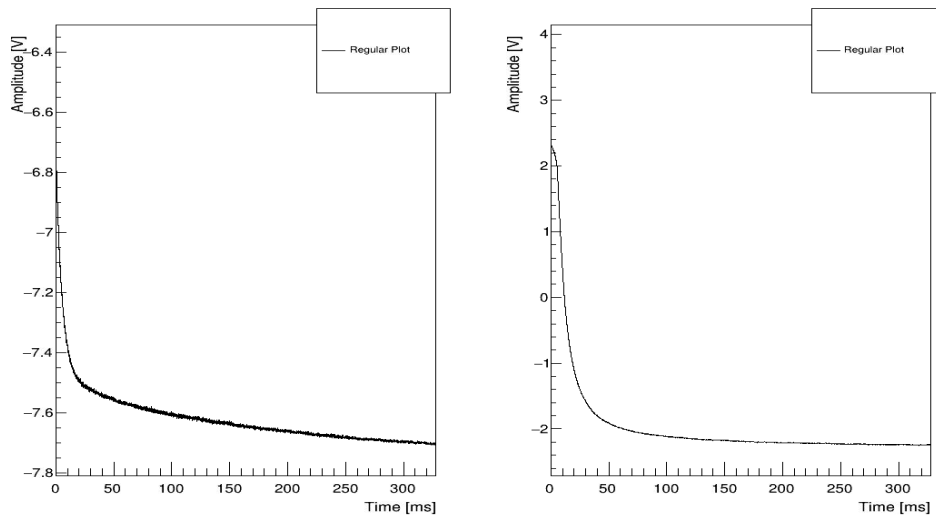


Figure 5.23: The phonon (left) and light (right) pulse recorded for an event in Red Full Circle.

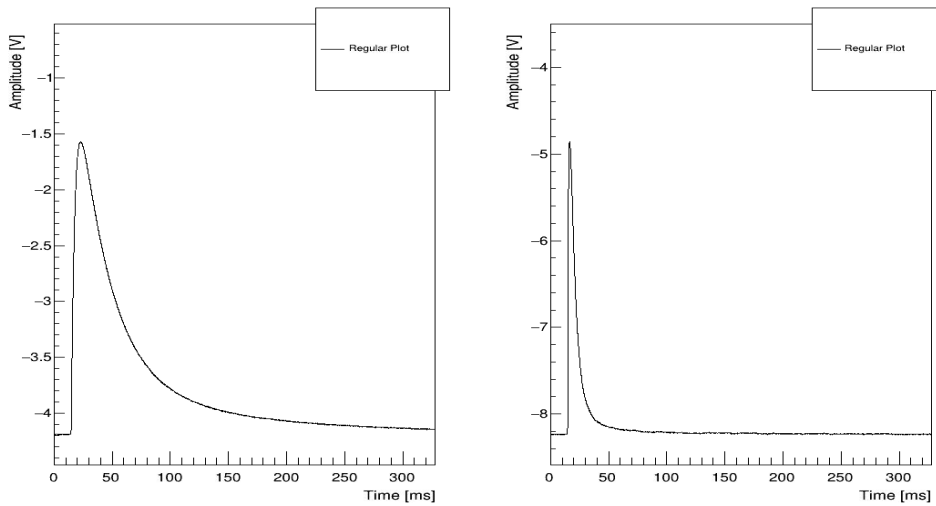


Figure 5.24: The phonon (left) and light (right) pulse recorded for an event in region 4.

5.1.3.5 Anja Region 5 and region 6

Events from region 5 and region 6 are below the main population are shown respectively in Figure 5.25 and Figure 5.26, with the pulse fit superimposed. The events have no major problem, and the fit is reliable. They are due to ^{210}Po decay and α particles interacting in the crystal, as already discussed for detector Frederika in Section 5.1.2.7.

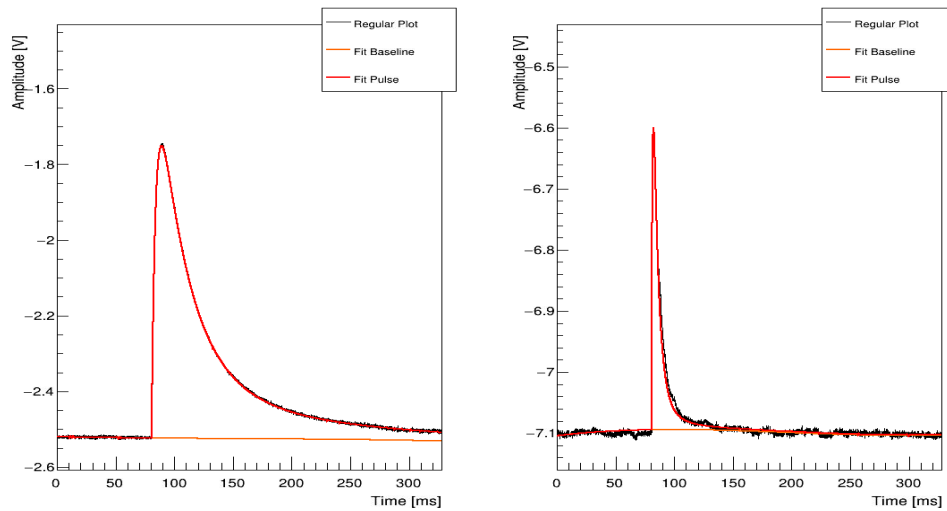


Figure 5.25: The phonon (left) and light (right) pulse recorded with the fit superimposed for an event in region 5.

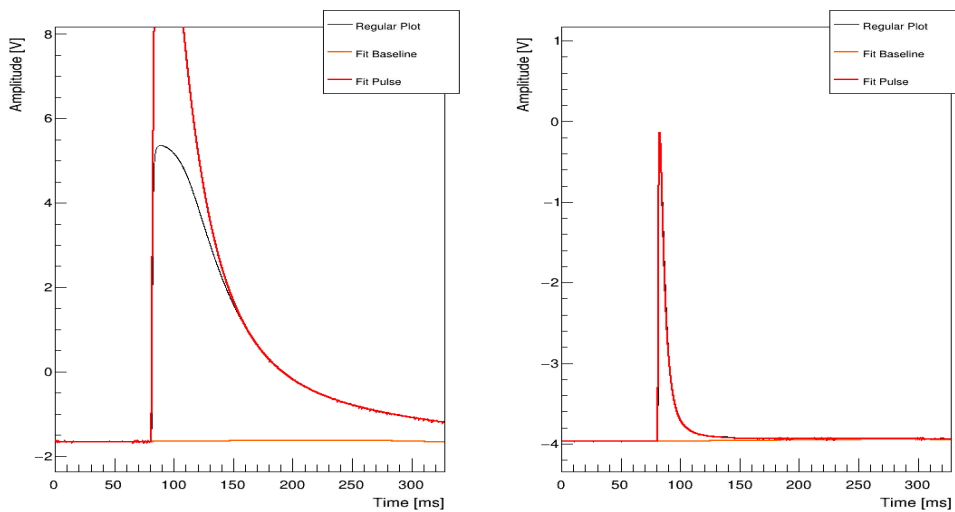


Figure 5.26: The phonon (left) and light (right) pulse recorded with the fit superimposed for an event in region 6.

5.1.4 Lise detector

Detector Lise is another commercial crystal made by the same company which delivered Frederika and Anja. The module setup is the same of detector Frederika and Anja previously described (see Figure 5.10). The scatter plot for Light versus Phonon Pulse Height is shown in Figure 5.27.

5.1.4.1 Lise Region 1

The events in this contour have no light signal and large phonon signal. As seen for the other detector, the cause of this events is the phonon channel ADC reset as can be seen in Figure 5.28

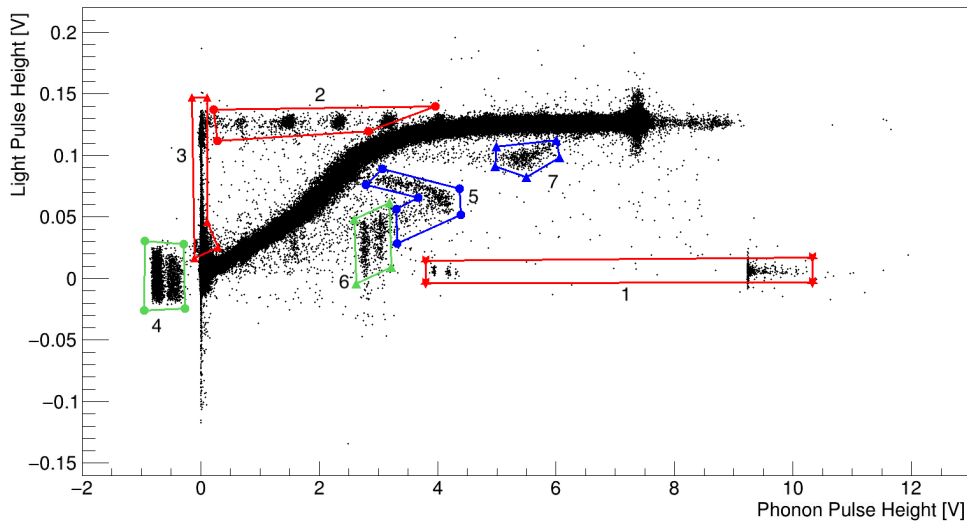


Figure 5.27: The scatter plot of the pulse height of the light detector vs the pulse height of the phonon detector for Lise. Plot obtained with the training dataset.

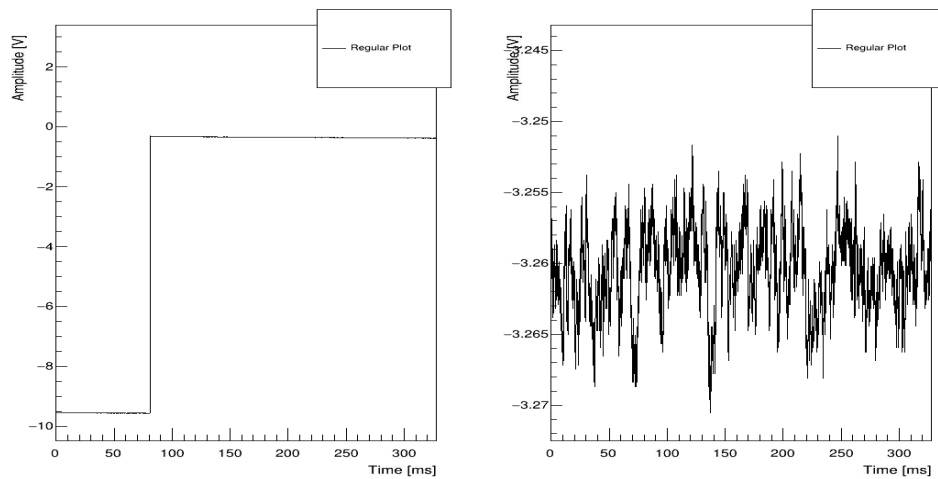


Figure 5.28: The phonon (left) and light (right) pulse recorded for an event in region 1.

5.1.4.2 Lise Region 2

This class of events presents a saturated light. As seen from the analysis of the 3 previous detectors, these events are caused by large energy release in the detector, associated with large light emission, causing a SQUID reset which distorts the recorded phonon pulse as can be seen from Figure 5.29.

5.1.4.3 Lise Region 3

The events in the region 4 are events characterized by the absence of a signal in the phonon channel, as can be seen in Figure 5.30. As already discussed in Section 5.1.2.3 these events are induced by direct hits in the light detector.

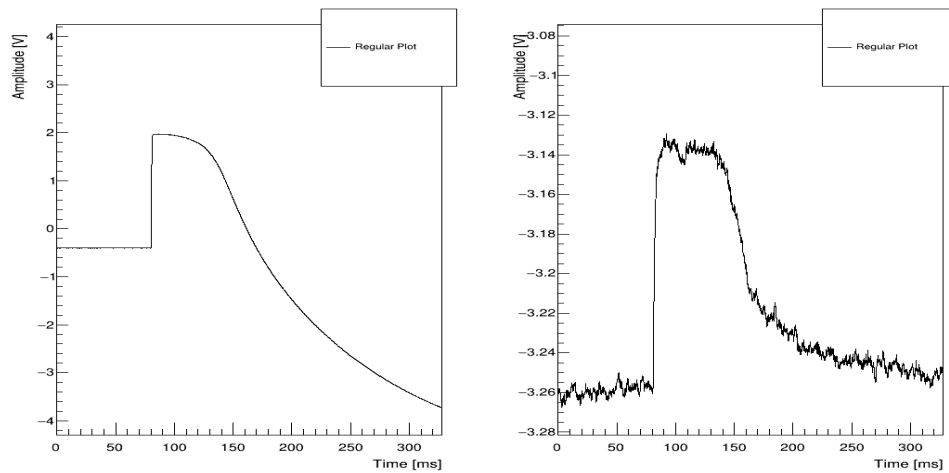


Figure 5.29: The phonon (left) and light (right) pulse recorded for an event in region 2.

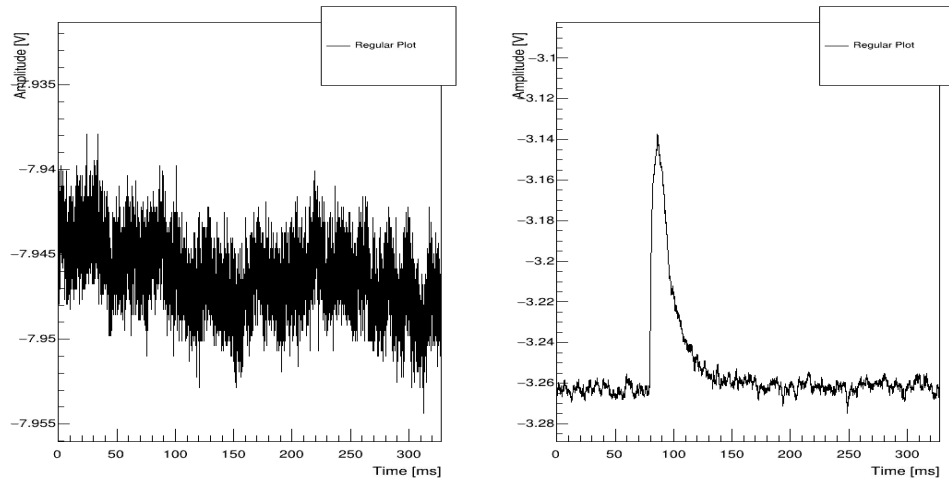


Figure 5.30: The phonon (left) and light (right) pulse recorded for an event in region 4.

5.1.4.4 Lise Region 4

The events present in this selection have a negative computed phonon pulse height. The typical events from this population is shown in Figure 5.31. The cause of the negative phonon pulse height is due to the method used to evaluate the baseline as already described for detector TUM40 5.1.1.4.

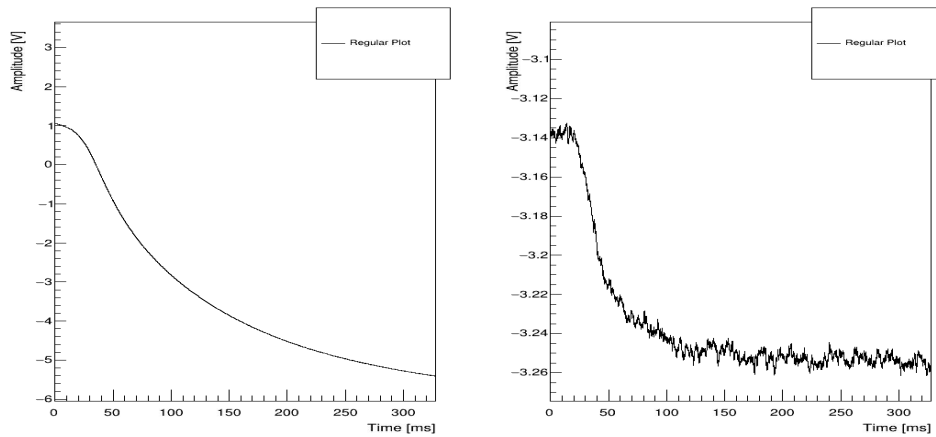


Figure 5.31: The phonon (left) and light (right) pulse recorded for an event in region 4.

5.1.4.5 Lise Region 5 and region 6

The events in these two classes, despite having a different shape in the scatter plot of Figure 5.27 are due to the same type of events: anticipated pulse are shown. Events from region 5 and region 6 contour are shown in Figure 5.32 and Figure 5.33 respectively. The two populations are distinguished by the pulse position in time and the pulse shape. Pulses from the vertical lines in region 6 are larger and start to rise ~ 60 ms, while pulses from region 5 rise ~ 20 ms and have a smaller amplitude.

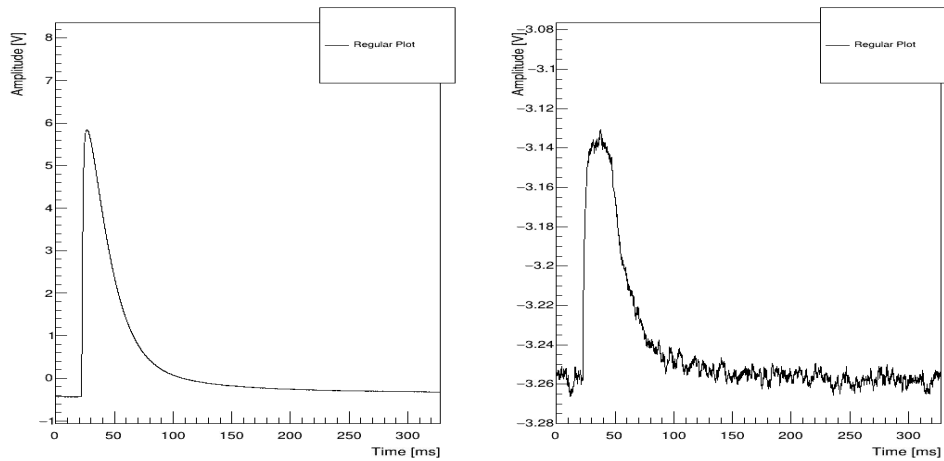


Figure 5.32: The phonon (left) and light (right) pulse recorded for an event in region 5.

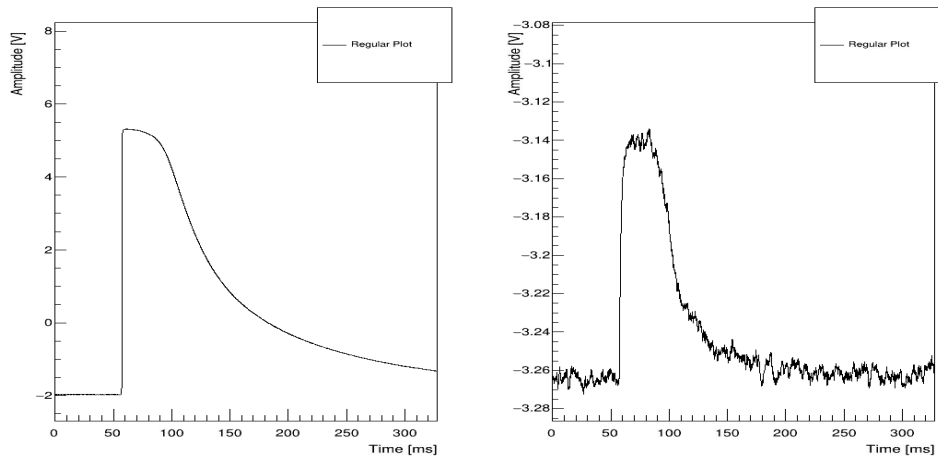


Figure 5.33: The phonon (left) and light (right) pulse recorded for an event in region 6.

5.1.4.6 Lise Region 7

Events from this contour are just below the main population, despite having a completely saturated light signal (Figure 5.34). The reason for the light pulse height underestimation is the slightly anticipated position of the pulse with respect to the nominal one. This is the same effect already discussed in Section 5.1.2.5. The pulse deviation from the nominal position is negligible, and it does not affect the fit performance (Figure 5.34).

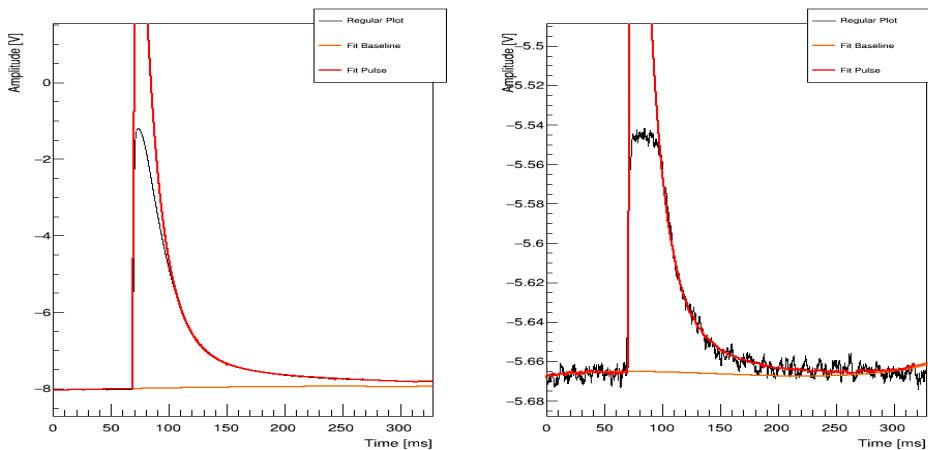


Figure 5.34: The phonon (left) and light (right) pulse recorded with fit superimposed for an event in Region 7.

5.1.5 Verena detector

Detector Verena is made with a commercial crystal made by the same company which delivered Frederika, Anja, and Lise crystals. The module setup is almost

the same as detectors previously described and is shown in Figure 5.35. There are two main differences with the setup of Frederika, Anja, and Lise.

The TES of the phonon detector is directly evaporated on the crystal, and no carrier is present. Moreover, the clamps are not coated with parylene, so they are not scintillating.

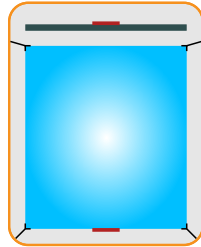


Figure 5.35: In figure is shown the Verena crystal layout. In figure, it is visible the scintillating CaWO_4 crystal held by clamps and the scintillating foil (light gray) inside the copper housing (orange). The TES (dark red) of the phonon channel is directly evaporated on the main absorber. The clamps holding the detector opposite to Frederika, Anja, and Lise are not coated with parylene.

In Figure 5.36, the scatter plot of Light versus Phonon Pulse Height for detector Verena is shown.

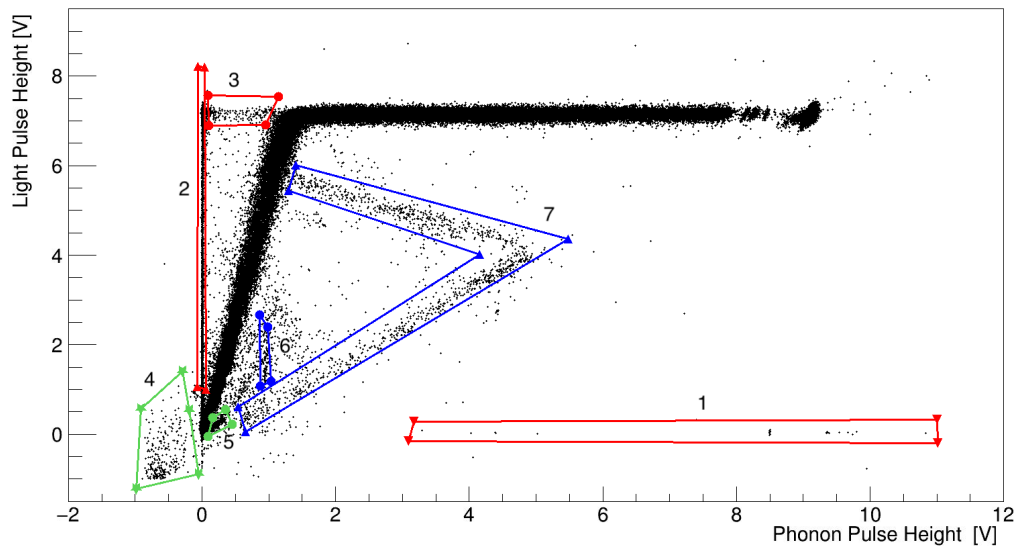


Figure 5.36: The scatter plot of the pulse height of the light detector vs the pulse height of the phonon detector for Verena. Plot obtained with the training dataset.

5.1.5.1 Verena Region 1

The events in this selection are not caused by a physical event but are due to ADC reset when the voltage reach -10V. An event from this selection is shown in Figure 5.37.

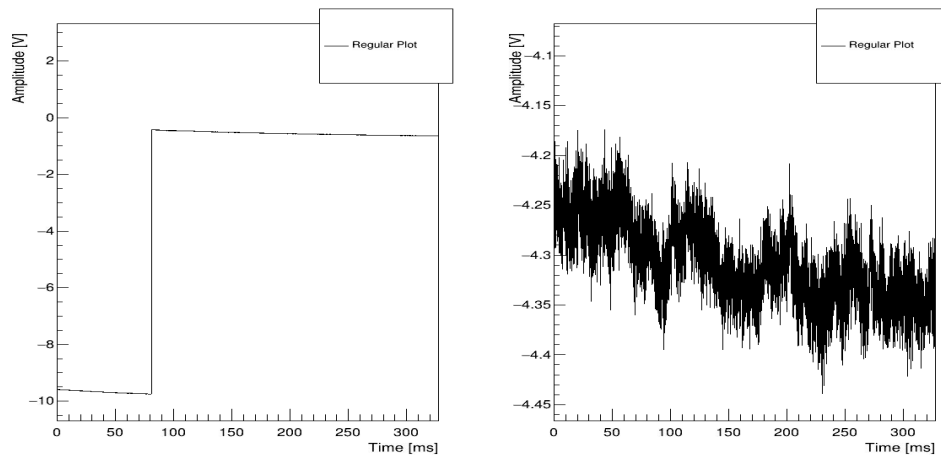


Figure 5.37: The phonon (left) and light (right) pulse recorded for an event in region 1.

5.1.5.2 Verena Region 2

The events in this region, as shown for the previous detectors (see Sections 5.1.2.3 and 5.1.4.3), are due to direct hit of the light detector, with no energy deposition in the phonon detector as shown in Figure 5.38

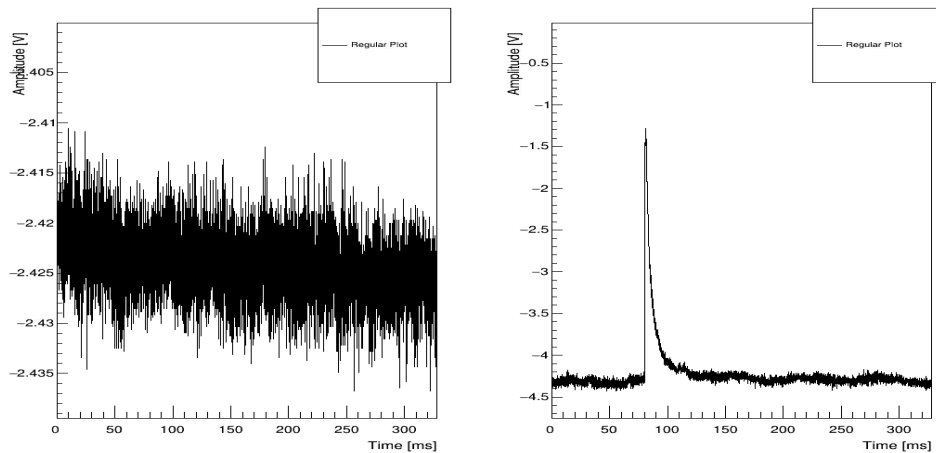


Figure 5.38: The phonon (left) and light (right) pulse recorded for an event in region 2.

5.1.5.3 Verena Region 3

The events in this region for detector Verena are different from similar events in the other detector generated by a SQUID reset. Their distributions in phonon Pulse Height are different, as they do not present small clusters. These events most likely come from α decay from the absorber or light detector surface, where the α goes in the light detector, and the daughter nucleus recoils in the main absorber. One event from this region is shown in Figure 5.39.

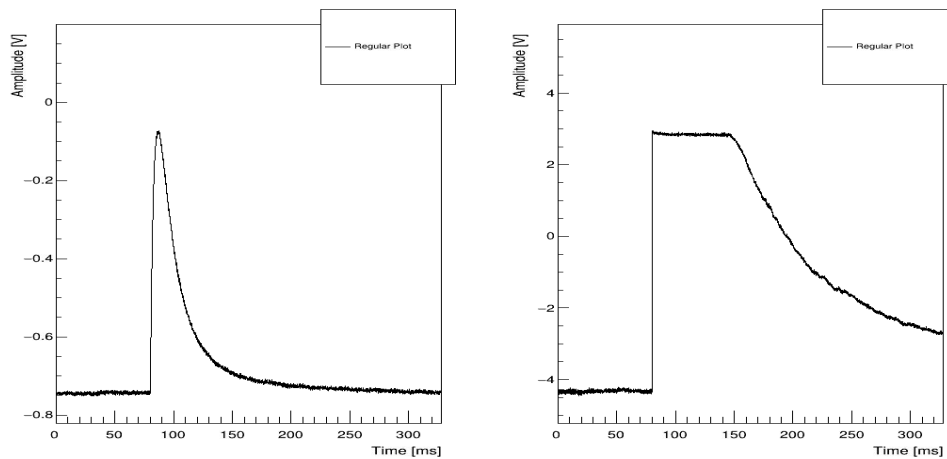


Figure 5.39: The phonon (left) and light (right) pulse recorded for an event in region 3.

5.1.5.4 Verena Region 4

The majority of the events in this region have both the phonon and light pulse evaluated negatively. This problem, as widely described before (see Sections 5.1.1.4, 5.1.3.1 and 5.1.3.2), is generated by a missing pre-trigger fraction in the recorded pulses that generates a wrong computation of the baseline value (larger than the pulse maximum and thus a negative pulse height is obtained). A typical event from this selection is shown in Figure 5.40.

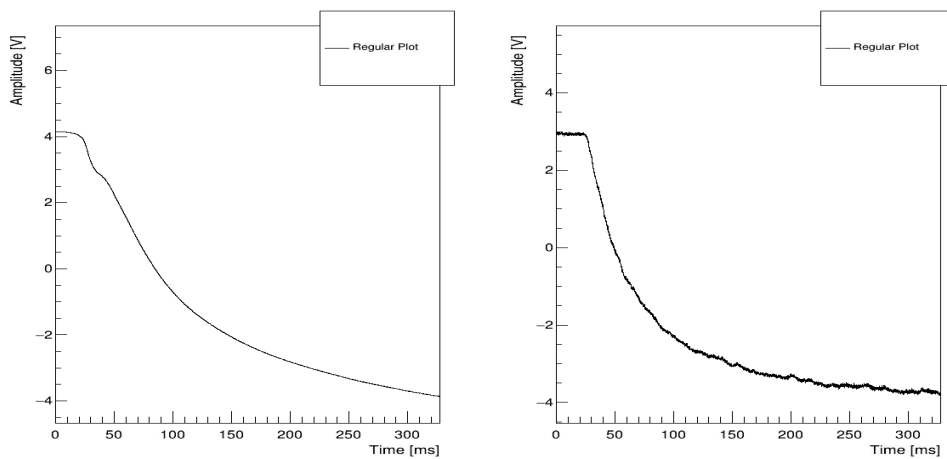


Figure 5.40: The phonon (left) and light (right) pulse recorded for an event in region 4.

5.1.5.5 Verena Region 5

The events in region 5 come from decaying baseline produced by events happening in the time interval in which the trigger was inhibited or from a previous event with a large energy release in the crystal. An event from this selection is shown in Figure 5.41.

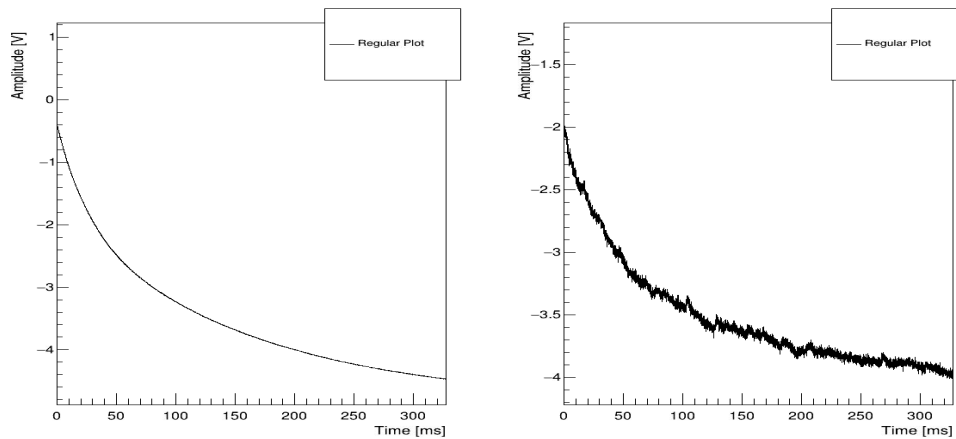


Figure 5.41: The phonon (left) and light (right) pulse recorded for an event in region 5.

5.1.5.6 Verena Region 6

The events from this region present no particular issue, and the resulting fit is reliable. A typical event from this region with the relative fit is shown in Figure 5.42. The cause of these events is the ^{210}Po α decays described in Section 5.1.2.7.

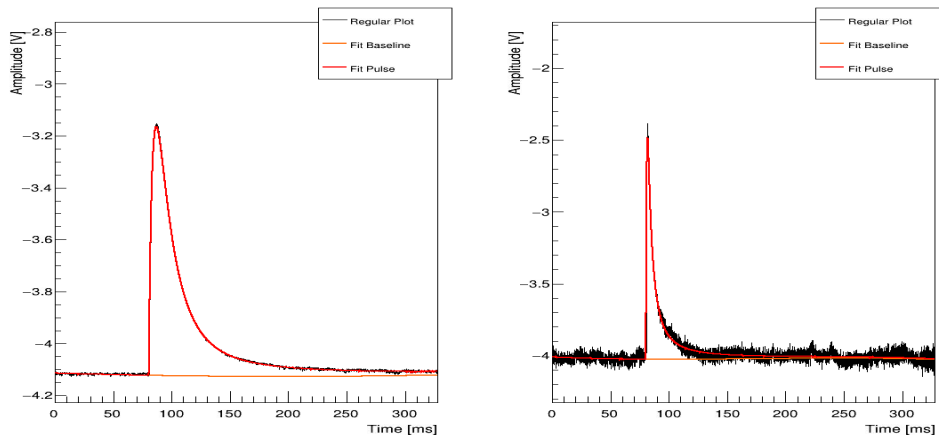


Figure 5.42: The phonon (left) and light (right) pulse recorded with the fit superimposed for an event in the Region 6.

5.1.5.7 Verena Region 7

The events in this region with a *boomerang* shape below the main population come from the anticipated pulse with the peak position before 50 ms (see Figures 5.43). The characteristic *boomerang* shapes comes from the peak position shifting: the shorter is the pre-trigger fraction, the worse is the baseline estimation. Once the pulse rise goes outside the recorded window due to a too short pre-trigger, only the decaying baseline remains in the acquired time window,

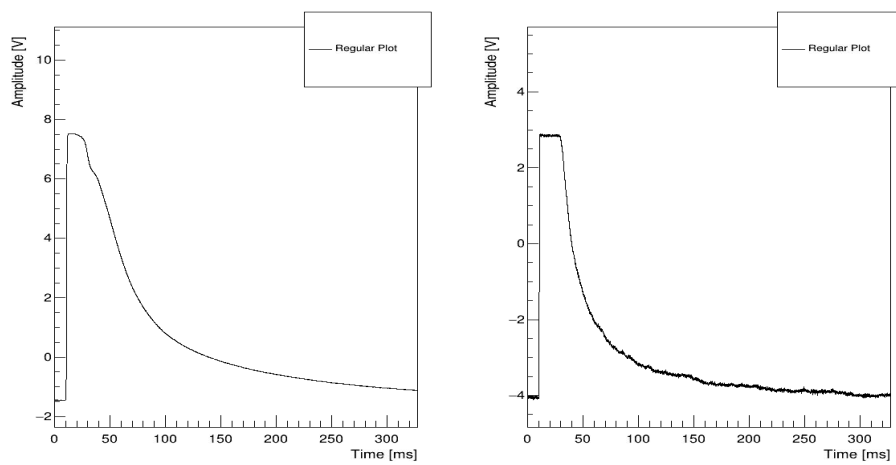


Figure 5.43: The phonon (left) and light (right) pulse recorded for an event in Region 7.

5.2 Detector Response

The energy spectrum and the light-energy distribution associated with each particle type are described in the following subsections. The energy spectrum is modeled, and the bands are parametrized following the standard CRESST approach [99, 103, 105]. The parameters of the resulting functions are determined by fitting the experimental data.

For each particle type, it is easier to model the light vs energy dependence, rather than the light yield vs energy one. For this reason, all the fits are performed in the Light vs Energy plane, Fig. 5.44.

For each detector, the fits are done using the ROMEO software [106] developed in the CRESST Collaboration and, based on the Julia framework[107]. ROMEO is used for both the band fit and the exclusion limit calculation. The software at the moment cannot provide the parameter uncertainties. A study how on systematics affect the limit is presented in Sec. 7.7.1.

5.2.1 Electron/Gamma light mean

The Light Yield is defined as the ratio between the energy deposited in the light channel and the energy deposition in the phonon channel and renormalized to Light Yield equal to 1 for the events at the 122 keV peak of ^{57}Co . Thus the LY for electron recoil follows almost a flat distribution with a mean value ~ 1 .

In a first approximation, the light production for electrons is parameterized linearly as a function of the energy

$$L_e = L_0 E, \quad (5.1)$$

where L_0 represents the proportionality factor between the light produced and the energy, and it is ~ 1 due to the normalization. Keeping into account also the non-linearity effects at higher energy, Equation 5.1 becomes:

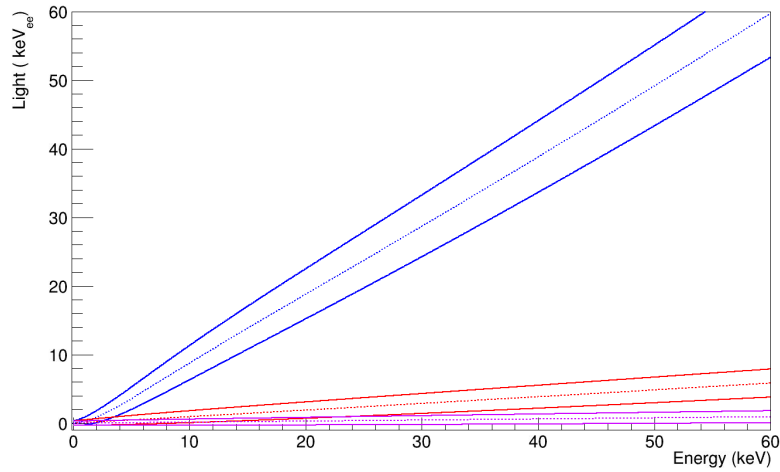
$$L_e = L_0 E + L_1 E^2, \quad (5.2)$$

where L_1 is the non-proportionality term for light production. Finally, the contribution of the non-proportionality effect that bends the electron band towards lower light yields is included in multiplying Eq. 5.2 by an exponential decaying term [105, 108]:

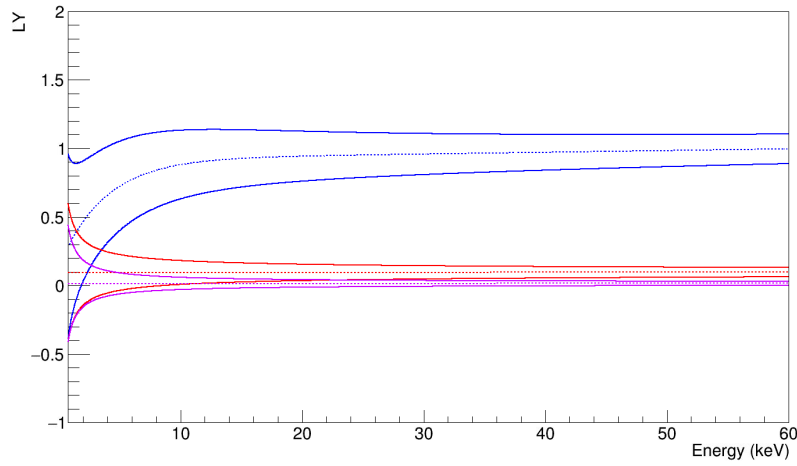
$$L_e = (L_0 E + L_1 E^2) \left[1 - L_2 \exp\left(-\frac{E}{L_3}\right) \right], \quad (5.3)$$

where L_2 is the amplitude of the non-linear effect, and L_3 describes the curvature of the mean line at low energy.

So far, electrons and gammas were treated in the same way, but gammas can release their energy inside the crystal producing multiple secondary electrons. Because of the non-proportionality effect in light production, the sum of the



(a)



(b)

Figure 5.44: The bands corresponding to electron (blue), oxygen (red), and tungsten (violet) recoil events as they appear in the two different planes. The dashed lines correspond to the mean of the bands.

light emitted by many electrons is less than the light produced by a single one with the same total energy. So photons of energy E behave as a single electron with a quenched energy E' . The photon energy quenching is parameterized as:

$$E' = E [Q_{\gamma,1} + E Q_{\gamma,2}], \quad (5.4)$$

where $Q_{\gamma,1}$ and $Q_{\gamma,2}$ describe the linear and non-linear effect of photon energy degradation. The mean photon light is parameterized using the mean electron band evaluated at E' instead of E , obtaining

$$L_{\gamma}(E) = L_e(E') = L_e(E [Q_{\gamma,1} + E Q_{\gamma,2}]) \quad (5.5)$$

The gamma light quenching explains why the gamma peaks in Fig. 4.22(b)

are not centered in the band but have a slightly lower Light Yield compared to the electrons band.

5.2.2 Electron/gamma energy spectrum

A simple linear function describes the electron differential energy spectrum

$$\frac{dN_e}{dE} = P_0 + EP_1, \quad (5.6)$$

where P_0 is the mean electron number for energy unit and P_1 , account for variation from the mean with the energy.

The β spectrum is modeled naively as the convolution of a Gaussian and right triangle starting at E_0 and ending at $E_0 + Q$, where Q is the Q -value

$$\begin{aligned} \frac{dN_{\beta,i}}{dE} &= \\ &= C_{\beta,i} \mathcal{N}(E, \sigma_P(E)) * \frac{2}{E_0 Q} \begin{cases} E_0 - \frac{E_0}{Q}(E - E_0) & \text{if } E_0 < E < E_0 + Q \\ 0 & \text{otherwise.} \end{cases} \end{aligned} \quad (5.7)$$

The coefficients $C_{\beta,i}$ are the counts under the i -th β spectrum, $\mathcal{N}(\mathcal{E}, \sigma_P(\mathcal{E}))$ is a Gaussian with an energy dependent σ as described in Eq 5.12, with an energy dependent σ as described in Eq. 5.12.

Gaussian distribution with an energy dependent σ describes the gamma peak, as described in Eq 5.12 and $C_{\gamma,i}$ accounts for the number of events the i -th peak.

$$\frac{dN_{\gamma,i}}{dE} = \frac{C_{\gamma,i}}{\sqrt{2\pi}\sigma_p(E)} \exp\left(-\frac{(E - E_{\gamma,i})^2}{2\sigma_p^2(E)}\right) \quad (5.8)$$

5.2.3 Nuclear recoil light mean

Nuclear recoil events can be originated from neutrons or dark matter particles interacting in the detector. The light produced in a nuclear recoil is less than that of electrons with the same energy, and the amount of scintillation lights depends on the nucleus involved. The description of the nuclear recoil mean light and a precise measurement of the Quenching Factor and other relevant parameters were studied in a previous works by Strauss [93] and can be described by the formula :

$$L_x = (L_0E + L_1E^2) QF_X \left[1 + f_X \exp\left(-\frac{E}{\lambda_X}\right) \right], \quad (5.9)$$

where the X denotes the nucleus under examination. The energy dependence for electrons is described, with f_X accounting for the strength of energy dependence and λ_X for the light bending. The values obtained for the elements composing CaWO_4 crystals are shown in Table 5.2.

Nucleus	QF_x	f_x	λ_x
O	0.07908 ± 0.00002	0.7088 ± 0.0008	567.1 ± 0.9
Ca	0.05949 ± 0.0078	0.1887 ± 0.0022	802 ± 19
W	0.0196 ± 0.0022	0	∞

Table 5.2: Quenching factor for the relevant elements for CRESST crystals.

Substituting $QF_X \rightarrow \epsilon QF_X$ in Eq. 5.9, the quenching parameters of nuclear recoil bands become the same of Table 5.2 for each detector, and the fit of nuclear recoil bands is reduced to evaluate the ϵ factor for each crystal.

5.2.4 Nuclear recoil energy spectrum

The nuclear recoil spectrum is described using the same exponential model as for the analysis of Run 32 data [99]

$$\frac{dN_{n,x}}{dE} = A_{n,x} \exp\left(-\frac{E}{\lambda_{n,x}}\right), \quad (5.10)$$

where $A_{n,x}$ is the amplitude of the neutron energy spectrum for recoils on the nucleus x and $\lambda_{n,x}$ is the energy decay length of the nuclear recoil on the nucleus x . Data obtained with an Americium - Beryllium neutron source are used to populate and characterize the nuclear recoil band for the different elements in CaWO_4 crystals, as shown in Figure 5.45

5.2.5 Band Width

The band width parameterization completes the nuclear recoil description. The band width is dominated by the light detector resolution, with a small contribution from the phonon detector resolution.

The resolution of the light detectors in CRESST is described by three parameters [105]:

- the baseline resolution of the light detector $\sigma_{0,L}$, which exclusively depends on the detector noise condition;
- a Poissonian term S_1 related to the number of produced photons, proportional to the square root of the measured energy;
- a term S_2 related to the location of the light deposition on the detector, which is proportional to the energy measured

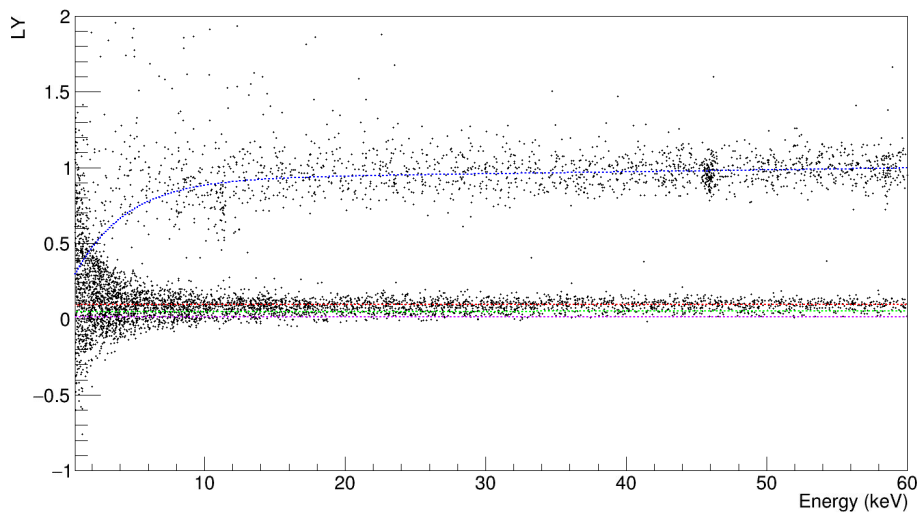


Figure 5.45: Electron and nuclear recoil bands obtained from Am-Be measurement. The mean of the electron band(blue) and the mean of the nuclear recoil for O(red), Ca(green), and W(violet). Neutron calibration data are used for this plot.

The light detector resolution is the squared sum of these three terms:

$$\sigma_L(L) = \sqrt{\sigma_{0,L}^2 + S_1 L + S_2 L^2} \quad (5.11)$$

The energy resolution of the heat (phonon) detector has a similar expression, with the energy proportional term resulting negligible for all the CRESST detector:

$$\sigma_P(E) = \sqrt{\sigma_{0,P}^2 + \sigma_{1,P} E} \quad (5.12)$$

The total energy dependent band width for each event type is determined as :

$$\sigma_{L,X}(E) = \sqrt{\sigma_L(L_X(E)) + \frac{dL_X}{dE}(E)\sigma_P(E)} \quad \text{with } X = e, O, Ca, W, \quad (5.13)$$

where $dL_X/dE(E)$ denote the derivative of light for the event of type X , which is calculated analytically.

Figure 5.46 shows the Light Yield versus Energy plot of Figure 5.45 completed with the band width.

5.2.6 Excess Light

There is an additional class of events, called *excess light event*, presenting a larger Light Yield compared to the electron/gamma event. Most likely, these

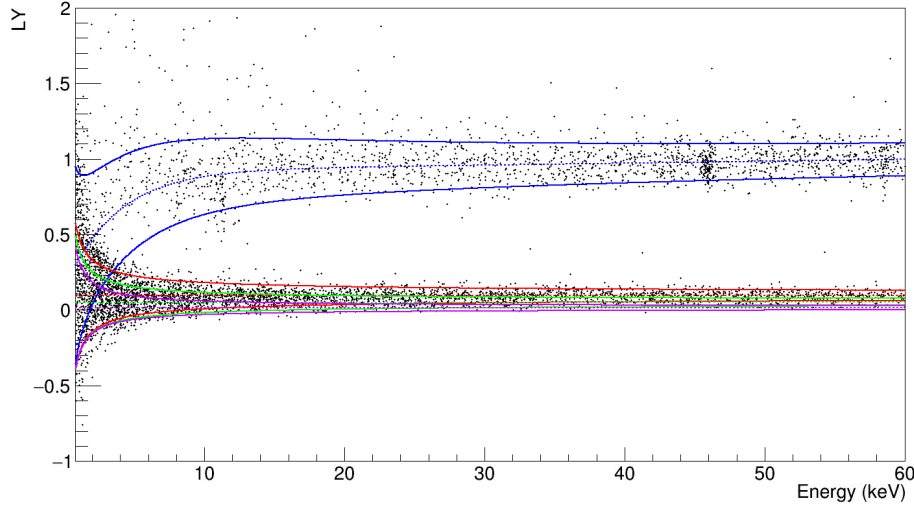


Figure 5.46: The full band description for the electron (blue) and the of the nuclear recoil for O (red), Ca (green), and W (violet) are shown. The dashed lines are the mean, while the solid lines contain 80% of the events of each band. Data from neutron calibration data set

are events happening in the scintillating foil of the crystal [103]. The number of these events decreases at higher energy and light. An empirical description of this event population can be found in [105] and is described by

$$\rho_X(E, L) = \quad (5.14)$$

$$X_{Amp} \exp\left(-\frac{E}{X_{dec}}\right) \left\{ \frac{1}{2X_\lambda} \exp\left(-\frac{L}{X_\lambda} + \frac{\sigma_{L,e}}{2X_\lambda^2}\right) \left[1 + \operatorname{erf}\left(\frac{L}{\sqrt{2}\sigma_{L,e}} - \frac{\sigma_{L,e}}{2X_\lambda}\right) \right] \right\}$$

where X_{Amp} represents the exponential amplitude, X_{dec} the energy decay length, and X_λ the light decay length.

5.3 Energy Spectrum and Light Yield

In this Section, the results obtained on the full dataset are illustrated. For each detector, the energy spectrum with the identified gamma lines as well as the Light Yield vs Energy plot with the result of the band fit are presented. The plots shown in this Section are obtained with the selections described in Chapter 4.

The relevant parameters that will be used for the exclusion analysis of the 5 modules examined are shown in Table 5.3. These parameters are the energy resolution of the phonon ($\sigma_{P,0}$) and light ($\sigma_{L,0}$) channel discussed in Section 5.2.5, the energy threshold used to trigger the data, and measured with the method described in Section 4.4.3, and the total exposure.

Detector	$\sigma_{P,0}$ (keV)	$\sigma_{L,0}$ (keV)	Threshold (keV)	Exposure (kg days)
TUM40	0.0793	0.241	0.8	129.22
Frederika	0.109	0.236	0.759	137.01
Anja	0.126	0.190	1.24	159.13
Verena	0.103	0.281	1.54	164.83
Lise	0.0598	3.23	1	158.67

Table 5.3: Relevant parameters characterizing the detectors included in this analysis. $\sigma_{P,0}$ and $\sigma_{L,0}$ are the resolution at zero energy of the phonon and light channels, respectively.

It is possible to observe how, despite having a similar phonon energy resolution, the threshold of detector Verena is two times larger than the one of Frederika. The threshold of detector Frederika was not optimized during Run 33 since the main focus was the threshold optimization of detectors TUM40 and Lise as they have the best energy resolutions among all the detectors.

The threshold optimization of Lise and TUM40 done during Run 33 made it possible to push the exclusion limit on Dark Matter mass down to $500 \text{ MeV}/c^2$ [101]. On the other hand, the limit at larger mass is limited by the small exposure.

These problems have been solved in the latest CRESST runs (starting from Run 34, details are in [97]), with the introduction of a continuous data taking. It allows to reprocess the full dataset offline with different thresholds.

Since the main purpose of the analysis portrayed in this work is the exclusion of the *islands* of Run 32, the use of the full dataset is mandatory. The choice of the thresholds used in this work for TUM40 and Lise are discussed in the next sections.

Finally, the survival probability of the different cuts for the 5 detectors under investigation is shown in Table 5.4.

Detector	TUM40	Frederika	Anja	Verena	Lise
Stability Cut	0.735(1)	0.804(1)	0.838(1)	0.897(1)	0.902(1)
Coincidence Cut	0.816(1)	0.854(1)	0.882(1)	0.895(1)	0.847(1)
Quality Cut	0.462(2)	0.802(1)	0.535(2)	0.662(1)	0.437(1)
Total	0.277(1)	0.551(1)	0.396(1)	0.532(2)	0.334(1)

Table 5.4: Cut survival probabilities for the detectors included in the analysis.

5.3.1 TUM40

TUM40 is one of the most radio pure detectors of Run 33, as can be seen from the plots in Figures 5.47 and 5.48. With its low threshold of 0.4 keV, TUM40 is considered one of the best detectors of Run 33. As mentioned above, such a threshold was applied only to a dataset fraction, since it was changed during the data taking of Run 33 from 0.6 to 0.4 keV [103].

The lower threshold allowed to achieve a better limit at low mass, but the price to pay was an exposure reduction. For the purpose of this analysis, a larger exposure is most relevant. To profit from the full statistic of this dataset, a high software threshold was applied to the data [100]. Since the campaign for a precise threshold measurement for TUM40 was done only after the threshold change, a new lower limit of the ROI was chosen. A more accurate way to combine the two fractions of the dataset using the Extended Maximum Likelihood is discussed in Section 7.7.

To avoid that events triggered with the 0.4 keV threshold could fluctuate upward and enter the ROI, a threshold value of 0.8 keV has been chosen. Considering that TUM40 energy resolution is 0.079 keV, the new lower limit for the ROI is 5σ above the threshold of 0.4 keV. In this way, no event due to the lower threshold should affect the dataset.

The plots in Figure 5.47 and 5.48 show TUM40 energy spectrum and Light Yield versus Energy scatter plot respectively, done with the new threshold value of 0.8 keV.

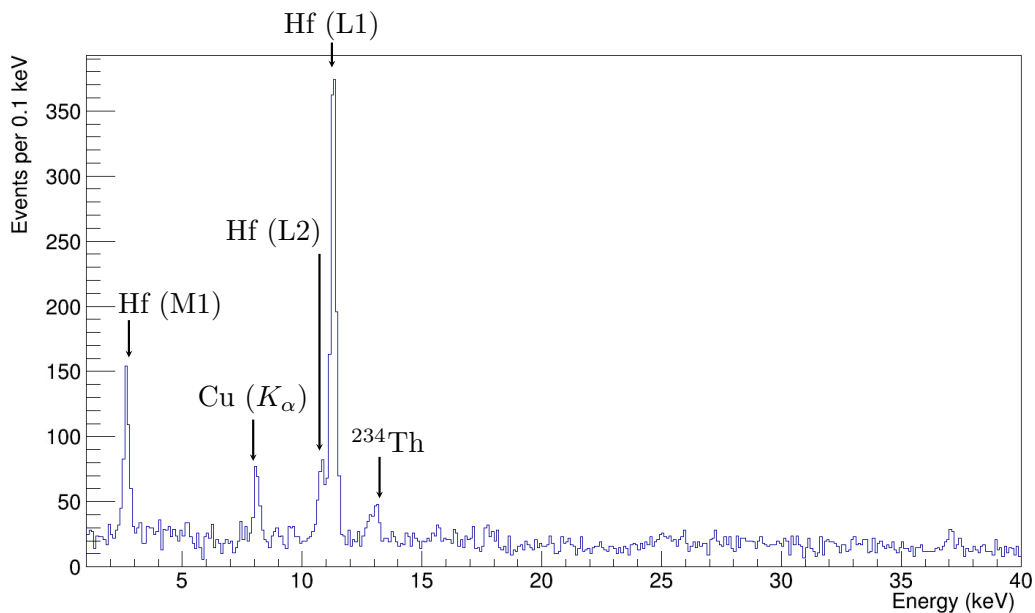


Figure 5.47: TUM40 energy spectrum for the full dataset. In the spectrum are visible the different gamma peaks from the ^{179}Ta electron capture (Eq. 4.5), and the gamma produced by an electron filling the vacancies at L1 (11.27 keV), L2 (10.74 keV), M1 (2.6 keV), the Copper fluorescence a 8 keV, and 13.3 keV X-ray from ^{234}Th .

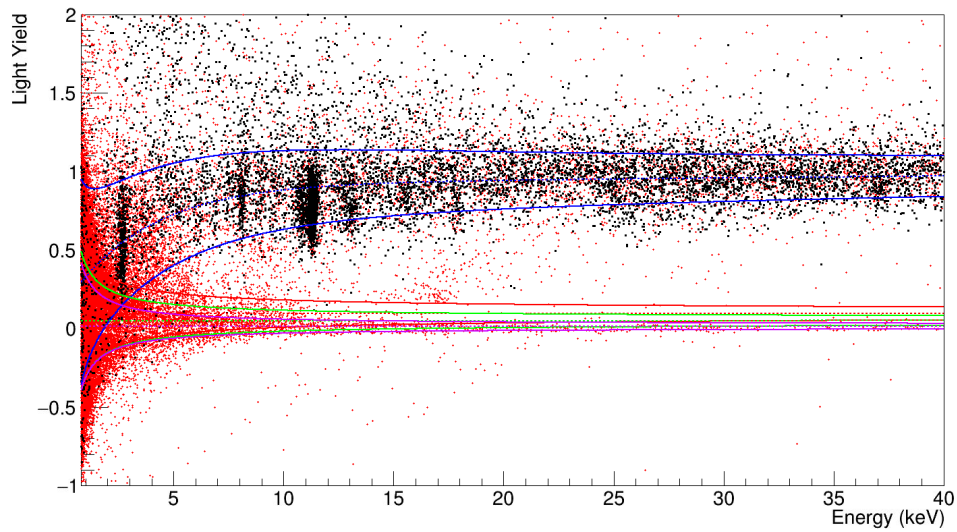


Figure 5.48: TUM40 Light Yield versus Energy scatter plot for the full dataset. In red are shown the events before the selections, while in black the event after the selections. Superimposed on the data, there are the bands for the electron (blue), and the one for nuclear recoil on O (red), Ca (green), and W (violet) are shown. The dashed lines are the mean, while the solid lines contain 80% of the events of each band.

5.3.2 Frederika

Detector Frederika, despite being a detector made by a commercial crystal (not grown from radio-pure selected powders), shows an energy spectrum clean from beta from ^{227}Ac , see Figure 5.50. Two peaks at 5.8 and 6.4 keV dominate the energy spectrum. Such peaks are due to an accidental contamination by a ^{55}Fe source on detector Lise. Such contamination was due to the relative position of detector Frederika with respect detector Lise inside the experimental area (see Figure 5.49). The Light Yield versus Energy plot is shown in Figure 5.51

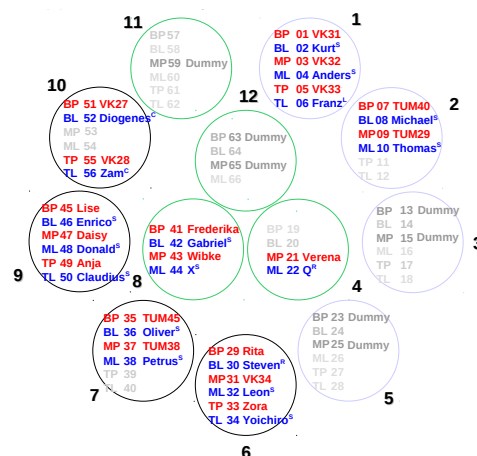


Figure 5.49: Run33 detector position. For each module both the name of the phonon (P) and light (L) detector are shown.

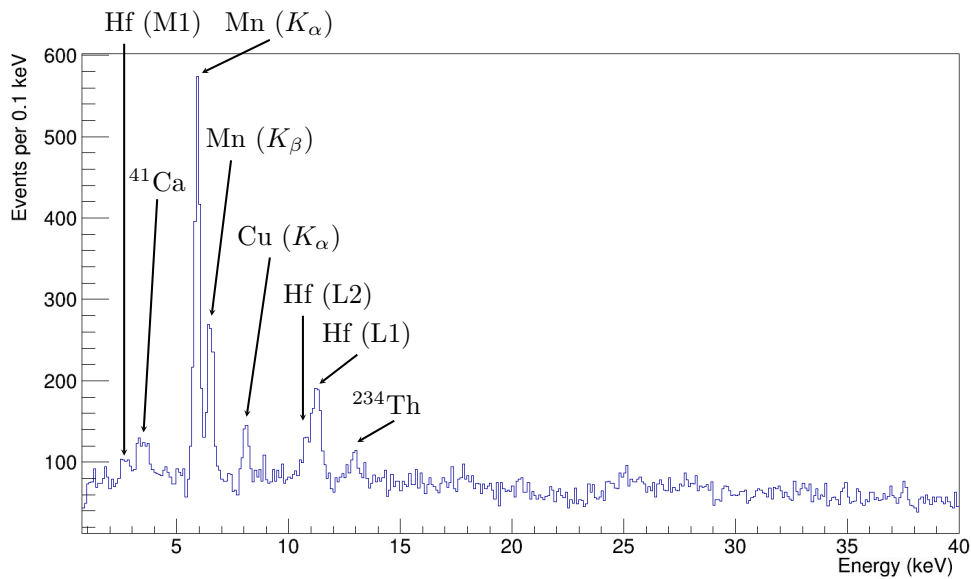


Figure 5.50: Frederika energy spectrum for the full dataset. In the spectrum are visible the different gamma peaks from the ^{179}Ta electron capture (Eq. 4.5), and the gamma produced by an electron filling the vacancies at L1 (11.27 keV), L2 (10.74 keV), M1 (2.6 keV), the Copper fluorescence a 8 keV, a 3.5 keV from ^{41}Ca decay (produced by the $^{40}\text{Ca}(n, \gamma)^{41}\text{Ca}$ reaction), and a 13.3 keV X-ray from ^{234}Th . The lines labeled as manganese escape shell comes from the ^{55}Fe decay. ^{55}Fe decays via electron capture in ^{55}Mn . The vacancy in the K shell left by the nuclear-captured electron is filled by an electron from a higher shell, in the process a X-ray is emitted.

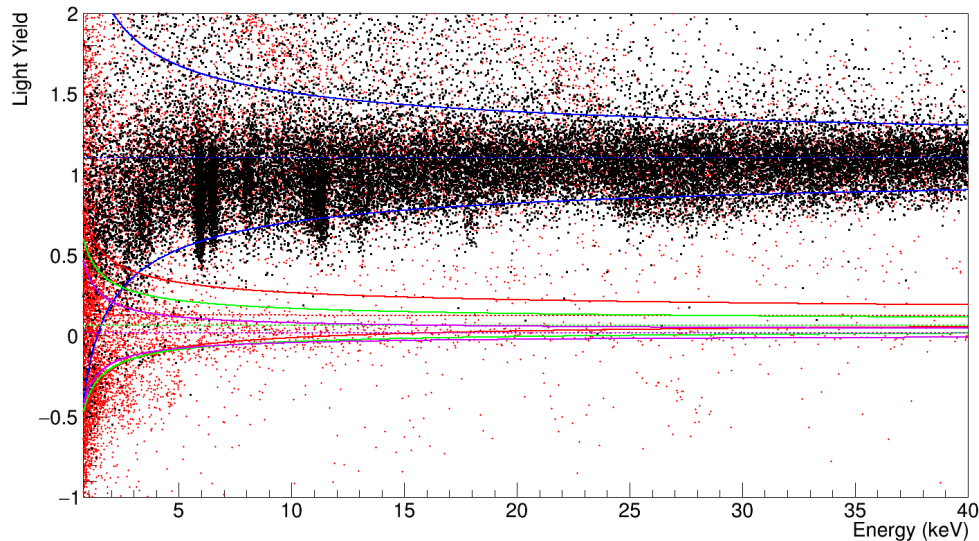


Figure 5.51: Frederika Light Yield versus Energy scatter plot for the full dataset. In red are shown the events before the selections, while in black the event after the selections. Superimposed on the data, there are the bands for the electron (blue), and the one for nuclear recoil on O (red), Ca (green), and W (violet) are shown. The dashed lines are the mean, while the solid lines contain 80% of the events of each band.

5.3.3 Anja

Unlike Fredericka and TUM40 detectors, Anja is dominated by two beta decay spectra ^{227}Ac coming from ^{235}U chain. The contamination The Light Yield versus Energy distribution is shown in Figure 5.53

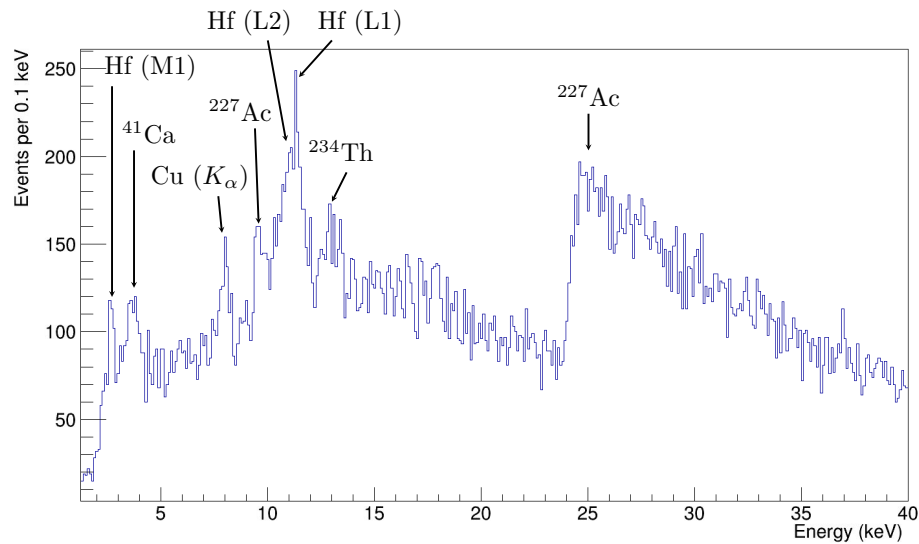


Figure 5.52: Anja energy spectrum. In the spectrum are visible the different gamma peaks from the ^{179}Ta electron capture (Eq. 4.5), and the gamma produced by an electron filling the vacancies at L1 (11.27 keV), L2 (10.74 keV), M1 (2.6 keV), the Copper fluorescence a 8 keV, a 3.5 keV from ^{41}Ca decay (produced by the $^{40}\text{Ca}(n, \gamma)^{41}\text{Ca}$ reaction), and a 13.3 keV X-ray from ^{234}Th . In addition two β spectra from the ^{227}Ac decay are present.

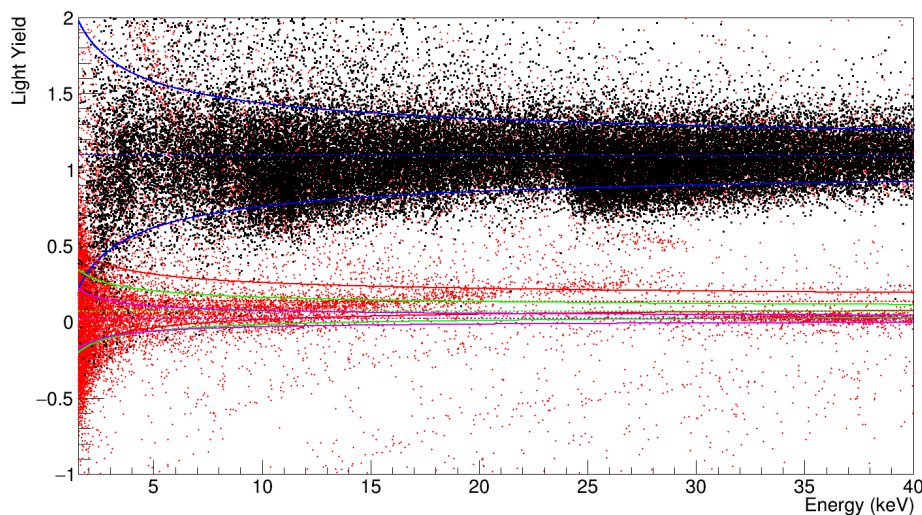


Figure 5.53: Anja Light Yield versus Energy scatter plot for the full dataset. In red are shown the events before the selections, while in black the event after the selections. Superimposed on the data, there are the bands for the electron (blue), and the one for nuclear recoil on O (red), Ca (green), and W (violet) are shown. The dashed lines are the mean, while the solid lines contain 80% of the events of each band.

5.3.4 Verena

The energy spectrum of detector Verena, presented in Figure 5.54, shows β contamination from ^{227}Ac similar to Anja. In addition one can observe a peak at 3.5 keV from ^{41}Ca decay. ^{41}Ca is produced by neutron capture on ^{40}Ca ($^{40}\text{Ca}(n, \gamma)^{41}\text{Ca}$). The Light Yield versus Energy distribution of detector Verena is presented in Figure 5.55.

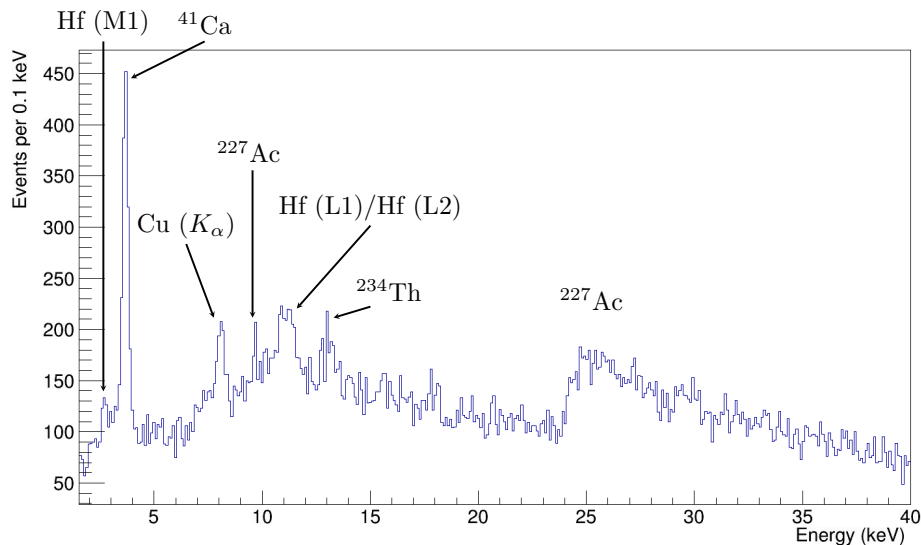


Figure 5.54: Verena energy spectrum for the full dataset. In the spectrum are visible the different gamma peaks from the ^{179}Ta electron capture (Eq. 4.5), and the gamma produced by an electron filling the vacancies at L1 (11.27 keV), L2 (10.74 keV), M1 (2.6 keV), the Copper fluorescence a 8 keV, a 3.5 keV from ^{41}Ca decay (produced by the $^{40}\text{Ca}(n, \gamma)^{41}\text{Ca}$ reaction), and a 13.3 keV X-ray from ^{234}Th . In addition two β spectra from the ^{227}Ac decay are present.

5.3.5 Lise

Similarly to what is discussed for TUM40 in Section 5.3.1, a new threshold has been set for the Lise detector. The threshold of the first fraction of Lise data was very high (~ 900 eV), and a dedicated threshold measurement was never performed. The resulting threshold value of 1 keV corresponds to more than 11σ above the lowest threshold, ensuring that no events triggered with the lower threshold can enter the acceptance region.

From the energy spectrum presented in Figures 5.56 a clear Fe-55 contamination can be appreciated. The presence of Fe-55 comes from an accidental contamination from the sources used to calibrate the CRESST light detector. Due to the huge statistic of the Fe-55 peaks, a zoom of the energy spectrum is presented in Figure 5.57.

From the Light Yield versus Energy plot distribution shown in Figure 5.58 is possible to notice the effect of the poor resolution of the light detector leading to the overlap of the electron/gamma band and nuclear recoil bands up to ~ 15 keV.

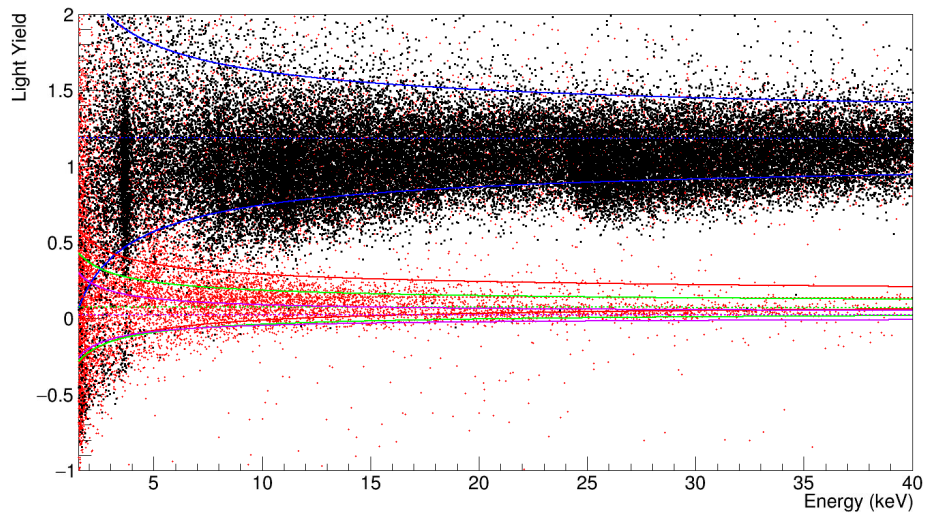


Figure 5.55: Verena Light Yield versus Energy scatter plot for the full dataset. In red are shown the events before the selections, while in black the event after the selections. Superimposed on the data, there are the bands for the electron (blue), and the one for nuclear recoil on O (red), Ca (green), and W (violet) are shown. The dashed lines are the mean, while the solid lines contain 80% of the events of each band.

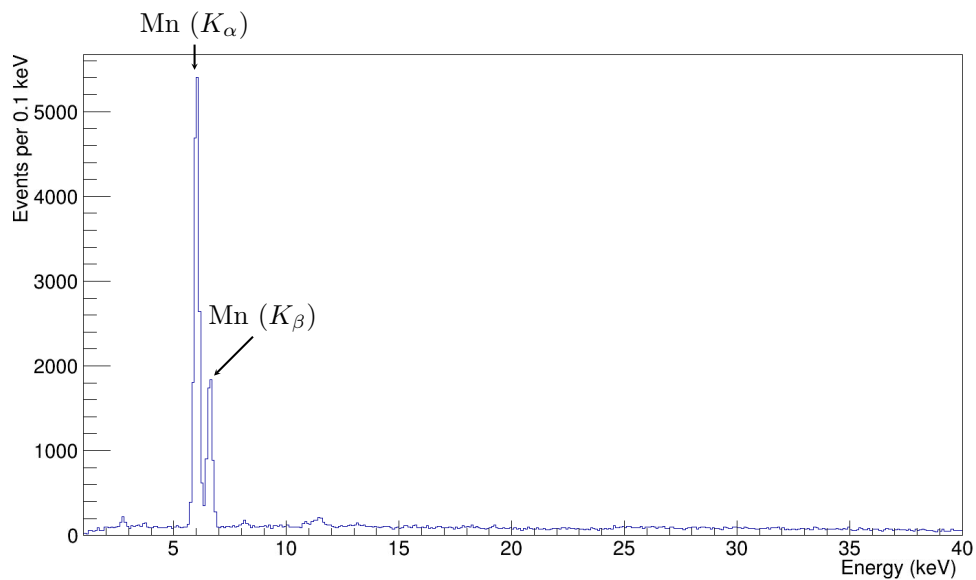


Figure 5.56: Lise energy spectrum for the full dataset. The lines labeled as manganese escape shell comes from the ^{55}Fe decay. ^{55}Fe decays via electron capture in ^{55}Mn . The vacancy in the K shell left by the nuclear-captured electron is filled by an electron from a higher shell, in the process a X-ray is emitted.

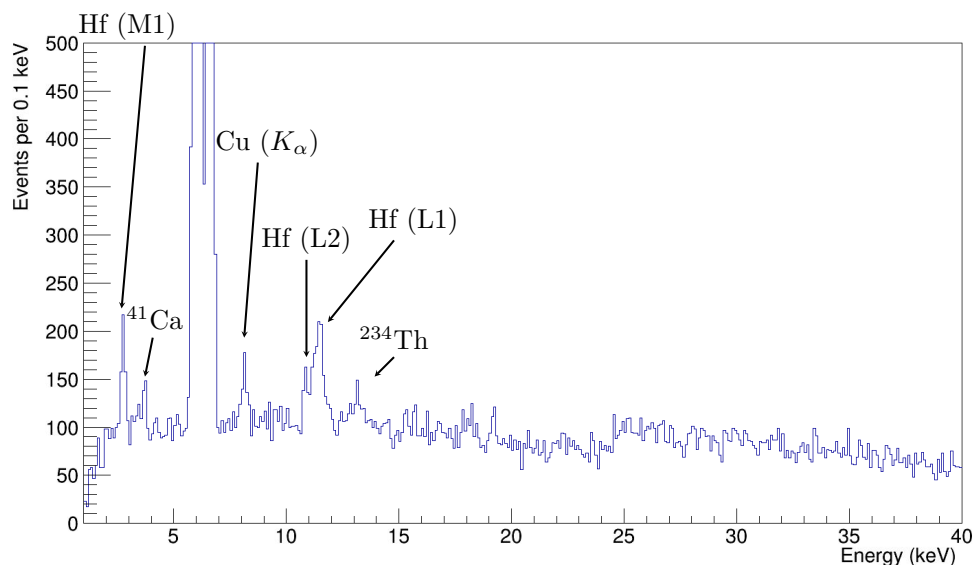


Figure 5.57: Zoom of the Lise energy spectrum in Figure 5.56. In the spectrum are visible the different gamma peaks from the ^{179}Ta electron capture (Eq. 4.5), and the gamma produced by an electron filling the vacancies at L1 (11.27 keV), L2 (10.74 keV), M1 (2.6 keV), the Copper fluorescence a 8 keV, a 3.5 keV from ^{41}Ca decay (produced by the $^{40}\text{Ca}(n, \gamma)^{41}\text{Ca}$ reaction), and a 13.3 keV X-ray from ^{234}Th .

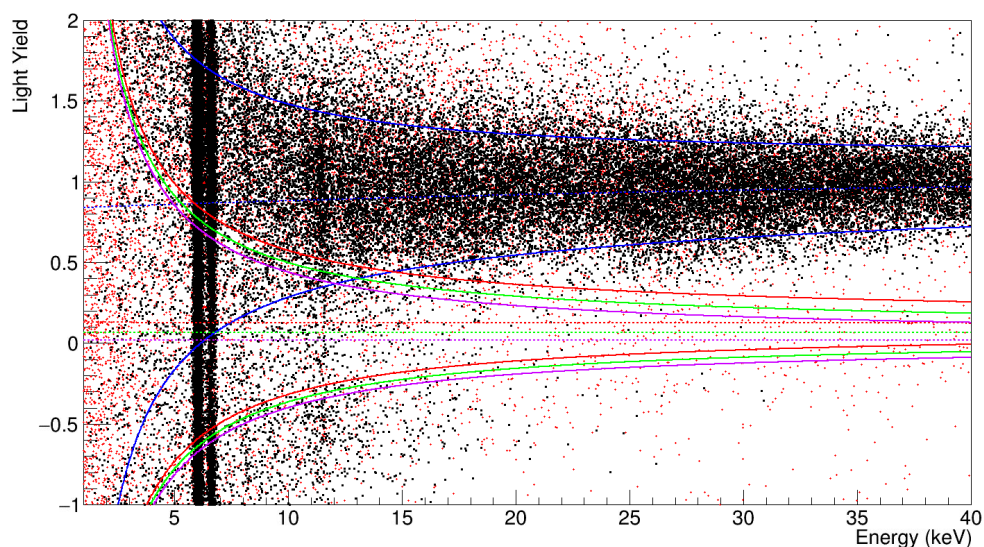
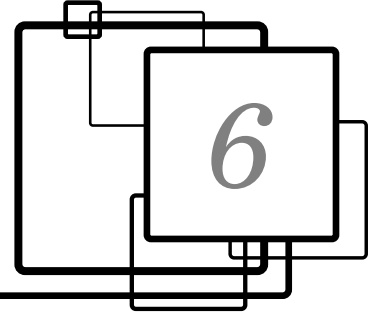


Figure 5.58: Lise Light Yield versus Energy scatter plot for the full dataset. In red are shown the events before the selections, while in black the event after the selections. Superimposed on the data, there are the bands for the electron (blue), and the one for nuclear recoil on O (red), Ca (green), and W (violet) are shown. The dashed lines are the mean, while the solid lines contain 80% of the events of each band.



Maximum Likelihood

This thesis main purpose is to analyse the largest available amount of CRESST data to test the statistical significance of the *islands* illustrated in Chapter 3. An Extended Maximum Likelihood approach has been used to reach this goal, instead of the Yellin method historically used for the CRESST limits computation. The Yellin method is a conservative method to extract Dark Matter limit, as it considers any event in the ROI as a Dark Matter event. In this approach, no background parameterization is included, and thus, no underestimation of unknown background in the data can happen. For this reason, any background over fluctuation results in less stringent limit. There are several reasons to prefer the Likelihood approach instead of the Yellin Optimum Interval method [109]:

- the Yellin optimum interval method is only an exclusion method. It can not be used to claim an excess of signal over background;
- the Yellin optimum interval method is based on the probability of n events occurring *between* two points on a dataset. Since this concept makes sense only in one dimension, it implies using only the phonon channel energy spectrum, neglecting the light channel information¹;
- the Likelihood is naturally suited for a multi-dimensional approach;
- the Likelihood allows the combination of different detectors with different backgrounds and performances-

In this Chapter, the Extended Maximum Likelihood approach is introduced and discussed. Its implementation for the CRESST analysis is described.

6.1 Maximum Likelihood

The maximum likelihood formalism introduced by Fisher [111] is based on the choice of the hypothesis that gives the greatest probability of observed events.

If a variable x (where x can have a dimension >1) is distributed according to a probability density function (*p.d.f.*) $f(x, \theta)$, where θ represents a set of

¹An extension of the Yellin method to multiple dimensions has been proposed in 2007 [110]. The requested computational power and the difficulty in the implementation does not favor such method.

parameters (also of dimension ≥ 1), the probability of experimentally obtaining exactly the dataset x_i given θ is:

$$\mathcal{P}(x_i | \theta) = \prod_i f(x_i | \theta) \quad \text{where } i \text{ runs over the events,} \quad (6.1)$$

The idea of the Likelihood method is to invert the probability. When the measures are taken and θ is unknown, the probability of θ given by x_i is:

$$\mathcal{L}(\theta | x_i) = \prod_i f(x_i | \theta), \quad (6.2)$$

Maximizing the Likelihood means finding the value of θ that maximizes the probability of getting the dataset x_i as the measurement outcome. The negative logarithm of the Likelihood is often used

$$-\log \mathcal{L}(\theta | x_i) = -\sum f(x_i | \theta), \quad (6.3)$$

6.1.1 Extended Maximum Likelihood

In 1990 Barlow [112] extended the Maximum Likelihood concept. The new Extended Maximum Likelihood approach is based on non-normalized density function $\rho(x_i | \theta)$, and includes the number of expected events ν as a new parameter of the Likelihood.

And Eq. 6.2 is modified in:

$$\mathcal{L}(\theta | x_i) = e^{-\nu} \prod_i \rho(x_i | \theta), \quad (6.4)$$

and consequently

$$-\log \mathcal{L}(\theta | x_i) = -\sum \rho(x_i | \theta) + \nu. \quad (6.5)$$

Since x_i can be a vector, it is possible to build a density function $\rho(\{E_i, L_i\} | \theta)$ describing the data in the Light vs Energy plane, and use the phonon and light information for the limit calculation.

6.1.2 Exclusion Limit with Profiled Likelihood Ratio

Since 2011, starting with the XENON100 experiment [113], the use of profile likelihood ratio became a common practice in direct Dark Matter search.

The Profile Likelihood Ratio is defined as :

$$\lambda(\chi) = \frac{\mathcal{L}(\sigma_{\chi,excl}, \hat{\theta} | x_i, m_{\chi})}{\mathcal{L}(\hat{\sigma}_{\chi}, \hat{\theta} | x_i, m_{\chi})}, \quad (6.6)$$

where $\hat{\sigma}_\chi$, and $\hat{\theta}$ are the parameters which maximize the Likelihood for the given data x_i and a specific mass m_χ , while the parameter $\hat{\hat{\theta}}$ are the ones which maximize the Likelihood for a fixed cross section $\sigma_{\chi,excl}$. The $\hat{\sigma}_\chi$ is the parameter of interest, while θ includes all the nuisance parameters, not relevant for the Dark Matter search.

The likelihood is profiled varying the value of $\sigma_{\chi,excl}$. The definition of a test statistic q_σ reduces the observed data to one parameter only.

Since, the purpose of this work is calculating a one sided upper bound the test statistic q_σ is defined as:

$$q_\sigma = \begin{cases} -2 \ln \lambda(\sigma_{\chi,excl}, m_\chi) & \sigma_{\chi,excl} \geq \hat{\sigma}_\chi \\ 0 & \sigma_{\chi,excl} < \hat{\sigma}_\chi \end{cases} \quad (6.7)$$

Let $f(q_\sigma | H_\sigma)$ be the probability distribution of the test statistic q_σ under the signal hypothesis H_σ and let q_σ^{obs} be the value of the test statistic obtained with the observed data. The signal p -value p_s , is the probability that the outcome of a hypothetical, random experiment results in a test statistic larger than the observed one, when the hypothesis H_σ is true. Therefore, p_s is given by

$$p_s = \int_{q_\sigma^{\text{obs}}}^{\infty} f(q_\sigma | H_\sigma) dq_\sigma. \quad (6.8)$$

The signal hypothesis H_σ is rejected at 90% CL if $p_s \leq 10\%$. The Wilks' theorem [114] states that q_σ follows a χ^2 distribution in the limit of a large number of observations. Using the χ^2 approximation and fixing $p_s = 10\%$ it is possible to invert Eq. 6.8 and found the value of λ corresponding to a $\sigma_{\chi,excl}$ that is excluded with a 90% CL . The choice of a 90% CL exclusion limit is a standard practice in exclusion of analysis.

6.2 Density functions

Using the energy spectrum and the light response described in Section 5.2 it is possible to define in the Light - Energy plane the following density functions:

$$\rho_x(E, L) = \frac{dN_x/dE}{\sqrt{2\pi}\sigma_{L,x}(E)} \underbrace{\exp\left\{-\frac{[L - L_{L,x}(E)]^2}{2\sigma_{L,x}^2(E)}\right\}}_{\text{Gaussian in the } L \text{ direction}}. \quad (6.9)$$

that will be used to build the Profile Likelihood Ratio. The Dark Matter density function is defined using the nuclear recoil band multiplied for the energy spectrum of Eq. 2.7 weighted with the detector efficiency and convoluted with the detector energy resolution.

The data of the training set are fit together with the ones from neutron calibration. In this way the fit convergence can benefit from the higher statistics in

both the electron/gamma and the nuclear recoil bands. For the physics data the total density function is given by:

$$\rho_{sum} = \rho_e + \rho_\gamma + \rho_X + \rho_\chi, \quad (6.10)$$

where ρ_e and ρ_γ denote the density functions of electron and gamma respectively, ρ_X corresponds to the excess light events distribution and ρ_χ is the density function for dark matter nuclear recoils given by the sum over the three different species present in the CaWO_4 crystals. The total density function for neutron calibration is :

$$\rho_{ncal} = \rho_e + \rho_\gamma + \rho_X + \rho_{nc}, \quad (6.11)$$

in which ρ_{nc} considers neutrons from the AmBe source.

6.2.1 CRESST Likelihood description

For each CRESST detector the Likelihood function has been defined as:

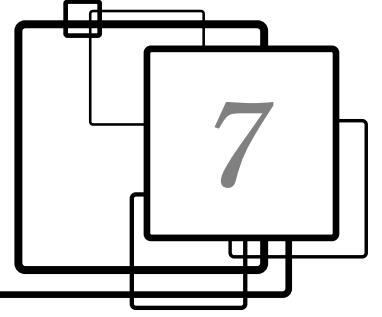
$$\mathcal{L}(\sigma, \theta|x) = e^{-\mathcal{N}_{tot}} \prod_i^N \epsilon \rho(x_i | \sigma, \theta), \quad (6.12)$$

where ρ is the density function defined in Eq. 6.10, \mathcal{N}_{tot} is the total number of expected event, and ϵ is the efficiency computed with the method described in 4.4.2.

The signal component is given by ρ_χ , while the background component is given by electron and gamma leakages in the nuclear recoil band, σ is the Dark Matter cross section used to profile the Likelihood, and θ includes the nuisance parameters describing the electron and gamma event numbers. The parameters describing the band shapes are fixed to the values determined by the band fit performed on the training set and the neutron calibration data. Any residual background event can increase the uncertainties of nuisance parameters, which are not computed by ROMEO. In Section 7.7.1 I show how a small variation in one of the nuisance parameters do not affect the exclusion limit.

The test statistic used for the limit calculation is the one described in Eq. 6.7 and the confidence level for the exclusion limit has been set to 90%. The 90% value for confidence level is a typical assumption for exclusion limit calculation.

The Likelihood is evaluated on each point of the dataset and its minimization is performed with the already cited ROMEO software using the Nelder-Mead minimization algorithm [115].



Dark Matter results

In this Chapter the computation of the exclusion limit obtained under the most standard assumptions for the galactic dark matter halo [57] and Dark Matter interaction is discussed. The analysis portrayed in this work covers the full analysis of 5 detectors discussed in Chapter 5 for a total exposure of ~ 748 kg day.

The Extended Maximum Likelihood has been performed for each detector individually and combining multiple detectors. All the single exclusion limits plots are compared with CRESST latest results (Run34) [64], the previous results of CRESST Run33 (2015) [100, 101], and the *islands* of CRESST Run32 (2012) [99] discussed in the Section 3.3.

In the final part of this Chapter the Dark Matter exclusion plots are presented and discussed. Possible strategies to improve this results are highlighted in Section 7.7.

7.1 TUM40

Figure 7.1 shows the dark matter exclusion plot for TUM40 obtained using the Profiled Likelihood Ratio described in Chapter 6. Comparing the results of TUM40 published in [100] with the ones obtained in this works (Figure 7.1) it is possible to appreciate the effect of the new threshold and the higher exposure in the exploration of the cross section - mass plane. The lower threshold used in [100] with respect to the one used for this work led to a better limit for the low Dark Matter mass. Above $10 \text{ GeV}/c^2$ the dark matter exclusion limit start to be affected by the increased exposure and the results obtained in this work substantially improves the previous one. This result alone can almost completely rule out the *island*.

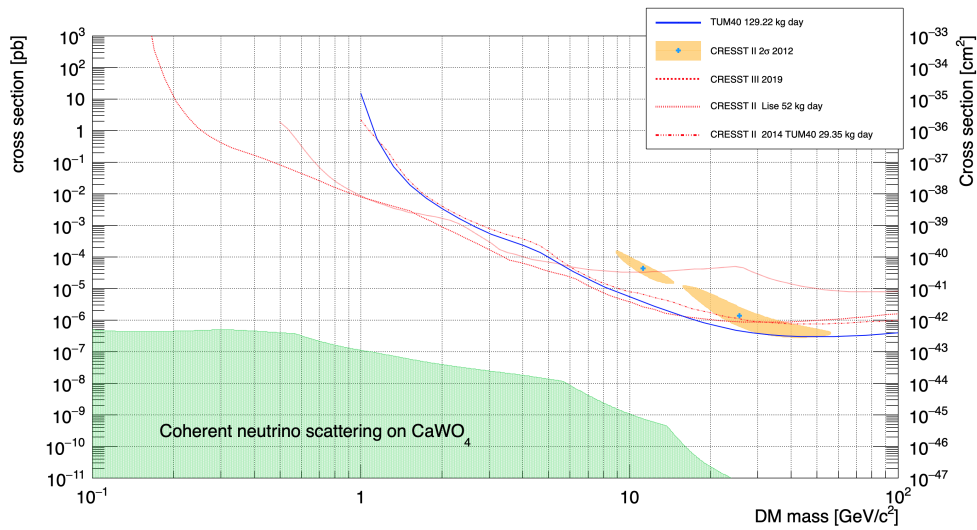


Figure 7.1: The exclusion plot obtained for TUM40 with 129.22 kg days of exposure, compared with the previous CRESST results.

7.2 Frederika

The exclusion limit results obtained for Frederika are presented in Figure 7.2.

Frederika exhibits a better limit than TUM40 up to $m_\chi \sim 15 \text{ GeV}/c^2$ thanks to its lower thresholds (Figure 7.2). For Dark Matter mass larger than $\sim 11 \text{ GeV}/c^2$ TUM40 becomes slightly better than Frederika due to the lower number of event in the nuclear recoil band.

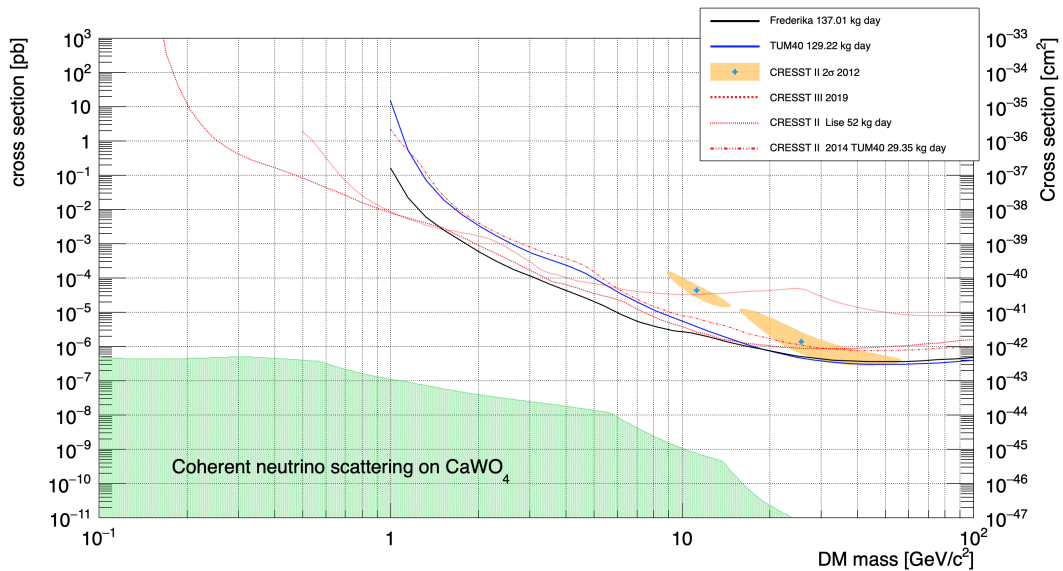


Figure 7.2: The exclusion plot obtained for Frederika with 137.01 for kg days of exposure, compared with the previous CRESST results and the limit of TUM40.

7.3 Anja

The exclusion limit for Anja is presented in Fig. 5.52. At low mass ($m_\chi \lesssim 1.5 \text{ GeV}/c^2$), Anja limit is definitely worse than Frederika and TUM40 due to the high threshold of 1.24 keV. For higher values of Dark Matter mass, from ~ 2 up to $\sim 20 \text{ GeV}/c^2$, a good exclusion limit is achieved by Anja detector for two main reasons: the electron and nuclear recoil bands are well separated above threshold and very few events are present in the nuclear recoil band from threshold up to 10 keV.

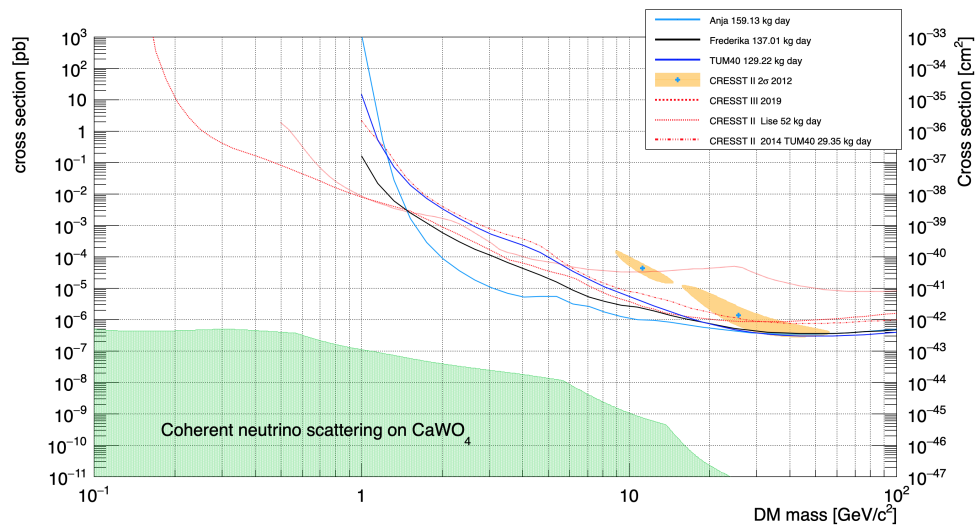


Figure 7.3: The exclusion plot obtained for Anja with 159.14 kg days of exposure, compared with the previous CRESST results and the limits for TUM40 and Anja.

7.4 Verena

The exclusion limit for Verena is shown in Fig. 5.55. Due to its contamination (Fig. 5.54) and to the 1.51 keV threshold, Verena limit is worse than the one of Anja up to $\sim 4 \text{ GeV}/c^2$. For Dark Matter mass larger than $4 \text{ GeV}/c^2$ Verena achieve better results with respect to Anja, because of its smaller ^{227}Ac contaminations and its slightly larger exposure.

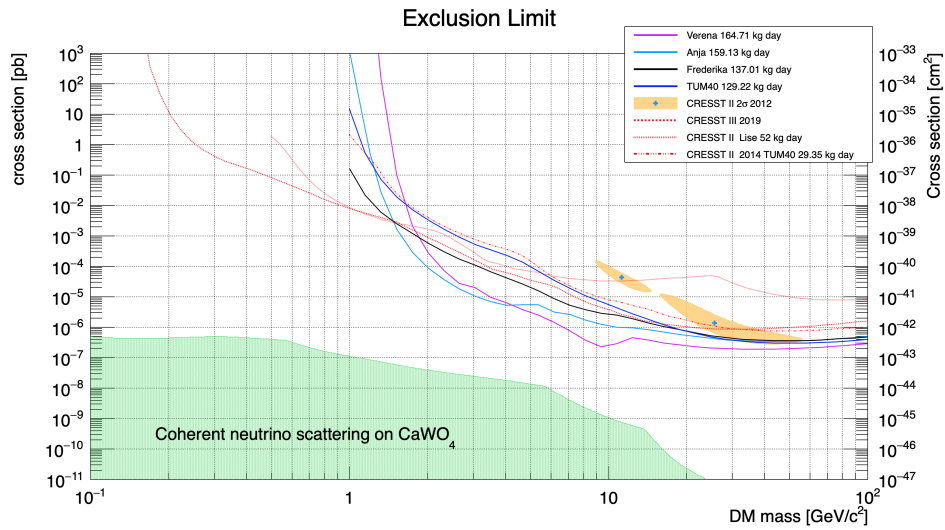


Figure 7.4: The exclusion plot obtained for Verena with 167.41 kg days of exposure, compared with the previous CRESST results and the limits for TUM40, Frederika and Anja.

7.5 Lise

Detector Lise was used to extract the limit presented in [101], thanks to its extremely low threshold ~ 300 eV. As in the case of TUM40, I want compare the limit obtained for Lise in this work with the published one. As discussed for TUM40, a more accurate combination method for the two data fraction is possible using Extended Maximum Likelihood as discussed in Section 7.7.

Despite this effect the exclusion limit obtained with Lise detector outperforms the limits realised with the other 4 detectors, as shown in Figure 7.6.

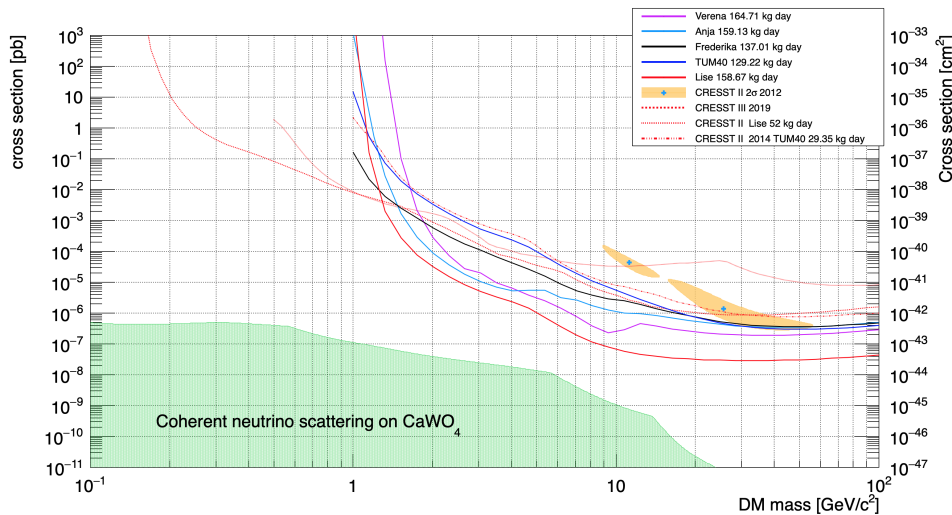


Figure 7.5: The exclusion plot obtained for Lise with 158.67 kg days of exposure, compared with the previous CRESST results and the limits for TUM40, Frederika, Anja and Verena.

7.6 Combined limit

Combining the data of Run 33 collected with the 5 detectors presented in Chapter 5 is crucial to obtain a definitive test of the islands in the region of mass dominated by the exposure. I do this using a global Likelihood that is defined as the product of the single detector Likelihood (see Eq. 6.12):

$$\mathcal{L}_{\text{tot}}^{\text{ext}}(\sigma, \theta | x) = e^{-\mathcal{N}_{\text{tot}}} \prod_d \left[\prod_i^{\mathcal{N}_D} \epsilon_d \rho_d(x_i | \sigma, \theta) \right], \quad (7.1)$$

where D is the number of detectors included in the global Likelihood.

Applying the procedure described in Section 6.1.2 to the global Likelihood in Eq. 7.1 it is possible to compute the combined exclusion limit. As described in Section 6.2.1 the likelihood minimization has been performed with the Nelder-Mead algorithm, evaluating the likelihood point by point. The presence of detector residual backgrounds can slightly modify the nuisance parameters. The small variations in the nuisance parameter do not affect the limit as shown in Sec. 7.7.1.

The exclusion limit obtained is shown in solid black in Figure 7.6. With a total exposure of 748.86 kg days, such result is overall better than the one obtained in 2014 [100] and is the best CRESST result for Dark Matter mass above 1.4 GeV/ c^2 . In the region between 1.4 and 10 GeV/ c^2 the combination of different detectors is very effective, pushing the CRESST exclusion limits $10^{-5} \div 10^{-6}$ pb in cross section region where it is competitive with the Dark Side low mass binomial limit [116]. In the Dark Matter mass region above 10 GeV/ c^2 the combined limit fully excludes the CRESST islands from 2012 [99].

This result is very important as it solves the long standing open issue concerning the excesses observed by CRESST in 2012.

An additional remark on the exclusion of the islands needs to be done. The results obtained in [99] were already excluded by other experiments by several orders of magnitude [67, 65]. These results were already conclusive regarding the most simple scenario for Dark Matter halo and interaction. Nonetheless many properties of the halo and the interactions are still experimentally unconstrained. For these reasons excluding any possible anomaly in the Dark Matter scenario gives a relevant contribution to establish a complete picture. With the result of this work the presence of an exotic interaction of Dark Matter in CaWO₄ crystal has been excluded to the level of 10^{-6} pb.

The limit obtained in this work confirms that the choice of CRESST of moving to fully scintillating housing was crucial to reject not yet fully modeled sources of background. The CRESST setups built after 2013 (from CRESST Run 33 on) continuously improved the concept of fully active/fully scintillating housing and since then no further evidences of relevant excess of events in the ROI has been observed.

It has to be noticed that in the region above 10 GeV/ c^2 the combination of the 5 detectors produces a limit which is worse than the result obtained with

Lise alone. This comes from the fact that the combination of detectors with very different contaminations and limits have to take in account the different populations and effects present in the spectra. For example, the Lise detector spectrum is well fitted in terms of known backgrounds and the presence of an eventual Dark Matter signal can be at maximum of the order of the background fluctuations. On the contrary TUM40 detector is extremely clean and the presence of signals in the dark band is necessarily associated in the Likelihood to Dark Matter events, affecting the exclusion limit. Combining Lise and TUM40 detectors leads to a combined limit dominated by the detector with the highest Dark Matter contribution.

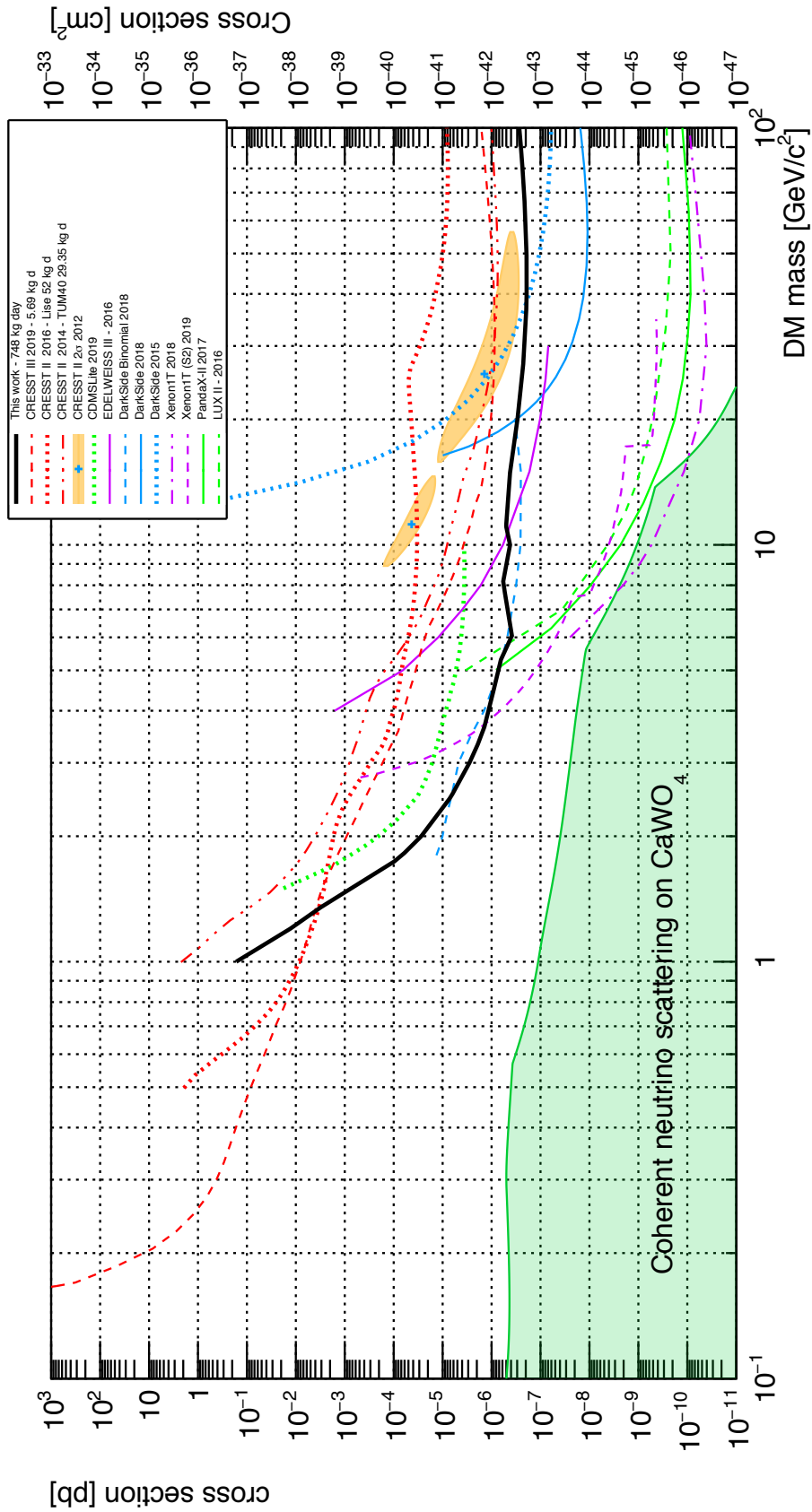


Figure 7.6: In Figure is presented the limit obtained in this work (solid black), together with the previous limit of CRESST: CRESST III - 2019 [64] (dashed red), CRESST II - 2016 [101] (dotted red), CRESST II - 2014 [100] (dash-dotted red), the islands found in CRESST II - 2012 [99] (orange filled with cyan cross). And the result of CDMSLite - 2019 [62] (dotted green), EDELWEISS III - 2016 [63] (solid violet), DarkSide Binomial analysis - 2018 [116] (dashed azure), DarkSide50 - 2018 [68] (solid azure), DarkSide50 - 2015 [117] (dotted azure), Xenon1T - 2018 [67] (dot dashed violet), Xenon1T S2 only - 2019 [118] (dashed violet), PandaX II 2017 [66] (solid green), LUX II [65] (dashed green).

7.7 Conclusions and outlook

As discussed in Sec 7.6 in this work combining the data of 5 modules from CRESST Run 33 detectors for a total exposure of 748.86 kg days, two main results were achieved: the complete exclusion of the islands due to an excess event from CRESST Run 32 and the best CRESST exclusion result for mass above 1.4 GeV/c^2 . The latter is competitive or better with the best limits in the field up to 4 GeV/c^2 .

Moreover this work opens the way to many possible different studies to improve the analysis of Run 33, increasing the sensitivity and improving the exclusion limits. The main developments that were suggested by this work can be summarised in: improving the exposure adding more detectors, improving the background reconstruction in the band fit, and developing a more accurate summing method for the two dataset fractions of Lise and TUM40 detectors.

The 5 detectors used for this analysis are a subset of the 12 working detectors measured in Run 33. Of the remaining detectors few others can be included in a future analysis improving the model of the bands. This will require a Montecarlo simulation of the electron/gamma contributions to better identify the different components. In this way it is possible to expect a final total expose of the order of 1.4 tonnes day.

The reconstruction of the beta and gamma components of the spectrum is done with a simplified model. A more accurate fit of the background, including full beta spectrum description and more accurate gamma modelling will produce a more robust band fitting, possibly improving the likelihood effectiveness.

As can be sen from Figure 7.6 the limit obtained in this work becomes less and less competitive, with respect to [101], below 1.4 GeV/c^2 . This is due to the fact that the 2 subsets of Lise and of TUM40 were combined using a higher *common* threshold. For this reasons the limit looses the sensitivity to the mass region between 0.5 and 1.4 GeV/c^2 . This effect can possibly be limited using a more robust approach to combine the two fractions of the dataset for Lise and TUM40. This can be obtained considering the two fractions as two independents detectors with different thresholds and combining them with an Extended Maximum Likelihood fit.

7.7.1 Study of Systematics

The software I used to compute the exclusion limits cannot quantify parameter uncertainties. So, it is not possible to know how systematics affect the limits. For this reason, I started a campaign to reevaluate exclusion limits modifying the parameter L_0 . This parameter accounts for the position along the y axis of the electrons and nuclear recoil bands, and it is the primary source for systematics. I computed two new limits for TUM40, increasing and decreasing the L_0 value by the 5%. The results obtained are presented in Figure 7.7.

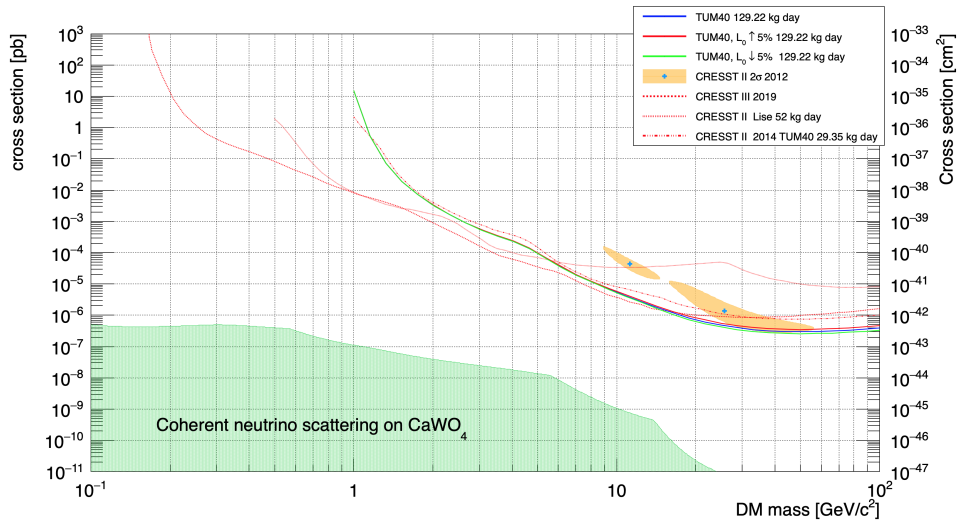


Figure 7.7: The limit of TUM40 presented in this work (solid blue) is compared with the limits obtained changing the parameter L_0 .

The limits obtained with the modified parameter differ from the limit presented in Figure 7.1 for at maximum the 7%. To obtain a complete and accurate analysis, this study of the systematics must be extended to the limits of the other detectors and the combined limit. A paper reporting all the analysis and the results presented in this work is in preparation, and it will also include the complete study of the systematics.

Bibliography

- [1] Thomson, Baron Kelvin, William. *Baltimore Lectures on Molecular Dynamics and the Wave Theory of Light*. Cambridge Library Collection - Physical Sciences. Cambridge University Press, 2010.
- [2] Poincaré, H. The Milky Way and the Theory of Gases. *Popular Astronomy*, 14:475–488, October 1906.
- [3] Bertone, Gianfranco and Hooper, Dan. History of dark matter. *Reviews of Modern Physics*, 90(4), Oct 2018.
- [4] Zwicky, F. Die Rotverschiebung von extragalaktischen Nebeln. *Helvetica Physica Acta*, 6:110–127, Jan 1933.
- [5] Zwicky, F. . Republication of: The redshift of extragalactic nebulae. *General Relativity and Gravitation*, 41(1):207–224, 2009.
- [6] Vera C. Rubin and W. Kent Ford Jr. Rotation of the Andromeda Nebula from a Spectroscopic Survey of Emission Regions. *Astrophys. J.*, 159:379–403, 1970.
- [7] Rubin, Vera C. and Ford, Jr., W. Kent and Thonnard, Norbert. Extended rotation curves of high-luminosity spiral galaxies. IV. Systematic dynamical properties, Sa through Sc. *Astrophys. J.*, 225:L107–L111, 1978.
- [8] Rubin, V. C and Ford, W. K., Jr. and Thonnard, N. Rotational properties of 21 SC galaxies with a large range of luminosities and radii, from NGC 4605 (R=4kpc) to UGC 2885 (R=122kpc). *Astrophys. J.*, 238:471–487, Jun 1980.
- [9] Zwicky, F. On the Masses of Nebulae and of Clusters of Nebulae. *The Astrophysical Journal*, 86:217, October 1937.
- [10] Einstein, Albert. LENS-LIKE ACTION OF A STAR BY THE DEVIATION OF LIGHT IN THE GRAVITATIONAL FIELD. *Science*, 84(2188):506–507, 1936.
- [11] Zwicky, F. On the Probability of Detecting Nebulae Which Act as Gravitational Lenses. *Phys. Rev.*, 51:679–679, Apr 1937.

- [12] Zwicky, F. Nebulae as Gravitational Lenses. *Phys. Rev.*, 51:290–290, Feb 1937.
- [13] Smith, Sinclair. The Mass of the Virgo Cluster. *The Astrophysical Journal*, 83:23, January 1936.
- [14] Massimo Persic, Paolo Salucci, and Fulvio Stel. The Universal rotation curve of spiral galaxies: 1. The Dark matter connection. *Mon. Not. Roy. Astron. Soc.*, 281:27, 1996.
- [15] Corbelli, E. and Salucci, P. The extended rotation curve and the dark matter halo of M33. *Monthly Notices of the Royal Astronomical Society*, 311(2):441–447, Jan 2000.
- [16] Douglas Clowe and Maruša Bradač and Anthony H. Gonzalez and Maxim Markevitch and Scott W. Randall and Christine Jones and Dennis Zaritsky. A Direct Empirical Proof of the Existence of Dark Matter. *The Astrophysical Journal*, 648(2):L109–L113, aug 2006.
- [17] Kochanek and *et al.* Clusters of Galaxies in the Local Universe. *The Astrophysical Journal*, 585(1):161–181, March 2003.
- [18] A. Vikhlinin and *et al.* Chandra Sample of Nearby Relaxed Galaxy Clusters: Mass, Gas Fraction, and Mass-Temperature Relation. *The Astrophysical Journal*, 640(2):691–709, apr 2006.
- [19] Maruša Bradač and Steven W. Allen and Tommaso Treu and Harald Ebeling and Richard Massey and R. Glenn Morris and Anja von der Linden and Douglas Applegate. Revealing the Properties of Dark Matter in the Merging Cluster MACS J0025.4-1222. *The Astrophysical Journal*, 687(2):959–967, nov 2008.
- [20] Clowe, Douglas and Gonzalez, Anthony and Markevitch, Maxim. Weak-Lensing Mass Reconstruction of the Interacting Cluster 1E 0657-558: Direct Evidence for the Existence of Dark Matter. *The Astrophysical Journal*, 604(2):596–603, Apr 2004.
- [21] Markevitch, M. and Gonzalez, A. H. and Clowe, D. and Vikhlinin, A. and Forman, W. and Jones, C. and Murray, S. and Tucker, W. Direct Constraints on the Dark Matter Self-Interaction Cross Section from the Merging Galaxy Cluster 1E 0657-56. *The Astrophysical Journal*, 606(2):819–824, May 2004.
- [22] Famaey, Benoît and McGaugh, Stacy S. Modified Newtonian Dynamics (MOND): Observational Phenomenology and Relativistic Extensions. *Living Reviews in Relativity*, 15(1):10, 2012.
- [23] Peebles, Phillip James Edwin. Discovery of the hot Big Bang: What happened in 1948. *The European Physical Journal H*, 39(2):205–223, 2014.

- [24] Penzias, A. A. and Wilson, R. W. A Measurement of Excess Antenna Temperature at 4080 Mc/s. *The Astrophysical Journal*, 142:419–421, July 1965.
- [25] Dicke, R. H. and Peebles, P. J. E. and Roll, P. G. and Wilkinson", D. T. Cosmic Black-Body Radiation. *The Astrophysical Journal*, 142:414–419, July 1965.
- [26] Fixsen, D. J. THE TEMPERATURE OF THE COSMIC MICROWAVE BACKGROUND. *The Astrophysical Journal*, 707(2):916–920, Nov 2009.
- [27] Bardeen, James M. and Steinhardt, Paul J. and Turner, Michael S. Spontaneous creation of almost scale-free density perturbations in an inflationary universe. *Phys. Rev. D*, 28:679–693, Aug 1983.
- [28] Smoot, G. F. and *et al.* . Structure in the COBE Differential Microwave Radiometer First-Year Maps. *The Astrophysical Journal*, 396:L1, September 1992.
- [29] Hinshaw G. F. *et al.* Nine-year Wilkinson Microwave Anisotropy Probe (WMAP) Observations: Cosmological Results. *The Astrophysical Journal Supplement*, 2012.
- [30] Planck Collaboration and *et al.* Planck 2018 results. I. Overview and the cosmological legacy of Planck. *A&A*, 2019.
- [31] Planck Collaboration. Planck 2018 results. VI. Cosmological parameters. *A&A*, 2020.
- [32] Brian D. Fields and Keith A. Olive. Big Bang nucleosynthesis. *Nuclear Physics A*, 777:208 – 225, 2006. Special Issue on Nuclear Astrophysics.
- [33] Jeans, James Hopwood and Darwin, George Howard . I. The stability of a spherical nebula. *Philosophical Transactions of the Royal Society of London. Series A, Containing Papers of a Mathematical or Physical Character*, 199(312-320):1–53, 1902.
- [34] Springel and *et al.* Simulations of the formation, evolution and clustering of galaxies and quasars. *Nature* , 435(7042):629–636, June 2005.
- [35] Frenk, C.S. and White, S.D.M. Dark matter and cosmic structure. *Annalen der Physik*, 524(9-10):507–534, 2012.
- [36] Ana Bonaca and *et al.* High-resolution Spectroscopy of the GD-1 Stellar Stream Localizes the Perturber near the Orbital Plane of Sagittarius. *The Astrophysical Journal*, 892(2):L37, apr 2020.
- [37] Nilanjan Banik and Jo Bovy and Gianfranco Bertone and Denis Erkal and T. J. L. de Boer. Novel constraints on the particle nature of dark matter from stellar streams, 2019.

- [38] Conrad, Jan and Reimer, Olaf. Indirect dark matter searches in gamma and cosmic rays. *Nature Physics*, 13(3):224–231, 2017.
- [39] Tanabashi M. *et al.* Review of Particle Physics. *Phys. Rev. D*, 98:030001, Aug 2018.
- [40] Boyarsky, A. and Drewes, M. and Lasserre, T. and Mertens, S. and Ruchayskiy, O. Sterile neutrino Dark Matter. *Progress in Particle and Nuclear Physics*, 104:1–45, Jan 2019.
- [41] Edward W. Kolb and Michael S. Turner. *The Early Universe*, volume 69. Avalon Publishing, 1994.
- [42] Kaplan, David E. and Luty, Markus A. and Zurek, Kathryn M. Asymmetric dark matter. *Physical Review D*, 79(11), Jun 2009.
- [43] Jason Kumar. Asymmetric Dark Matter. *AIP Conf. Proc.*, 1604(1):389–396, 2015.
- [44] Peccei, R. D. and Quinn, Helen R. CP Conservation in the Presence of Pseudoparticles. *Phys. Rev. Lett.*, 38:1440–1443, Jun 1977.
- [45] Peccei, R. D. and Quinn, Helen R. Constraints imposed by CP conservation in the presence of pseudoparticles. *Phys. Rev. D*, 16:1791–1797, Sep 1977.
- [46] A. Ringwald. Axions and Axion-Like Particles. In *49th Rencontres de Moriond on Electroweak Interactions and Unified Theories*, pages 223–230, 2014.
- [47] Kim, Jihn E. and Carosi, Gianpaolo. Axions and the strong CP problem. *Rev. Mod. Phys.*, 82:557–601, Mar 2010.
- [48] Boveia, Antonio and Doglioni, Caterina. Dark Matter Searches at Colliders. *Annual Review of Nuclear and Particle Science*, 68(1):429–459, Oct 2018.
- [49] Blennow, M. and Fernandez-Martinez, E. and Olivares-Del Campo, A. and Pascoli, S. and Rosauero-Alcaraz, S. and Titov, A. V. Neutrino portals to dark matter. *The European Physical Journal C*, 79(7):555, 2019.
- [50] Aartsen, M. G. and *et al.* Search for annihilating dark matter in the Sun with 3 years of IceCube data. *The European Physical Journal C*, 77(3):146, 2017.
- [51] Di Mauro, Mattia and Hou, Xian and Eckner, Christopher and Zaharijas, Gabrijela and Charles, Eric. Search for γ -ray emission from dark matter particle interactions from the Andromeda and Triangulum galaxies with the Fermi Large Area Telescope. *Phys. Rev. D*, 99:123027, Jun 2019.

- [52] Fermi-LAT Collaboration. The Fermi Galactic Center GeV Excess and Implications for Dark Matter. *The Astrophysical Journal*, 840(1):43, May 2017.
- [53] Karwin, Christopher and Murgia, Simona and Tait, Tim M. P. and Porter, Troy A. and Tanedo, Philip. Dark matter interpretation of the Fermi-LAT observation toward the Galactic Center. *Physical Review D*, 95(10), May 2017.
- [54] Bennett, C. L., et.al. Nine-year Wilkinson Microwave Anisotropy Probe (WMAP) Observations: Final Maps and Results. *The Astrophysical Journal Supplement*, 2012.
- [55] Heisig, Jan and Cuoco, Alessandro and Korsmeier, Michael and Kraemer, Michael. A combined dark matter study of AMS-02 antiprotons and Fermi-LAT gamma rays. *Proceedings of The European Physical Society Conference on High Energy Physics — PoS(EPS-HEP2017)*, Oct 2017.
- [56] Chang, J. *et al.* The DARK Matter Particle Explorer mission. *Astroparticle Physics*, 95:6–24, Oct 2017.
- [57] Gunn, James E. and Gott, J. Richard, III. On the Infall of Matter Into Clusters of Galaxies and Some Effects on Their Evolution. *The Astrophysical Journal*, 176:1, August 1972.
- [58] J.D. Lewin and P.F. Smith. Review of mathematics, numerical factors, and corrections for dark matter experiments based on elastic nuclear recoil. *Astroparticle Physics*, 6(1):87 – 112, 1996.
- [59] F. Donato, N. Fornengo, and S. Scopel. Effects of galactic dark halo rotation on wimp direct detection. *Astroparticle Physics*, 9(3):247 – 260, 1998.
- [60] Freese, K. Review of Observational Evidence for Dark Matter in the Universe and in upcoming searches for Dark Stars. *EAS Publications Series*, 36:113–126, 2009.
- [61] Helm, Richard H. Inelastic and Elastic Scattering of 187-Mev Electrons from Selected Even-Even Nuclei. *Phys. Rev.*, 104:1466–1475, Dec 1956.
- [62] Agnese, R. and *et al.* Search for low-mass dark matter with CDMSlite using a profile likelihood fit. *Physical Review D*, 99(6), Mar 2019.
- [63] E. Armengaud and *et al.* Constraints on low-mass WIMPs from the EDELWEISS-III dark matter search. *Journal of Cosmology and Astroparticle Physics*, 2016(05):019–019, may 2016.
- [64] Abdelhameed, A. H. and *et al.* First results from the CRESST-III low-mass dark matter program. *Phys. Rev. D*, 100:102002, Nov 2019.

- [65] Akerib, D. S. and *et al.* Results from a Search for Dark Matter in the Complete LUX Exposure. *Physical Review Letters*, 118(2), Jan 2017.
- [66] Cui *et al.* Dark Matter Results from 54-Ton-Day Exposure of PandaX-II Experiment. *Phys. Rev. Lett.*, 119:181302, Oct 2017.
- [67] Aprile, E. and *et al.* Dark Matter Search Results from a One Ton-Year Exposure of XENON1T. *Physical Review Letters*, 121(11), Sep 2018.
- [68] Agnes, P. and *et al.* DarkSide-50 532-day dark matter search with low-radioactivity argon. *Physical Review D*, 98(10), Nov 2018.
- [69] LUX Event. https://en.wikipedia.org/wiki/Large_Underground_Xenon_experiment. Accessed: 2020-05-11.
- [70] Laura Baudis. Wimp dark matter direct-detection searches in noble gases. *Physics of the Dark Universe*, 4:50 – 59, 2014. DARK TAUP2013.
- [71] Knoll, G.F. *Radiation Detection and Measurement*. Wiley, 2000.
- [72] Y. Zhu and S. H. Yue and Z. W. Ge and Y. W. Zhu and X. J. Yin and I. Dafinei and G. DImperio and M. Diemoz and V. Pettinacci and S. Nisi and C. Tomei and H. B. Zhao and B. Xu and J. Fang and Q and . W. Tu. Production of ultra-low radioactivity NaI(Tl) crystals for Dark Matter detectors, 2019.
- [73] Bernabei, R. and *et al.* First model independent results from DAMA/LIBRA-phase2. *Nuclear Physics and Atomic Energy*, 19(4):307–325, Dec 2018.
- [74] Undagoitia, Teresa Marrodán and Rauch, Ludwig. Dark matter direct-detection experiments. *Journal of Physics G: Nuclear and Particle Physics*, 43(1):013001, Dec 2015.
- [75] D’Imperio, Giulia and *et al.* The SABRE experiment for dark matter search. *PoS, ICHEP2018:653*, 2019.
- [76] Adhikari, G. and *et al.* . Search for a Dark Matter-Induced Annual Modulation Signal in NaI(Tl) with the COSINE-100 Experiment. *Physical Review Letters*, 123(3), Jul 2019.
- [77] First Results on Dark Matter Annual Modulation from the ANAIS-112 Experiment. *Physical Review Letters*, 123(3).
- [78] Akimov, D. and *et al.* Observation of coherent elastic neutrino-nucleus scattering. *Science*, 357(6356):1123–1126, 2017.
- [79] N. Di Marco and *et al.* NEWSdm: an emulsion-based directional Dark Matter experiment. *Journal of Physics: Conference Series*, 1056:012018, jul 2018.

- [80] Tao, Y. and *et al.* Track length measurement of $^{19}\text{F}^+$ ions with the MIMAC Dark Matter directional detector prototype. 3 2019.
- [81] Mazzitelli, G. and *et al.* CYGNO: a CYGNUs Collaboration 1 m³ Module with Optical Readout for Directional Dark Matter Search. 1 2019.
- [82] Migdal, A. . *J. Phys. (USSR)*, 4, 1941.
- [83] Ibe, Masahiro and Nakano, Wakutaka and Shoji, Yutaro and Suzuki, Kazumine. Migdal effect in dark matter direct detection experiments. *Journal of High Energy Physics*, 2018(3):194, 2018.
- [84] Paolo Gorla. Review on Direct Dark Matter searches, May 2020. Presentation for LNGS-INFN National Scientific Committee in Astroparticle Physics (CSN2).
- [85] G. Bellini *et al.* Cosmic-muon flux and annual modulation in Borexino at 3800 m water-equivalent depth. *Journal of Cosmology and Astroparticle Physics*, 2012(05):015–015, may 2012.
- [86] Mei, D.M. and Hime, A. Muon-induced background study for underground laboratories. *Phys. Rev. D*, 73:053004, Mar 2006.
- [87] Yu-Cheng Wu *et al.* Measurement of cosmic ray flux in the China JinPing underground laboratory. *Chinese Physics C*, 37(8):086001, aug 2013.
- [88] Andreas Best and *et al.* Low energy neutron background in deep underground laboratories. *Nuclear Instruments and Methods in Physics Research Section A: Accelerators, Spectrometers, Detectors and Associated Equipment*, 812:1 – 6, 2016.
- [89] C. Arpesella and *et al.* Radon measurements in the Gran Sasso Underground Laboratory. *Health Phys*, 72(4):629–632, Apr 1997.
- [90] Strauss R. *et al.* A detector module with highly efficient surface-alpha event rejection operated in CRESST-II Phase 2. *The European Physical Journal C*, 75(8):352, Jul 2015.
- [91] Pröbst F. *et al.* Model for cryogenic particle detectors with superconducting phase transition thermometers. *Journal of Low Temperature Physics*, 100(1):69–104, Jul 1995.
- [92] M. Gluyas and F. D. Hughes and B. W. James. The elastic constants of calcium tungstate, 4.2-300 K. *Journal of Physics D: Applied Physics*, 6(17):2025–2037, nov 1973.
- [93] Strauss R. *et al.* Energy-dependent light quenching in CaWO_4 crystals at mK temperatures. *The European Physical Journal C*, 74(7):2957, Jul 2014.

- [94] Karoline Julia Schöffner. *Study of Backgrounds in the CRESST Dark Matter Search*. PhD thesis, Technische Universität München, 2013.
- [95] Cochran, John F. and Mapother, D. E. Superconducting Transition in Aluminum. *Phys. Rev.*, 111:132–142, Jul 1958.
- [96] G. *et al.* Angloher. Results on light dark matter particles with a low-threshold cressst-ii detector. *The European Physical Journal C*, 76(1):25, Jan 2016.
- [97] M. Mancuso and *et al.* A Low Nuclear Recoil Energy Threshold for Dark Matter Search with CRESST-III Detectors. *Journal of Low Temperature Physics*, 193(3):441–448, Nov 2018.
- [98] E. Gatti and P. F. Manfredi. Processing the signals from solid-state detectors in elementary-particle physics. *La Rivista del Nuovo Cimento (1978-1999)*, 9(1):1–146, Jan 1986.
- [99] Angloher, G. and *et al.* Results from 730 kg days of the CRESST-II Dark Matter search. *The European Physical Journal C*, 72(4):1971, Apr 2012.
- [100] Angloher G. and *et al.* Results on low mass WIMPs using an upgraded CRESST-II detector. *The European Physical Journal C*, 74(12):3184, Dec 2014.
- [101] Angloher G. and *et al.* Results on light dark matter particles with a low-threshold CRESST-II detector. *The European Physical Journal C*, 76(1):25, Jan 2016.
- [102] CERN. ROOT - Data Analysis Framework, 2020.
- [103] Florian Reindl. *Exploring Light Dark Matter With The CRESST-II Low-Threshold Detectors*. PhD thesis, Technische Universität München, 2016.
- [104] Andrea Münster. *High-Purity CaWO₄ Single Crystals for Direct Dark Matter Search with the CRESST Experiment*. PhD thesis, Technische Universität München, 2013.
- [105] Jens Michael Schmaler. *The CRESST Dark Matter Search-New Analysis Methods and Recent Results*. PhD thesis, Technische Universität München, 2010.
- [106] Daniel Schmiedmayer. Calculation of Dark-Matter Exclusion-Limits using a Maximum Likelihood Approach. Master’s thesis, Technische Universität Wien, 2019.
- [107] Bezanson, Jeff and Edelman, Alan and Karpinski, Stefan and Shah, Viral B. Julia: A Fresh Approach to Numerical Computing. *SIAM Review*, 59(1):65–98, 2017.

-
- [108] Patrick Huff. *The Detector Parameters Determining the Sensitivity of the CRESST- II Experiment*. PhD thesis, Technische Universität München, 2010.
- [109] Yellin, S. Finding an upper limit in the presence of an unknown background. *Physical Review D*, 66(3), Aug 2002.
- [110] S. Yellin. Extending the optimum interval method, 2007.
- [111] R. A. Fisher. On an absolute criterion for fitting frequency curves. *Messenger of Mathematic*, 41:155, 1912.
- [112] Roger Barlow. Extended maximum likelihood. *Nuclear Instruments and Methods in Physics Research Section A: Accelerators, Spectrometers, Detectors and Associated Equipment*, 297(3):496 – 506, 1990.
- [113] Aprile, E. *et al.* Likelihood approach to the first dark matter results from XENON100. *Physical Review D*, 84(5), Sep 2011.
- [114] Wilks, S. S. The Large-Sample Distribution of the Likelihood Ratio for Testing Composite Hypotheses. *Ann. Math. Statist.*, 9(1):60–62, 03 1938.
- [115] J. Nelder and R. Mead. A Simplex Method for Function Minimization. *Comput. J.*, 7:308–313, 1965.
- [116] Agnes, P. and *et al.* Low-Mass Dark Matter Search with the DarkSide-50 Experiment. *Physical Review Letters*, 121(8), Aug 2018.
- [117] Agnes, P. and *et al.* Results from the first use of low radioactivity argon in a dark matter search. *Phys. Rev. D*, 93:081101, Apr 2016.
- [118] Aprile, E. *et al.* Light Dark Matter Search with Ionization Signals in XENON1T. *Physical Review Letters*, 123(25), Dec 2019.